Traveling-wave Stark deceleration of SrF molecules

van den Berg, Joost Elbert

Traveling-wave Stark deceleration of SrF molecules

rijksuniversiteit groningen

faculteit wiskunde en natuurwetenschappen

van swinderen institute for particle physics and gravity

Nederlandse Organisatie voor Wetenschappelijk Onderzoek

Dit werk maakt deel uit van het onderzoekprogramma van de Stichting voor Fundamenteel Onderzoek der Materie (FOM), die deel uitmaakt van de Nederlandse Organisatie voor Wetenschappelijk Onderzoek (NWO).

ISBN: 978-90-367-7901-2 (gedrukte versie)
ISBN: 978-90-367-7900-5 (elektronische versie)
Druk: Ipskamp Drukkers, Enschede, 2015
Omslag: De binnenkant van onze afremmer. Foto van Steven Hoekstra.

rijksuniversiteit
groningen

Traveling-wave Stark deceleration of SrF molecules

Proefschrift

ter verkrijging van de graad van doctor aan de
Rijksuniversiteit Groningen
op gezag van de
rector magnificus prof. dr. E. Sterken
en volgens besluit van het College voor Promoties

De openbare verdediging zal plaatsvinden op

vrijdag 4 september 2015 om 12.45 uur

door

Joost Elbert van den Berg

geboren op 14 maart 1986
te Groningen

Promotores
Prof. dr. S. Hoekstra
Prof. dr. K. H. K. J. Jungmann

Beoordelingscommissie
Prof. dr. ir. R. A. Hoekstra
Prof. dr. G. J. M. Meijer
Prof. dr. J. Küpper

Contents

1 | Introduction

Precision spectroscopy of molecules has been a powerful tool to test physics theory for many decades. The remarkable recent advances in the techniques to control simple molecules are pushing the frontier even further [1–5]. Molecular spectroscopy can now be used to test the fundamental discrete symmetries that are at the basis of the Standard Model of particle physics. The sensitivity that can be reached in such experiments is intimately linked to the intrinsic molecular sensitivity, the experimental control over the molecules, the interrogation time, and the number of molecules. All these topics will be treated in this chapter, but some introductory words are in order here. To start with the intrinsic sensitivity: because molecules have many rotational ladders with close-lying states, mixing effects are strongly enhanced between these states, resulting in high sensitivity to, for example, parity violation effects or time variation of fundamental constants. Furthermore, in polar molecules the internal electric fields can be orders of magnitude higher than can be made in laboratories. Prime examples that exploit these electric fields are the experiments on YbF by the group of Hinds at Imperial College London [6, 7], and on ThO by the ACME collaboration between Harvard and Yale Universities [8, 9] that have put the most stringent limit on the size of an electric dipole moment of the electron (eEDM).

In order not to be limited by systematic errors, such high-precision measurements must have an excellent experimental control over the molecules. This includes very well known electric and magnetic fields as well as full control over the molecular beam's velocity and quantum state population. Only if these conditions are all met, one can obtain long coherent interaction times, a necessity to reach the ultimate precision. Very cold molecules can help substantially to fulfill those requirements: cold samples have only a few quantum states populated and this population can also be manipulated using external fields. Cold molecules can be held for relatively long times in a very small interaction zone

where it is easier to exercise full control over the measurement sequence and the applied fields. Or, they can be put in a fountain where, due to the low transverse velocity spread, they can actually traverse a long interaction zone resulting in very long coherent measurement times as well. By using traps instead of molecular beams, the interaction time can potentially be increased by a factor of a few hundred [10]. Current state-of-the art molecular beam experiments could thus be improved by going to slower and colder beams of molecules with high intrinsic sensitivity, while making sure that the number of molecules is not lowered too much. In this thesis we therefore investigate and demonstrate the deceleration and steps towards trapping of molecules that have a large inherent sensitivity for tests of fundamental discrete symmetries. Specifically, we decelerate and trap SrF molecules, as a highly sensitive probe of nuclear-spin-dependent parity violation, by adapting the recently developed traveling-wave Stark decelerator technique [11, 12].

Heavy diatomic radicals offer a high sensitivity to study the violation of the discrete parity symmetry [13–17]. Of the suitable diatomic molecules, such as YbF, SrF, PbF and RaF, only SrF has very recently been trapped by the group of DeMille [18]. Ultracold, trapped samples of those molecules would open the pathway for well-controlled experiments with long coherence times, resulting in low statistical uncertainties needed for discriminative experiments on fundamental physics laws. Whereas for atoms direct laser cooling from an evaporative oven source has provided the physics community with a plethora of ultracold species, for molecules this has not (yet) been the case. Different techniques are therefore employed for the preparation of cold and slow molecules. One of these, which is the topic of our research, is Stark deceleration. This technique makes use of electric field gradients to decelerate molecules that have a permanent electric dipole moment. Although this method does not lead to cooling of the molecules but merely to slowing them down, it is often used in combination with a cooling method such as supersonic expansion. A second possible approach, that has resulted in the coldest samples of trapped molecules so far, is the association of ultracold atoms into ultracold molecules. This approach is unfortunately not feasible for the fluorine containing alkaline-earth radicals which are of interest for fundamental physics tests. A third approach is to use buffer gas sources to produce cold, slow and bright beams of heavy diatomics, which have recently been developed with the aim of precision measurements [19, 20]. Similar to atom experiments, molecules originating from such a beam can be slowed and trapped using laser light [21], or alternatively with the Stark deceleration technique. For

a more complete overview of possible techniques to cool molecules we refer to a number of review articles [3–5, 22–25].

In the remainder of this chapter we will discuss in more detail the topics of fundamental physics experiments with molecules and the methods of slowing and/or cooling molecular beams: supersonic expansion, cryogenic buffer gas sources, deceleration using electric or magnetic fields, and laser cooling, which are all relevant for the work described in this dissertation.

1.1 Cold molecules for fundamental physics tests

Since the Standard Model is based on symmetry principles, an excellent way of testing its validity is to measure whether the symmetries really hold or are (slightly) broken. The discrete symmetries in the Standard Model are parity ($\mathcal{P}$), charge conjugation ($\mathcal{C}$), time reversal ($\mathcal{T}$) and their combinations. Not all of them are actually conserved symmetries; for instance the weak interaction is known to break the parity symmetry as was suggested in 1956 by Lee and Yang [26] and observed in 1957 by Wu and co-workers [27] in nuclear beta decay. Also the combined $\mathcal{CP}$-symmetry was found to be violated in neutral kaon decay through the strong interaction [28]. A combination of all three discrete symmetries, must always leave the physics invariant [29] due to the CPT-theorem which is the foundation of all Lorentz-invariant local field theories, such as the Standard Model. It is therefore interesting to measure to what extent $\mathcal{T}$-symmetry is broken, or to experimentally verify $\mathcal{CPT}$ invariance. Experimental validation of (breaking of) these symmetries is highly relevant for putting constraints on theories that go beyond the Standard Model. Since we know that the Standard Model is incomplete —not only because it does not include gravity— many extensions and new theories have been suggested, some of which explicitly break one of the core symmetries of the Standard Model. Some of these extensions predict the existence of new particles, which could be interpreted as being the dark matter that is thought to constitute some 24 % of the energy content in the universe [30]. Other extensions predict significant $\mathcal{CP}$ violation, which is related to the problem of the observed baryon asymmetry in the universe, i.e., the question why there is not much anti-matter in our universe. Because molecules are sensitive to both dark matter and $\mathcal{CP}$ violation, they can be used in laboratory experiments as probes for physics beyond the Standard Model on high-energy or cosmological scale.

1.1.1 Electron electric dipole moment

Time-reversal and parity symmetries forbid the existence of permanent electric dipole moments (EDM) in a fundamental particle, such as an electron. The Standard Model predicts that $\mathcal{T}$ is violated at a very small amount, such that fundamental particles can have an EDM. However, the size of such an EDM is orders of magnitude smaller than can currently (and in the near future) be measured. Nevertheless, models such as supersymmetry predict the existence of EDMs with a size that is (almost) within experimental reach [31]. Experiments are thus needed to set further constraints on the possible size of an EDM. Such an experiment usually looks for the interaction of the EDM $\boldsymbol{d}_e$ with an electric field $\boldsymbol{E}$ of the form $\boldsymbol{d}_e \cdot \boldsymbol{E}$. Because the EDM is so tiny, the interaction is very small too, and the possibility to detect the EDM at all is heavily dependent on the magnitude of the electric field. The electric field strength that can be realized in experiments is limited for technical reasons. Inside a polarizable atom or molecule, however, the effective electric field strength for valence electrons that move at high and relativistic velocities can be orders of magnitude higher. In molecules with close-lying rotational levels this can be up to a million times higher than an externally applied field. For atoms, where electronic states are further separated, the enhancement is much lower. It is therefore not suprising that, after the recent developments in molecular beam technology, the current best limit on the size of an electron-EDM comes from an experiment on a beam of ThO molecules by the ACME collaboration between the Universities of Harvard and Yale [9]. This measurement improves the results from measurements on beams of YbF molecules at Imperial College London [7] and Tl atoms as performed at the University of California, Berkely [32], by one order of magnitude. The result of $|d_\mathrm{e}| < 8.7 \times 10^{-29}\,\mathrm{e\,cm}$ at 90 % confidence level from the ThO experiment can be used to set a limit on $\mathcal{CP}$ violation up to energy scales of 3 TeV. This is a remarkable result from a molecular physics experiment, putting strong constraints on proposed high-energy theories such as various supersymmetry (SUSY) models [33], as shown in Figure 1.1. Improvement of the YbF beam electron-EDM experiment, which is currently statistics limited, is foreseen by using colder molecules and a molecular fountain setup [33] which will increase the interaction time considerably. Such a fountain could be loaded with molecules originating from a Stark decelerated beam [34]. In a similar type of experiment, it is proposed to use cold molecules to search for dark matter in the form of axions, which should induce energy shifts in the molecule due to a small axion-induced electric dipole moment [35].

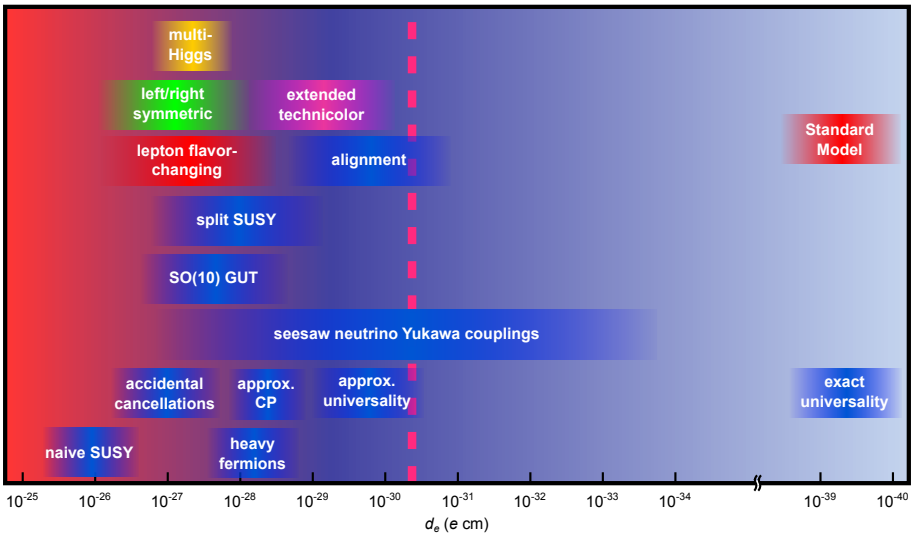

Figure 1.1: Various theories and their predicted value for the electron EDM as compiled by Dave DeMille. The region excluded by the ThO measurement [9] is highlighted in red, and the designed accuracy for the YbF fountain measurement [33] is indicated with the dashed line. The restrictions on SUSY theories are severe.

1.1.2 Parity violation

Parity violation (PV) is an important feature of the electroweak part of the Standard Model. The unification of electroweak theory by Glashow, Salam and Weinberg [36–38] in the 1960s predicted the existence of neutral current interactions which had not yet been observed at the time. These neutral currents are mediated by neutral, heavy Z^0 bosons and are therefore only effective at short ranges. The other weak interactions are mediated by charged $W^{\pm}$ bosons whose charged currents can be observed in beta decay. The observation of neutral currents at high energy and the confirmation in atomic parity violation was of great importance in establishing the validity of the Standard Model.

In 1974, Bouchiat and Bouchiat [39] described the effect of neutral currents in atomic systems in terms of mixing electronic states of opposite parity, an effect that scales faster than nuclear charge Z to the third power. Parity violation effects are therefore most pronounced in heavy atoms, and, as might be expected, in molecules with heavy nuclei. The electromagnetic interaction conserves parity symmetry whereas the weak interaction breaks this symmetry. In atoms

and molecules the weak charge of the nucleons is coupled via Z^0 exchange to the electrons. Measuring this weak charge can establish the value of the Weinberg angle $\sin^2\theta_W$, which relates the coupling strengths of the photon and the Z^0-boson and is one of the most poorly tested free parameters of the Standard Model. For atoms, the important PV interaction is via $A_e V_N$, the axial-electron and vector-nucleon currents giving rise to nuclear spin-independent parity violation which is only dependent on the nuclear weak charge and not on its spin; for diatomic molecules it is $V_e A_N$ and this gives rise to nuclear spin-dependent (NSD) parity breaking, of which only a small portion is due to the weak charge. Additionally, the nuclear anapole moment is also a source of NSD-PV. The Feynman diagrams of both NSD-PV interactions are drawn together with a visualization of the anapole moment in Figure 1.2. The anapole moment is a parity-odd magnetic

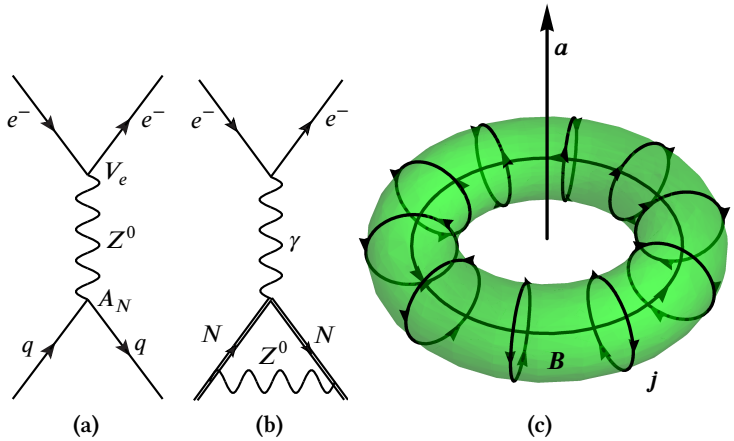

Figure 1.2: Nuclear spin-dependent parity violation via the electrons with (a) the nuclear weak charge through Z^0 exchange, (b) the anapole moment. (c) A visualization of the anapole moment. A toroidal current creates a magnetic flux and an anapole moment perpendicular to the plane of the torus.

moment resulting from a toroidal current, induced by the weak interactions inside the nucleus. The nuclear anapole moment couples electromagnetically to the electrons [40, 41]. It is a purely hadronic effect, and the potential has the form of a contact interaction: therefore the effect is greatest in heavy nuclei. Until now, only in ^{133}Cs a nuclear anapole has been measured [42]. More measurements in other species would contribute to a better understanding of hadronic PV [43]. Just as in the case of EDMs, molecules can offer tremendous advantages over

atoms in the search for parity violation, because of their internal structure.

For an overview of the enhancement of parity violation in diatomic molecules we refer to the paper by Kozlov and Labzowsky [15]. Here we will briefly discuss the most important points. The NSD-PV interaction can be described by the Hamiltonian

$$\hat{H}_{\text{NSD-PV}} = \kappa_{\text{NSD}} \frac{G_{\text{F}}}{\sqrt{2}} \frac{\boldsymbol{\alpha} \cdot \boldsymbol{I}}{I} \rho(\boldsymbol{r}), \tag{1.1}$$

where G_{F} is the Fermi constant, $\boldsymbol{\alpha}$ is the standard vector of Dirac matrices, $\boldsymbol{I}$ is the nuclear spin, $\boldsymbol{r}$ is the valence electron displacement from the nucleus with density $\rho(\boldsymbol{r})$, and κ_{NSD} is a parameter describing the strength of the interaction and is composed of $\kappa_{\text{NSD}} = \kappa_2 + \kappa_{\text{a}} + \kappa_Q$, representing the $V_e A_N$, the anapole moment, and the small weak charge contributions to NSD-PV. The anapole contribution κ_{a} can be calculated in the simple valence model as [44]

$$\kappa_{\text{a}} = 1.15 \times 10^{-3} \left(\frac{(-1)^{I+\frac{1}{2}-l} (I + 1/2)}{I + 1} \right) A^{2/3} \mu_i g_i, \tag{1.2}$$

where A is the number of nucleons, l is the orbital angular momentum of the unpaired nucleon i, which can either be a proton or a neutron, such that the magnetic moments are (expressed in nuclear magnetons) $\mu_p = 2.8$ and $\mu_n = -1.9$. The parameters g_i that describe the strength of the interaction between the valence nucleon and the core can be calculated by parameters describing low-energy PV interactions in hadrons [45], but are not well known and are usually taken to be $g_p \approx 5$, $g_n \approx -1$. A precise measurement of the anapole moment can therefore increase the knowledge of physics inside the nucleus. For $^2\Sigma_{1/2}$ and $^2\Pi_{1/2}$ molecular states the Hamiltonian can be replaced by an effective operator

$$\hat{H}^{\text{eff}}_{\text{NSD-PV}} = \kappa_{\text{NSD}} W_P \frac{(\boldsymbol{n} \times \boldsymbol{S}) \cdot \boldsymbol{I}}{I}, \tag{1.3}$$

with $\boldsymbol{S}$ the effective spin and $\boldsymbol{n}$ the unit vector from the heavier to the lighter nucleus. The factor W_P is found by calculating the matrix elements of $\boldsymbol{\alpha}\rho(\boldsymbol{r})$ and some values are listed in Table 1.1. Of main importance to us is that parity violation effects can be greatly enhanced by mixing of opposite parity levels in molecules and atoms. In molecules, such opposite parity states can be found in rotational ladders, where the spacing is small and therefore the mixing large. This mixing can be further enhanced by placing the molecule in a magnetic field, where the Zeeman shift will bring these levels to near degeneracy [14, 46]. It

Table 1.1: Theoretically calculated parity violating interaction constants W_P for various open-shell diatomic molecules. Various ab-initio and semi-empirical models have been used and the results vary accordingly. Therefore, we list here the full range of values reported in literature. In this form the list gives an idea of the order of magnitude of the parity violation effects and the uncertainties in the numerical calculations. A discussion of the theoretical frameworks, methods, the validity of the results, and values for further molecules are given in [44, 47].

Molecule	A	W_P/Hz	Reference
MgF	24	3.9–4.92	[44, 47]
CaF	40	8.0–10.6	[44, 47]
SrF	87	46–65	[16, 44, 47]
BaF	137	111–190	[15, 16, 44, 47–49]
YbF	171	484–729	[16, 44, 47, 50, 51]
RaF	225	1300–2100	[17, 44, 47]
YO	88	65.1	[44]
HfN	178	892.4	[44]
HgH	178	2000–3300	[47]
HgF	200	3162.1	[44]
PbF	207	−720 to −1269	[44, 52–54]
AcO	227	2388.9	[44]
CnH	285	31 000–48 800	[47]

was described in detail by DeMille et al. [16] how to measure NSD-PV in diatomic molecules. Their method uses a Stark-interference technique in which population transfer between the two, Zeeman-tuned to near-degeneracy, opposite parity states is measured as function of an external electric field. From this, the NSD-PV matrix element can be deduced from which then the amount of NSD-PV due to $V_e A_N$-interactions and the nuclear anapole moment must be separated. To do this properly, one could measure NSD-PV in a range of nuclei because the $V_e A_N$ part is independent of nuclear mass A while the anapole moment effect scales as $A^{2/3}$.

In such an experiment, the statistical uncertainty is inversely proportional to the number of molecules and the square root of the coherent measurement time. It is therefore beneficial to have a slow beam or trapped sample of cold molecules. In Table 1.1 we list a number of molecules with their NSD-PV sensitivities which

does not include the experimental (i.e. the Zeeman tuning to near degeneracy) effects. However, these experimental effects have been tabulated in [16] and show that for the fluorine-containing diatomics the values are all very similar. The values of W_P confirm that NSD-PV is most prominent in heavy diatomics, strengthening the case for a traveling-wave Stark decelerator. To the best of our knowledge, only the DeMille group at Yale University is currently working to measure NSD-PV, in BaF [55].

Parity was the first discrete symmetry observed to be broken, and continues to be a fruitful research topic. The most precise measurement and theoretical analysis of parity violation in an atomic system was performed in Cs atoms in 1997 [42]. The resulting value for the weak charge is still actively being researched by theoreticians [56, 57]. The result agrees within 1.5 standard deviation to the Standard Model prediction. This is of great importance in relation to theories that link parity violation to dark matter. Among these are theories that consider dark matter to consist of Majorana fermions that interact only via their anapole moment [58] or theories that predict the existence of additional Z'-bosons which would be the dark matter particles [59, 60]. Another interesting feature of NSD-PV is that a measurement of it in atoms or molecules can set limits on Lorentz symmetry violation [61] and axion dark matter [62, 63]. Electron spins couple in the same way to axions or a Lorentz symmetry violating background as they do to an anapole moment, leading to observable NSD-PV effects in atoms or molecules. Thus, apart from leading to a better understanding of nuclear physics, measuring the anapole moment can also be used in Lorentz violation or axion searches. Because the effects are tiny and need very precise measurements, the advantage of cold molecules should not be underestimated.

Chirality A related, but somewhat different topic is chirality. Chiral molecules have a handedness, meaning that they can not be overlapped with their mirror images. Especially in biochemical activity the two enantiomers can behave completely differently. For instance DNA, a chiral molecule, is the cornerstone of life as we know it on earth, and is only found in one enantiomeric form with D-type sugars and L-type amino acids. This is a clear manifestation of symmetry breaking but the causes for this homochirality are not yet known [64]. It is thought to originate from either a chance process, biological evolution, polarized light or particles, or from weak interactions [65]. If the weak interaction would energetically favor the production of one of the enantiomers instead of the other, this could, over the lifetime of the universe, result in homochirality as

the final state. Theoretical calculations on chiral molecules indicate that this is indeed a viable option [66, 67], and we like to refer to [68–70] for an overview of the measurements that are currently in progress in order to establish experimental values for the energy difference caused by the parity violation between the enantiomers. As these most recent experiments measure spectroscopically very small frequency differences between the enantiomers, they benefit from longer measurement times which could be accessible with slow beams of cold molecules.

1.1.3 Time variation of fundamental constants

The Standard Model contains a few dimensionless parameters with a value that cannot be predicted by the theory, but can only be learned from experiments. It is thought that these values, such as the fine structure constant α or the ratio of the electron to proton mass $\mu = m_e/m_p$ are constant in time and space, although this does not follow from a theoretical prediction. In fact, extensions beyond the Standard Model predict the variation of such constants. Experiments in laboratories and astronomical observations (which basically look back to the times when the universe was still young) on atomic and molecular transitions are being performed to search for such a variation. Some diatomic molecules are highly sensitive for variation of μ due to accidental degeneracies between rotational levels [71]. Again, experiments looking for μ-variation might benefit from using cold molecules; for example the group of Bethlem at the VU University Amsterdam is slowing down ammonia molecules for a molecular fountain experiment [71, 72]. We note that, for these experiments, we contributed the final traveling-wave Stark decelerator [73, 74].

1.1.4 Further applications

We briefly mention two broad fields that use cold or ultracold molecules, which could benefit from our experiments on Stark deceleration of dipolar molecules. For a review and further references we refer to the papers by Lemeshko et al. [75] and Quéméner et al. [76].

Cold collisions To study the full quantum effects of collisions, low temperatures and well prepared quantum states are necessary. Stark decelerators can be used to tune the velocity of crossed molecular beams used in collisions, such as is done in the group of Van de Meerakker at Radboud University Nijmegen [77].

For those experiments, the small velocity spread of Stark decelerated beams is of key importance to obtain high resolution scattering data. As an alternative to crossed beams, one can merge beams to do collision studies at almost zero velocity in the moving frame. Collision studies at low energies are relevant for an astrophysical understanding of interstellar matter. Ultracold molecules can also be used for controlled chemistry: the possibility of having full control over the quantum states and the environment make it possible to open up or close certain reaction paths.

Ultracold dipolar gases The long-range dipole-dipole interaction can be exploited in ensembles of polar molecules trapped in an optical lattice [78]. In such a system crystals form which could be used as quantum memory for quantum computing tasks. Furthermore, these systems can serve as quantum simulators for condensed matter physics phenomena. Indeed, this is a very broad field in which cold molecules will truly reveal their full potential.

1.2 Production of cold molecules

In the previous section we discussed the motivation for making samples of cold molecules. We note that, for tests of fundamental physics, open-shell diatomic radicals are best suited. In this section we discuss how in general samples of cold molecules can be made, but our focus will be on the diatomic radicals, and more in particular SrF, which we use in our experiments.

1.2.1 Photo-association of cold atoms

Since laser cooling is a very successful technique to make ultracold atoms, it proves to be an excellent starting point to use these ultracold atoms for making ultracold molecules. Ultracold molecules can be created from ultracold atoms by means of photo-association (PA) or Feshbach-resonance assisted PA. A full description can be found in the review [25] by Koch and Shapiro. In PA, a pair of atoms in an unbound state is transferred to a molecular bound state by the absorption of a photon. This bound state is an electronically excited state which, in general, does not provide for a fast decay path to the electronic and rovibronic ground state. However, certain diatomic bi-alkali do have such a decay path and have therefore been used in the lab for making ultracold ground state molecular samples. The range of molecules includes, but is not limited to, Cs_2, Rb_2, Na_2, K_2, Li_2, KRb, and RbCs [5]. A limiting factor for this production path is the low

reaction rate of the ultracold atoms, leading to a very low molecular production rate. This problem has been circumvented in a clever scheme using two nearly degenerate atomic gases that form a weakly bound molecular state after sweeping a magnetic field through a Fano-Feshbach resonance. The weakly bound Feshbach molecules are then coherently transferred to the ground state using a Stimulated Raman Adiabatic Passage (STIRAP) process, as was demonstrated by the group of Ye at JILA [79, 80] for KRb. The main limitation of PA is obvious: only atoms that can be laser cooled can be used as the constituents of the molecules. In practice, that limits the range to either hetero- or homonuclear bialkali. Furthermore, any heating of the molecules must be prevented during the process. Also, for reasonable production rates, the molecular energy levels need a certain amount of vibrational (Franck-Condon) overlap, which is different for each molecule. Nevertheless, PA of ultracold atoms so far seems to be the only method to create samples of almost degenerate ultracold molecules.

1.2.2 Supersonic expansion/cryogenic buffer gas cooling

Except for the case where molecules are created in a cold way, such as in photoassociation, a molecular sample needs to undergo special treatment to cool it. Normally, we start with a sample of molecules in the gas phase, which is initially at room temperature or even much hotter (for example, after laser ablation or from an oven). Especially for radicals, the molecules can be so reactive that they can only be obtained by creating them in vacuum through laser ablation off a stable precursor. In that case the fraction of molecules in the ground state is negligible. We can increase the fraction of molecules in this state by cooling the sample. Two implementations of this idea are used in the field [4]: one is cryogenic buffer gas cooling [20, 81–83] and the other one is supersonic expansion [73, 84–87]. In the former, the gas phase molecules are placed in an environment of cryogenic He gas. Through collisions the sample of molecules thermalizes with the buffer gas, thereby reducing the temperature. A small opening is made in the wall of the chamber such that the gas can escape in an effusive flow with a velocity that is typically below 150 m/s and has a temperature of only a few Kelvin. When laser ablation takes place inside the buffer gas, the source can produce a pulsed, intense beam of cold and slow molecules. This slow beam, or the slow bunch of molecules, can serve as a seed for further deceleration by means of optical forces (laser cooling) or other electromagnetic forces (Stark or Zeeman deceleration). Even though the ablation pulse is very short, the pulse of cold molecules has a length of several tens of centimeters because the diffusion

time is of order milliseconds. In addition, the velocity spread is rather large compared to a supersonic expansion. This is disadvantageous for coupling it into a Stark or Zeeman decelerator, which are typically built for molecular bunches of maximally one centimeter in size and a velocity spread of only a few m/s.

On the other hand, in the supersonic expansion method a carrier gas is let into the vacuum chamber from a high pressure reservoir through a pulse valve with a very small nozzle. By opening the valve briefly for a few hundred microseconds, a small pulse of gas can expand adiabatically into the vacuum. In this process it cools down considerably; however this comes at the expense of gaining a very high (even supersonic) forward velocity. If the molecules of interest are available in the gas phase, they can be seeded in the carrier gas. Otherwise laser ablation from a solid target, positioned at the nozzle of the valve, can create the molecules in the gas phase, which are subsequently picked up by the supersonically expanding carrier gas pulse. If the seeded molecules have a sufficient number of collisions with the expanding carrier gas, they obtain the same longitudinal velocity and internal state cooling takes place to about the same temperature as the translational beam temperature. The size of the molecular packet is mostly determined by the ablation spot size. Although the molecular packet size is much smaller than from a cryogenic buffer gas source, the beam velocity is higher.

The velocity of a supersonically expanding beam can be calculated from simple thermodynamics. Here we follow the text of Sanna and Tomassetti [88]. We start with considering the isentropic flow for a fluid unit mass, as described by the Bernoulli equation:

$$\frac{v^2}{2} + h = \text{constant}, \tag{1.4}$$

where v denotes the stream velocity and h the enthalpy per unit mass. Now, for constant pressure, the infinitesimal change in enthalpy $H = U + pV$ is given by $\mathrm{d}H = \mathrm{d}U + p\,\mathrm{d}V + V\,\mathrm{d}P = \mathrm{d}U + p\,\mathrm{d}V$. Here, U denotes the total internal energy, p the pressure and V the volume of the gas. From the first law of thermodynamics the heat transfer $\mathrm{d}Q = \mathrm{d}U + p\,\mathrm{d}V$ such that $\mathrm{d}H = \mathrm{d}Q$ for $p = \text{constant}$. The specific heat capacity at constant pressure for an ideal gas is given by $C_P = \left(\frac{\mathrm{d}Q}{\mathrm{d}T}\right)_p$, or equivalently here $C_P = \left(\frac{\mathrm{d}H}{\mathrm{d}T}\right)_p$. Thus, we can write the infinitesimal variant of Equation (1.4) as

$$\mathrm{d}\left(\frac{v^2}{2}\right) + \mathrm{d}h = \mathrm{d}\left(\frac{v^2}{2}\right) + c_p\,\mathrm{d}T = 0. \tag{1.5}$$

The specific heat at constant pressure can be related to the specific heat at constant volume via $c_p = c_V + R/M$, where R is the molar gas constant and M is the molar mass. Alternatively, c_p can be expressed through the relation $\gamma = c_p/c_V$, such that $c_p = \gamma R/M(\gamma - 1)$. For mono-atomic gases, $\gamma = 5/3$. Substituting this into Equation (1.5) and integrating, we obtain

$$\frac{v^2}{2} - \frac{v_0^2}{2} + \frac{R}{M}\frac{\gamma}{\gamma - 1}\left(T - T_0\right) = 0. \tag{1.6}$$

We can set the initial velocity v_0 in the reservoir to zero. Then,

$$v = \sqrt{2\frac{R}{M}\frac{\gamma}{\gamma - 1}\left(T_0 - T\right)}. \tag{1.7}$$

For an ideal gas, the temperature T is related to the temperature T_0 in the reservoir, the ratio of the stagnation pressure in the reservoir and the pressure in the vacuum chamber via $T = T_0(p/p_0)^{(\gamma-1)/\gamma}$. It is therefore safe to assume that $T \ll T_0$, such that the approximate beam velocity after the supersonic expansion is

$$v = \sqrt{2\frac{R}{M}\frac{\gamma}{\gamma - 1}T_0}. \tag{1.8}$$

It can be seen from the last equation that the beam velocity can be lowered by using a heavy carrier gas and by cooling the reservoir. We will calculate in Chapter 3 the effect of lowering the initial velocity on the needed length or deceleration strength of a traveling-wave Stark decelerator. The decelerator length or deceleration strength needed to fully stop the molecules depends quadratically on the initial velocity and the phase space acceptance of such a decelerator decreases much faster than that. Starting with low velocities is therefore very important in order to obtain good numbers of decelerated molecules. The calculations in Chapter 3 show that a SrF beam of 300 m/s can be decelerated to standstill with approximately 10 % transmission in a 5 m long decelerator. By using xenon and cooling the valve to −80 °C, a velocity of 280 m/s is well possible [86]. This compares unfavorably to the velocities that can be obtained with a cryogenic buffer gas source, which can be a factor two lower while being more intense [81]. However, as stated, the size and the velocity spread of the molecular packet is much smaller from a supersonic expansion, which makes it the preferred method when loading the beam into a Stark or Zeeman decelerator. Alternatively, a drastic reduction in the supersonic expansion velocity can be

obtained by moving the nozzle backwards. This has been implemented in rotating nozzles where the backward velocity due to the rotation of the valve mostly cancels the forward velocity of the beam [89]. In this way, beams of xenon with a velocity well below 100 m/s have been obtained [90]. However, as for the cryogenic buffer gas beam, in general the divergence of such a beam does not match the limited transverse acceptance of a Stark decelerator [91].

1.2.3 Stark and Zeeman deceleration

Polar molecules have an intrinsic electric dipole moment $\boldsymbol{\mu}_\mathrm{e}$ that interacts with externally applied electric fields. The same holds for paramagnetic molecules with a magnetic dipole moment $\boldsymbol{\mu}_\mathrm{B}$ that interacts with magnetic fields. These effects can be described by adding a term $\hat{H}_\mathrm{S} = -\boldsymbol{\mu}_\mathrm{e} \cdot \boldsymbol{E}$ or $\hat{H}_\mathrm{Z} = -\boldsymbol{\mu}_\mathrm{B} \cdot \boldsymbol{B}$ to the molecular Hamiltonian, causing a shift in the energy levels of the molecule. This shift, called the Stark or Zeeman energy W, is a function of the field strength E or B. A molecule with a dipole moment will therefore experience a force $\boldsymbol{F} = -\boldsymbol{\nabla} W$ when it is positioned in an inhomogeneous field. It is this force that we use to decelerate and trap molecules. For a typical polar molecule with an electric dipole moment of a few Debye in a typically experimentally achievable electric field of 100 kV/cm, the Stark energy is on the order of 0.1 cm^{-1} to 10 cm^{-1}. The same range exists for the Zeeman energy of typical molecules in a 2 T field. Only for Rydberg states, which have a large electric dipole moment due to the extent of their wave functions, Stark energies of a few cm^{-1} are observed for field strengths of order 100 V/cm. In contrast, a molecule with mass number M in a beam of 300 m/s has a kinetic energy of $E_\mathrm{k} = 3.8 M\,\mathrm{cm}^{-1}$. The experimentally realizable Stark shift, which is basically the energy that we can use to manipulate the molecule, is thus only a fraction of the kinetic energy. Additionally, the simple approximation that the electric dipole moment is a constant, resulting in an ever increasing magnitude of the Stark shift as the electric field strength rises, is only valid for small electric field strengths. In fact, the Stark effect can reduce the effective dipole moment or change its sign by mixing molecular energy levels. This shrinks the lever arm for manipulation of the molecules even further. Notwithstanding this large energy gap between the Stark shift and the initial kinetic energy, molecular beams can indeed be decelerated using a device called Stark decelerator. The first demonstration of this method in 1999 by the group of Meijer, then still in Nijmegen [92], used an electric field switching procedure in a *multistage* Stark decelerator. Since then, the same group has also employed a *traveling-wave* approach [93] that we will pursue as well. Schematic drawings of

multistage Stark and Zeeman decelerators, and Rydberg-Stark decelerators are shown in Figure 1.4, for a traveling-wave decelerator see Figure 1.5a. For further details on Zeeman deceleration we refer to the review by Narevicius and Raizen [24].

Multistage Stark decelerators are based [1] on letting molecules fly through an array of fast switching high-voltage electrodes as depicted in Figure 1.3. A molecule with its electric dipole moment oriented opposite to the electric field will gain potential energy when it enters the field in between two electrodes. In this process, the gain of potential energy comes at a loss of kinetic energy: the molecule decelerates. When the voltages are switched off just at the moment when the molecule is in between the electrodes, the potential energy becomes zero and the net result is only a loss in kinetic energy. This process is then repeated many times for an array of such electrodes. To keep the molecules focused on axis subsequent electrodes are placed orthogonally. However, this merely creates a non-continuous effective potential that is far from perfect and leads —especially at lower velocities— to loss of molecules, even when optimized switching schemes are applied [94].

In contrast, traveling-wave Stark deceleration is based on genuine three-dimensional potential wells which are formed by closed electric field lines as depicted in Figure 1.5b. Molecules with an electric dipole moment oriented such that their energy is lowest in the minimum of the electric field can be trapped inside these field lines. Once trapped in such a moving potential well, the potential wells can be slowed down, thereby exerting a force on the trapped molecules so that they decelerate as well. This principle, equivalent to a conveyor belt, is truly stable and does not lead to molecule losses. For efficient deceleration it is important that the acceptance of the decelerator is as large as possible. The depth of the trap determines the maximum relative velocity that the molecules can have with respect to the moving traps, and this depends on the electric field strength and the specific shape of the Stark shift of the molecular state. The maximal deceleration strength is determined by the gradient of the potential well, which depends on the electric field gradient and the shape of the Stark shift as well.

Stark deceleration [92] and subsequent trapping has been demonstrated for a number of molecules in recent years [95–101]. These molecules are relatively light (<25 atomic mass units (u)) and have almost linear Stark shifts. Stark deceleration of heavier molecules (which can be roughly defined as having a mass >100 u) is more difficult for two reasons. First, the heavy mass makes the stopping distance longer. Second, due to the small rotational constants of heavy

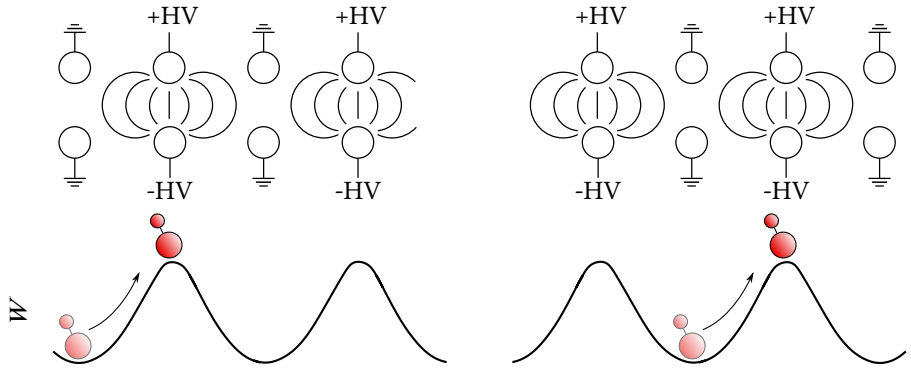

Figure 1.3: A polar molecule which has its electric dipole moment oriented anti-parallel to the electric field lines will gain potential energy W while flying into an electric field as shown on the left. This gain is compensated by a loss in kinetic energy; the molecule is decelerated. If an electric field remains on, the molecule will accelerate while leaving the electric field and regains kinetic energy. However, if the electric field is abruptly switched off, as shown on the right, the potential energy of the molecule is reduced while the molecule keeps its lower kinetic energy. Repeating this procedure forms the principle of a multistage Stark decelerator and slows down the molecule. Figure adapted from [94]. A Zeeman decelerator works similarly, but has current coils instead of electrodes, through which current pulses are sent.

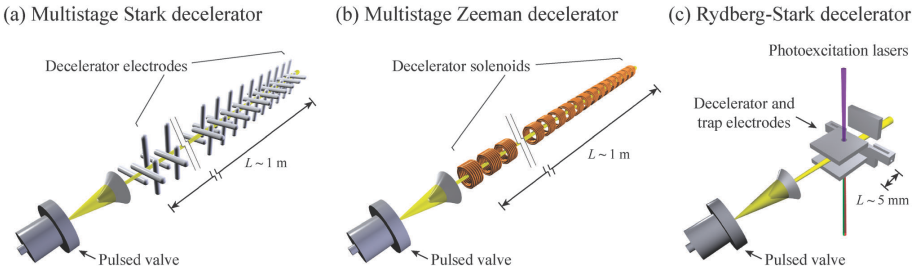

Figure 1.4: Schematic diagrams of (a) a multistage Stark decelerator, (b) a multistage Zeeman decelerator, and (c) a single-stage Rydberg-Stark decelerator and trap. Reproduced from [84] with permission of the PCCP Owner Societies.

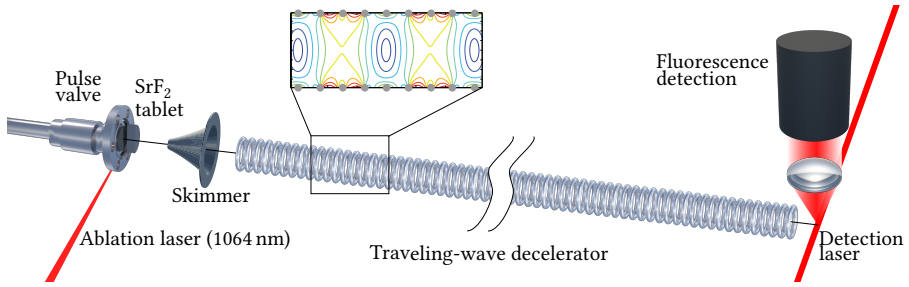

(a) A schematic diagram of a traveling-wave Stark decelerator.

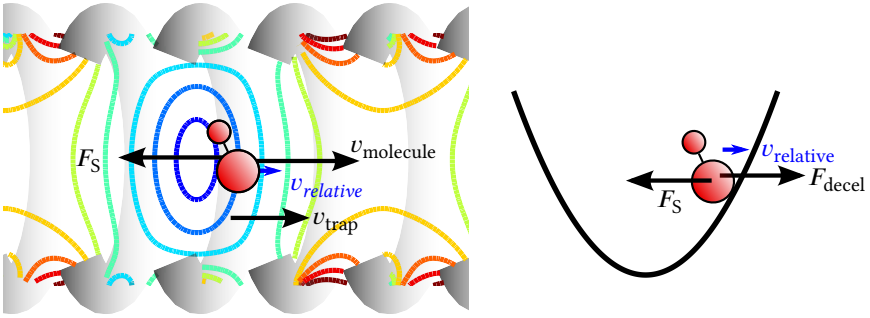

(b) Left: In a traveling-wave decelerator molecules can be 3D confined in the minimum of an electric field, created by ring-shaped electrodes. The traps themselves can be moved with a velocity $\boldsymbol{v}_{\text{trap}}$ by varying the voltages on the rings. The molecules move with a velocity $\boldsymbol{v}_{\text{relative}} = \boldsymbol{v}_{\text{molecule}} - \boldsymbol{v}_{\text{trap}}$ relative to the trap. When v_{relative} is close to zero, the molecule has a constant position in the trap and feels a constant Stark force $\boldsymbol{F}_S$ due to the electric field gradient. This force slows down the molecule. Right: In the non-inertial frame of the decelerating trap it can be seen that the molecule remains trapped if 1.) the kinetic energy $1/2mv^2_{\text{relative}}$ is smaller than the depth of the potential and 2.) the deceleration force is balanced by the Stark force.

Figure 1.5: The principle of a traveling-wave decelerator.

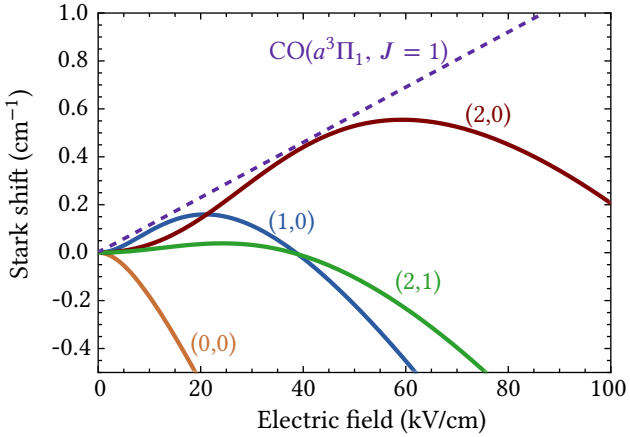

Figure 1.6: The Stark shifts of the rovibronic ground state and the lowest low-field seeking rotational levels of the SrF molecule in its $X\ ^2\Sigma^+$ electronic ground state, and the metastable $a^3\Pi_1$, $J = 1$ level of the light molecule CO for comparison. The levels are labeled (N, M_N) where N is the rotational quantum number in zero field and M_N the projection of N on the electric field axis.

molecules, the Stark shift is rather small and has a turning point at modest electric field strengths. This is shown in Figure 1.6 where the Stark shifts for the lowest rotational states in SrF are compared to the linear Stark shift for CO in the metastable $a^3\Pi_1$, $J = 1$ level. This reduces the achievable deceleration strength, as we will discuss in Section 2.1. The small Stark shift combined with the large mass requires a rather long decelerator, which puts high demands on the stability of the deceleration process. In a multistage Stark decelerator, the stability is problematic because of the coupling between longitudinal and transverse motion. This induces a loss which gets worse as the decelerator is longer. Decelerating high-field seeking states in a so-called Alternating Gradient decelerator has been demonstrated for various molecules [102–104]. However, because of high losses at low velocities, fully decelerating to complete standstill is unfeasible using this technique [10]. Hence only traveling-wave deceleration, which is inherently stable, is a feasible modality for Stark decelerating these heavy molecules originating from a supersonic expansion. As an additional advantage, a traveling-wave decelerator can also be used as a static trap for a fully stopped beam of molecules. Such a trapped cloud can be further cooled down by adiabatic cooling [72] or in situ laser cooling. The ring electrode trap can also be overlapped with an optical dipole trap to enable efficient loading of the

latter. But above all, the prime advantage is that trapped molecules can be interrogated for longer times, reducing statistical errors and enabling high-precision measurements.

Centrifuge deceleration A new method for decelerating continuous beams of polar molecules was developed in the group of Rempe. In their experiment [105], they decelerated a continuous beam of CF_3CCH ($m = 94\,\mathrm{u}$, $d = 2.4\,\mathrm{Debye}$) with a velocity of 200 m/s to 15 m/s using a rotating spiral electric quadrupole guide, which provided a centrifugal force that was used to slow down the molecules. To the best of our knowledge, no study of the efficiency of a centrifuge decelerator in combination with a cryogenic buffer gas source of heavy diatomic radicals has been made. Such a study would be of interest in a comparison to a traveling-wave Stark decelerator.

1.2.4 Laser slowing and cooling

Laser slowing and cooling works very well for alkali atoms, noble gases and earth-alkali cations. For many species, such as earth-alkali atoms or atoms with nuclear spin, the level schemes are such that multiple transitions need to be covered by the lasers in order to make the cooling or slowing efficient. In molecules, this is often even worse: the huge amount of vibrational and rotational levels make it in general nearly impossible to create a closed cooling cycle. However, Di Rosa pointed out that for a large class of diatomic molecules, the vibrational branching to higher levels is so low that this effect can be handled by only one or two repump lasers, and that dipole selection rules enable access to a fully closed rotational cycle [106]. Laser cooling and slowing of SrF molecules followed by subsequent trapping in a three dimensional magneto-optical trap was first shown by the group of DeMille [18, 21, 107]. Although the number of trapped molecules is still rather low, this is a very important step forward in the field of producing samples of cold molecules. Also, other molecules such as CaF [108] and YO [109] have now been laser cooled, and work on YbF is underway [110]. A more elaborate overview of molecular laser cooling and its application to SrF molecules can be found in the dissertation of Meinema [111].

1.2.5 Discussion of production methods

We compare photo-association, deceleration and direct laser cooling in terms of feasibility for producing cold molecules of different kinds. For diatomics con-

sisting of two laser coolable alkali atoms, cold association seems best suited for producing ultracold, dense, samples. For earth-alkaline monohalides, direct laser slowing of molecules from a cryogenic buffer gas source beam is possible, however, the yields are low. This is mostly due to transverse spreading of the slow molecular beam. Additional confinement in the transverse direction, in the form of transverse laser cooling or electromagnetic guiding fields could mitigate the transverse losses [112]. Furthermore, the complicated hyperfine structure (e.g. in molecules of interest for nuclear spin-dependent parity violation) and the vibrational branching do require the use of at least a handful of lasers to keep the cooling cycle closed enough for slowing. A very promising approach appears to be the combination of Stark or Zeeman deceleration of an intense supersonic beam and laser cooling afterward. In such a setup, the molecules start out cold from the supersonic expansion and the slowing is done by the decelerator. The available optical cycles can then be used fully for further cooling, instead of spending them on the slowing part. The additional advantage of a traveling-wave decelerator over a multistage decelerator is that the transverse confinement of the beam is guaranteed throughout the deceleration process. While the length of such a decelerator is only on the order of a few meters, its versatility makes it suitable for almost any molecule with an electric dipole moment and low-field seeking states, and that can be created in a supersonic expansion or a cryogenic buffer gas source. The fact that the molecules remain trapped inside the decelerator makes it possible to do further experiments or apply additional cooling methods afterward.

For these reasons, and because of our interest in testing fundamental laws of physics, we have opted to build a traveling-wave Stark decelerator for the deceleration of SrF radicals, originating from a supersonic expansion. We have chosen SrF because it has a reasonable electric dipole moment and Stark shift for deceleration, it is heavy enough to have a significant sensitivity to NSD-PV while it is not too heavy for deceleration in a few meters length, and it is laser coolable which makes a very sensitive measurement on trapped ultracold molecules possible. We have chosen a supersonic expansion source, because at the start of the project good results with such a source had been reported for YbF [86]. The size of the molecular packet originating from such a source is more suited for the size of a traveling-wave decelerator than the long pulses from a cryogenic buffer gas source. We calculate in Chapter 3 below that the number of decelerated, trapped molecules is expected to be higher than reported via direct laser cooling from a cryogenic buffer gas source. We conclude with

noting that the chosen molecule combined with the techniques does not limit the experiments to merely testing fundamental physics: applications in the field of dipole-dipole interactions in optical lattices or quantum information processes are within reach of the experimental setup.

To sum up, the subject of cold molecules forms an interesting research topic. In this thesis, we discuss the design, the construction and the first operation of a large traveling-wave Stark decelerator for creating slow bunches of SrF molecules, in preparation of a fundamental physics measurement.

2 | SrF interacting with electric fields

In this chapter we discuss the interaction of our chosen molecule SrF with electric fields, in the form of static fields or laser beams. Those aspects are relevant for the Stark deceleration and subsequent laser induced fluorescence detection of the molecules. Most of the text is based on the books by Herzberg [113] and Brown and Carrington [114].

2.1 Stark shift for $^2\Sigma$ diatomics

To determine the size of the Stark shift for diatomic molecules we start from the description of the molecule as a linear rigid rotor. For the purpose of this work we only consider radicals in an open-shell $^2\Sigma$ electronic state, where the projection of electron's orbital angular momentum onto the internuclear axis is zero. The relevant quantum numbers are defined as in Figure 2.1. Excluding spin, the Hamiltonian is given by [113]

$$\hat{H}_0 = \frac{\hat{N}^2}{2I}, \tag{2.1}$$

where $I = \mu {R_\mathrm{e}}^2$ is the moment of inertia. Here R_e is the equilibrium internuclear distance and μ denotes the reduced mass of the two nuclei. The eigenfunctions of the quantum rotational operator $\hat{N}$ are given by the spherical harmonics $Y_m^n(\theta, \phi) = \langle \theta, \phi | N M \rangle$ and the eigenvalues are $\hbar^2 N(N+1)$. The energy is independent of the azimuthal quantum number $M = -N, -N+1, \ldots, N$. When we include the interaction of the electric dipole moment $\boldsymbol{\mu}_\mathrm{e}$ with an external electric field $\mathcal{E}$ the Hamiltonian becomes

$$\hat{H} = \hat{H}_0 + \hat{H}_\mathrm{S} = \frac{\hat{N}^2}{2I} - \boldsymbol{\mu}_\mathrm{e} \cdot \mathcal{E} = \frac{\hat{N}^2}{2I} - \mu_\mathrm{e} \mathcal{E} \cos(\theta). \tag{2.2}$$

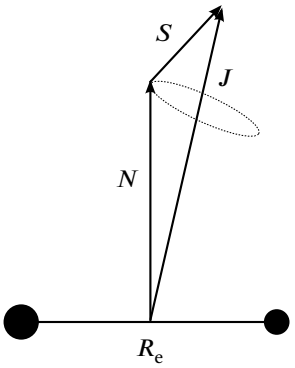

Figure 2.1: A schematic picture of a diatomic molecule in a $^2\Sigma$ Hund's case (b) configuration. The molecular rotation is indicated by $\boldsymbol{N}$ and the total angular momentum is found by adding the electron spin to the nuclear rotation: $\boldsymbol{J} = \boldsymbol{N} + \boldsymbol{S}$. The electric dipole moment $\boldsymbol{\mu}_e$ lies along the internuclear axis $\boldsymbol{R}_e$. In the text, we ignore electron spin so that $\boldsymbol{J} = \boldsymbol{N}$.

For small electric field strengths, the Stark interaction $\hat{H}_S$ can be treated as a perturbation to the original Hamiltonian $\hat{H}_0$. Second order perturbation theory [115] gives the following expression for the energy levels:

$$E_{NM} = E_N^0 + H_{NN}^S + \sum_{N'M' \neq NM} \frac{|\langle N'M'|\hat{H}_S|NM\rangle|^2}{E_N^0 - E_{N'}^0}, \tag{2.3}$$

where $E_N^0 = BN(N+1)$ is the unperturbed rotational energy with the rotational constant $B = \hbar^2/2I$, and $H_{NN}^S = \langle NM'|\hat{H}_S|NM\rangle = 0$ is the first order Stark shift which vanishes because of parity symmetry. The other matrix elements can be calculated by realizing that the $\cos(\theta)$ operator can be expressed as $\cos(\theta) = \sqrt{\frac{4\pi}{3}}Y_0^1(\theta,\phi)$. Now,

$$\langle N'M'|\hat{H}_S|NM\rangle = -\sqrt{\frac{4\pi}{3}}\mu_e\mathcal{E}\langle N'M'|Y_0^1|NM\rangle. \tag{2.4}$$

The result comes from standard angular momentum theory [116] and is given by

$$\langle N'M'|\hat{H}_S|NM\rangle = (-1)^{M'}(-\mu_e)\mathcal{E}\sqrt{(2N+1)(2N'+1)}\times \begin{pmatrix} N' & 1 & N \\ -M' & 0 & M \end{pmatrix}\begin{pmatrix} N' & 1 & N \\ 0 & 0 & 0 \end{pmatrix}. \tag{2.5}$$

The 3j-symbols vanish except when $M' = M$ and $N' = N \pm 1$, that is, the Stark interaction mixes states that differ by one rotational quantum but have the same azimuthal quantum number. For the ground state $N = 0$ we only need to consider the coupling between the $|NM\rangle = |00\rangle$ and the $|10\rangle$ states:

$$E_{00} = \frac{|\sqrt{\frac{4\pi}{3}}\mu_e\mathcal{E}\langle 10|Y_0^1|00\rangle|^2}{-2B} = \frac{\mu_e^2\mathcal{E}^2(2\cdot 0+1)(2\cdot 1+1)}{-2B}\times \left|\begin{pmatrix} 1 & 1 & 0 \\ 0 & 0 & 0 \end{pmatrix}\begin{pmatrix} 1 & 1 & 0 \\ 0 & 0 & 0 \end{pmatrix}\right|^2 = -\frac{\mu_e^2\mathcal{E}^2}{6B}. \quad (2.6)$$

For this state the Stark shift is quadratic in the electric field strength and has a negative slope. The next rotational level $N = 1$ has the three $M = -1, 0, 1$ states of which the $M = \pm 1$ are degenerate because of time reversal invariance. The sum in Equation (2.3) contains the terms $\langle 00|\hat{H}_S|10\rangle, \langle 20|\hat{H}_S|10\rangle$ for the $M = 0$ state, and $\langle 21|\hat{H}_S|11\rangle$ for the $M = \pm 1$ states. Evaluating those gives:

$$E_{10} = +\frac{\mu_e^2\mathcal{E}^2}{6B} + \frac{\langle 20|\hat{H}_{\text{Stark}}|10\rangle}{E_1^0 - E_2^0} = \frac{\mu_e^2\mathcal{E}^2}{B}\left(\frac{1}{6} - \frac{1}{15}\right) = \frac{\mu_e^2\mathcal{E}^2}{10B} \quad (2.7)$$

$$E_{11} = -\frac{\mu_e^2\mathcal{E}^2}{20B}. \quad (2.8)$$

The two states of the $N = 1$ level with nonzero M have a different Stark shift compared to the $M = 0$ state, with opposite sign. Thus the interaction with the electric field partly lifts the degeneracy of the rotational levels, and we end up with both positively and negatively shifted states. The resulting force $\boldsymbol{F} = -\boldsymbol{\nabla}W(\mathcal{E})$ is oriented opposite the direction of the electric field gradient for molecules in states with a positive Stark shift. We call those states *low-field seeking* (LFS). States with a negative Stark shift are attracted to high electric field strengths, and are therefore called *high-field seekers* (HFS).

Unfortunately this perturbative calculation of the Stark shift does not give the full story, as it only holds for small electric field strengths such that the Stark shift is much less than the unperturbed rotational energy splitting. For higher field strengths, perturbation theory is insufficient and we need to diagonalize the full Hamiltonian to solve the Schrödinger equation for the eigenvalues W_q:

$$\hat{H}|\psi_q\rangle = \left[\frac{\hat{N}^2}{2I} - \mu_e\mathcal{E}\cos(\theta)\right]|\psi\rangle = W_q|\psi_q\rangle. \quad (2.9)$$

Multiplying from the left with $\langle N, M|$ and inserting the full set of states $\sum_{N',M'} |N'M'\rangle\langle N'M'|$, we arrive at the left-hand side being

$$\sum_{N',M'} \langle N, M| \left[\frac{\hat{N}^2}{2I} - \mu_e \mathcal{E}\cos(\theta)\right] |N'M'\rangle\langle N'M'|\psi_q\rangle = \left[B N(N+1)\delta_{NN'}\delta_{MM'} - \sum_{N',M'} \langle N, M|\mu_e \mathcal{E}\cos(\theta)|N'M'\rangle\right] \langle N'M'|\psi_q\rangle. \tag{2.10}$$

We write the right-hand side $W_q\langle N'M'|\psi_q\rangle$ as a column vector ordered by N' so that for every N' there are $2N'+1$ elements labeled by M' running from $-N'$ to N'. Then the left-hand side of the Schrödinger equation (2.9) can be written in matrix form as:

$$\begin{pmatrix} 0 & 0 & \langle 00|\hat{H}_S|10\rangle & 0 & 0 & 0 & \cdots \\ 0 & 2B & 0 & 0 & 0 & \langle 1{-}1|\hat{H}_S|2{-}1\rangle & \cdots \\ \langle 10|\hat{H}_S|00\rangle & 0 & 2B & 0 & 0 & 0 & \cdots \\ 0 & 0 & 0 & 2B & 0 & 0 & \cdots \\ 0 & 0 & 0 & 0 & 6B & 0 & \cdots \\ 0 & \langle 2{-}1|\hat{H}_S|1{-}1\rangle & 0 & 0 & 0 & 6B & \cdots \\ \vdots & \vdots & \vdots & \vdots & \vdots & \vdots & \ddots \end{pmatrix} \begin{pmatrix} \langle 00|\psi\rangle \\ \langle 1{-}1|\psi\rangle \\ \langle 10|\psi\rangle \\ \langle 11|\psi\rangle \\ \langle 2{-}2|\psi\rangle \\ \langle 2{-}1|\psi\rangle \\ \vdots \end{pmatrix}, \tag{2.11}$$

where we used the previously found fact that the Stark matrix elements only couple states with $M' = M$ and $N = N' \pm 1$. The eigenvalues of this infinite matrix are to be found by diagonalizing it. Since only finite matrices can be diagonalized we need to truncate the matrix by setting a limit on the maximum N' to include.

This calculation including up to $N' = 8$ (converging to better than 0.1 ‰) was performed with Mathematica [117]. As a result the Stark shifted energy levels for a diatomic molecule in the $^2\Sigma$ electronic state is plotted in Figure 2.2 in terms of the dimensionless number W/B as a function of $\mu_e\mathcal{E}/B$. From the figure it is apparent that the quadratic shape of the Stark shift is indeed limited to the regime of low electric field strength. For higher field strengths, the curve becomes linear due to Stark mixing with high rotational levels. The ground state has a high-field seeking character. Also, the states that start out as low-field seeking, turn into high-field seekers from a certain electric field strength onwards.

By mixing rotational levels, the Stark shift induces an electric dipole moment in the molecule. The derivative of the Stark curve gives the effective electric

dipole moment $\mu_{\text{eff}} = \frac{\mathrm{d}W(\mathcal{E})}{\mathrm{d}\mathcal{E}}$. The sign of μ_{eff} determines the HFS or LFS character of the state.

Because the high molecular mass of relevant molecules gives rise to small spacings of rotational levels, already at modest electric field strengths (20 kV/cm–30 kV/cm) the slope of the Stark curve of the lowest rotational levels turns negative; at higher fields these states are all high-field seekers, and are attracted to the high field at the electrodes of a decelerator. At the turning point the maximum Stark shift is for the lowest rotational states only a fraction of a wavenumber, as can be seen in Table 2.1. This is illustrated in Figure 2.2 for the lowest rotational states of SrF in its $X\,^2\Sigma^+(v = 0)$ electronic and vibrational ground state and severely limits the maximal deceleration strength that can be applied in a traveling-wave decelerator for these molecules.

Table 2.1: Molecular parameters, maximal Stark shift, and the value of the electric field at this peak shift for diatomic molecules in the $X\,^2\Sigma^+$ rotational states (N, M) from the calculations presented here. Molecular masses are taken from [118]. For PbF we calculated the Stark curve for the $X^2\Pi_{1/2}$, $(J, M) = (3/2, 1/2)$ e-parity state using PGOPHER [119]. For CO in the $a^3\Pi_1$, $J = 1$ state, which does not have a Stark maximum, we give the Stark shift at an electric field of 100 kV/cm.

				$W_{\text{max}}/\text{cm}^{-1}$		$\mathcal{E}_{\text{peak}}/(\text{kV/cm})$	
Molecule	Mass/u	μ_e/Debye	B/cm^{-1}	(1,0)	(2,0)	(1,0)	(2,0)
CaF [120]	59	3.07	0.34	0.22	0.75	32.4	91.9
SrF [121, 122]	106	3.50	0.25	0.16	0.56	20.9	59.3
BaF [123, 124]	156	3.17	0.21	0.13	0.47	19.4	55.0
YbF [125]	192	3.91	0.24	0.15	0.53	18.0	50.9
PbF [126]	226	3.5	0.23	0.2		34	
CO [1]	28	1.37	1.68	1.15		100	

2.2 SrF spectroscopy

In this section we discuss the basics of molecular spectroscopy relevant for SrF. It forms the basis for further chapters in which we explain optical detection of SrF with laser induced fluorescence.

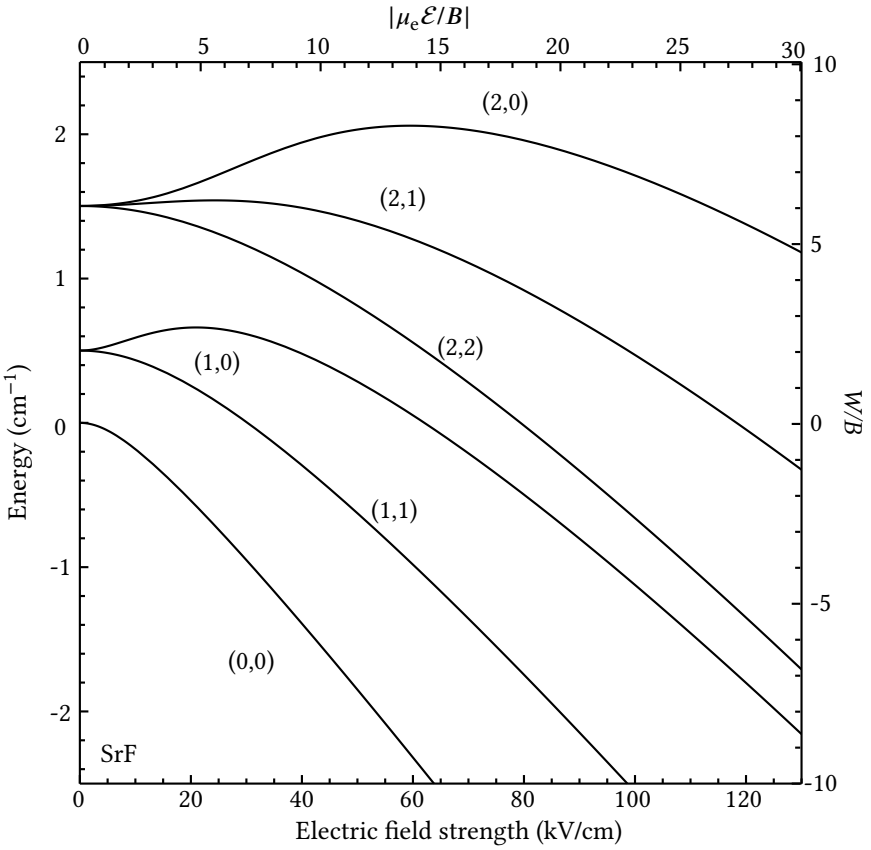

Figure 2.2: The energy levels of the three lowest rotational levels of a diatomic molecule in a $^2\Sigma$ state, shifted by the Stark effect, as function of its electric dipole moment μ_e, its rotational constant B, and the magnitude of the electric field $\mathcal{E}$ (top and right axes). For the SrF molecule in the $X\,^2\Sigma^+$ electronic ground state ($\mu_e = 3.5\,\text{Debye}$ and $B = 0.25\,\text{cm}^{-1}$) the values can be read off from the left and bottom axes. The contributions up to $N = 8$ are included in the calculation. The levels are labeled (N, M) where N is the rotational quantum number in zero field and M the projection of N on the electric field axis.

2.2.1 Vibrational and rotational levels of diatomics

The total energy of a diatomic molecule can be parametrized in the Born-Oppenheimer approximation. In this approximation we can separate the nuclear motion from the electronic motion which have, due to their masses differing by orders of magnitude, vastly different timescales involved. The total energy can thus be written as [113]

$$E = E_e + E_v + E_r, \tag{2.12}$$

or, in wavenumber units (cm^{-1})

$$T = T_e + G + F = E/hc, \tag{2.13}$$

where T_e is the pure electronic energy, G is the vibrational energy, and F is the rotational energy. For our purposes the electronic energy can be described by a static potential surface varying as a function of the internuclear distance as shown in Figure 2.3. We limit our discussion to molecules in the ground and first excited electronic states which are denoted by X and A, respectively. On such a potential surface, the vibrational energy can be parametrized around the equilibrium internuclear distance R_e by an anharmonic potential of the form [114]

$$V(R) = f\left(R - R_e\right)^2 - g\left(R - R_e\right)^3 \tag{2.14}$$

that results in energy levels

$$G(v) = \omega_e(v + 1/2) - \omega_e x_e(v + 1/2)^2 + \omega_e y_e(v + 1/2)^3 + \cdots. \tag{2.15}$$

The rotational levels, on the other hand, can be obtained by starting from the, classically inspired, Schrödinger equation for a rigid rotor

$$\frac{\hbar^2}{2\mu R^2}\hat{J}^2\psi = E\psi, \tag{2.16}$$

which we have discussed already in Section 2.1 in relation to the Stark shift.

In practical cases, there is not only one single quantum number J as for the rigid rotor. The relevant angular momenta are (see Figure 2.4): molecular rotation of the nuclei $\boldsymbol{R}$, electron orbital angular momentum $\boldsymbol{L}$, electron spin $\boldsymbol{S}$, total angular momentum excluding electron and nuclear spin $\boldsymbol{N}$, total angular momentum excluding nuclear spin $\boldsymbol{J}$, nuclear spin $\boldsymbol{I}$, and total angular momentum $\boldsymbol{F}$. The coupling of the angular momenta can in general be categorized in four cases, named after Hund. We will consider only Hund's cases (a) and (b) shown

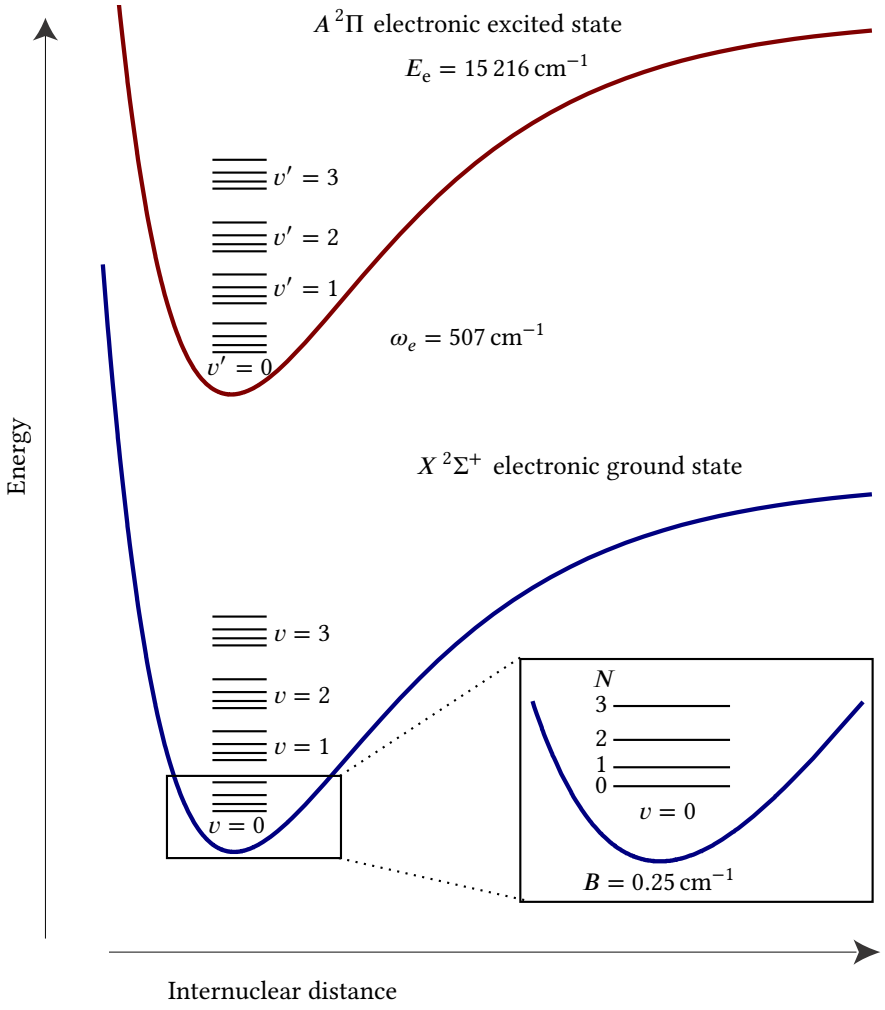

Figure 2.3: Energy level scheme (not to scale) of SrF in its ground $X\,^2\Sigma^+$ and first excited electronic $A\,^2\Pi$ state. The electronic potential wells are dependent on the internuclear distance R. Within these potential energy surfaces, the vibrational levels are indicated, with on top of those the rotational levels. Typical energy scales E_e, ω_e, and B are indicated, clearly showing that the three energy regimes are well separated.

in Figure 2.4, as those are the only relevant cases for the electronic ground X and first excited A states in SrF. The main difference between those two cases is

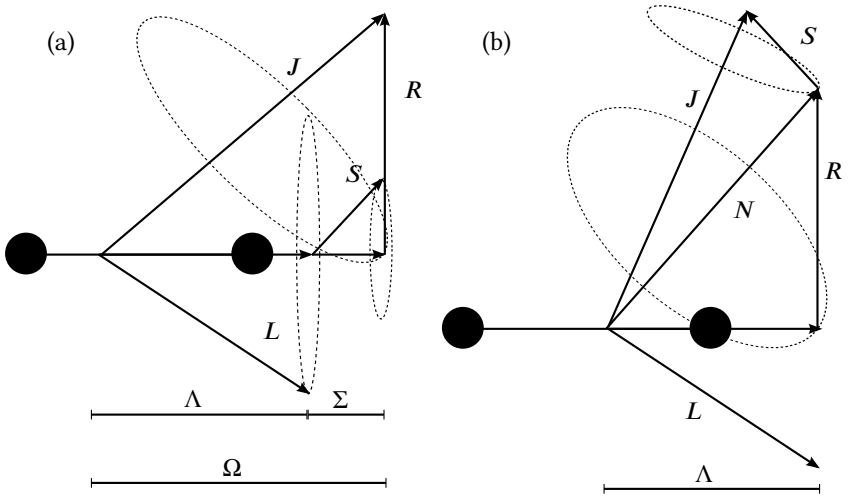

Figure 2.4: Hund's cases (a) and (b).

the strong coupling of the electron's angular momenta to the internuclear axis in case (a), as opposed to case (b) where this coupling is absent.

2.2.2 SrF $X\,^2\Sigma^+$ ground state

The ground state of SrF is the $X\,^2\Sigma^+$ state that can be described as a Hund's case (b) system. The notation $X\,^2\Sigma^+$ implies that the single valence electron with spin $S = 1/2$ has zero orbital angular momentum $\Lambda = 0$.

In Hund's case (b) the electron spin is not coupled to the internuclear axis. This is most often the result of a zero orbital angular momentum $\boldsymbol{L}$, but can also occur when the spin-orbit coupling is very weak. If nonzero, $\boldsymbol{L}$ precesses around the internuclear axis, and Λ, the projection of $\boldsymbol{L}$ on the internuclear axis, is a well-defined quantum number. Λ is coupled to the molecular rotation $\boldsymbol{R}$ to form the total angular momentum without spin $\boldsymbol{N}$. In the $\Lambda = 0$ case, $\boldsymbol{N} = \boldsymbol{R}$ and is perpendicular to the internuclear axis. The total angular momentum is formed as $\boldsymbol{J} = \boldsymbol{N} + \boldsymbol{S}$.

Rotational levels in the SrF $X\,^2\Sigma^+$ ground state The rotational levels are in principle given by N, but are split up into different $N, \boldsymbol{J}$ combinations due to the spin-rotation interaction $\hat{H}_{\mathrm{SR}} = \gamma \boldsymbol{S} \cdot \boldsymbol{N}$. Therefore we get spin doublets with

energies

$$F_1(N) = BN(N+1) + \frac{1}{2}\gamma N, \tag{2.17a}$$

$$F_2(N) = BN(N+1) - \frac{1}{2}\gamma(N+1). \tag{2.17b}$$

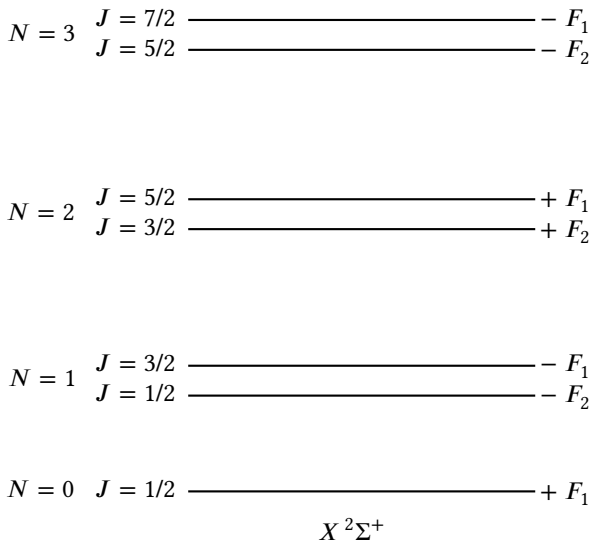

Figure 2.5: The $X\,^2\Sigma^+$ electronic ground state of SrF. For one particular vibrational level the rotational structure is displayed, including spin-rotation splitting denoted by the F_1, F_2 labels and their parities. Hyperfine splitting is not shown.

2.2.3 SrF excited $A\,^2\Pi$ state

The first electronic excited state in SrF is the $A\,^2\Pi$ state. This doublet Π state can be well described as a Hund's case (a). In Hund's case (a), the electron motion is very strongly coupled to the axis joining the nuclei. Electrostatic forces couple $\boldsymbol{L}$ to the internuclear axis and $\boldsymbol{S}$ is strongly coupled to $\boldsymbol{L}$ by the spin-orbit interaction. This causes $\boldsymbol{L}$ and $\boldsymbol{S}$ to precess around the internuclear axis. Since the symmetry of the potential in which the electrons move is reduced from a complete spherical to cylindrical symmetry around the internuclear axis, the total orbital angular momentum $\boldsymbol{L}$ is not a constant of the motion or a conserved

quantity, as it is in a spherically symmetric atom. However, Λ, the component of $\boldsymbol{L}$ along the internuclear axis, is a good quantum number instead of $\boldsymbol{L}$ itself. It is clear that $\Lambda = |M_L| = 0, 1, 2, \ldots, L$.

The component of $\boldsymbol{S}$ along the internuclear axis is denoted by Σ. Together with Λ, this produces a total vector $\Omega = |\Lambda + \Sigma|$ along the internuclear axis. This $\boldsymbol{\Omega}$ is added to the nuclear rotation $\boldsymbol{R}$ perpendicular to the internuclear axis to form the total angular momentum $\boldsymbol{J}$. $\boldsymbol{R}$ and $\boldsymbol{\Omega}$ nutate around $\boldsymbol{J}$.

Hund's case (a) levels have two types of degeneracy: Ω and Λ doubling. Ω doubling is comparable to fine structure in atoms and is the result of the fact that due to the two possible senses of rotation, Λ and Σ can have opposite sign: $\Omega = |\Lambda \pm \Sigma|$. Λ doubling is much smaller and is due to the possible two senses of Λ for each value of Ω. It relates to the parity of the states.

In spectroscopic notation we label the states ${}^{2S+1}\Lambda_\Omega$. In the SrF $A\,{}^2\Pi$ state, we have one valence electron with $\Lambda = 1$ and $S = 1/2$, resulting in $\Sigma = \pm 1/2$ and $\Omega = 1/2, 3/2$. Thus, we have two levels denoted as ${}^2\Pi_{1/2}$ and ${}^2\Pi_{3/2}$. The coupling $\Lambda\Sigma$ results in an energy splitting A between these levels ($E = E_0 + A\Lambda\Sigma$), just as in the fine structure splitting found in atoms.

Rotational levels in Hund's case (a) The system can, to first order, be regarded as a rigid rotor with an additional moment of inertia of the electron cloud around the internuclear axis. This type of molecule is called a symmetric top. The rotational energy levels are given by

$$F(J) = BJ(J+1) + (A - B)\Omega^2, \tag{2.18}$$

where B is the rotational constant due to the moment of inertia of the nuclei, and $A = h/(8\pi^2 c I_A)$ (not the same A as the fine structure splitting from the previous paragraph) is due to the small moment of inertia of the electrons rotating around the internuclear axis. This formula can be understood from the Hamiltonian

$$\hat{H} = \frac{\hat{N}^2}{2I_B} + \frac{\hat{\Omega}^2}{2I_A} = \frac{\hat{J}^2}{2I_B} - \frac{\hat{\Omega}^2}{2I_B} + \frac{\hat{\Omega}^2}{2I_A}. \tag{2.19}$$

The term $A\Omega^2$ is constant for a given electronic state and $B\Omega^2$ is constant for a given vibrational level in that electronic state. Together they determine the splitting between two Ω states of the same ${}^{2S+1}\Lambda$ multiplet. By convention [113], for a normal spectrum ($A > 0$), the level with highest energy is labeled F_2 and the lowest energy level is labeled F_1. For an inverted spectrum ($A < 0$), this is the opposite. For the $A\,{}^2\Pi$ doublet with a normal Ω splitting, the $A\,{}^2\Pi_{1/2}$ level is called F_1 and the $A\,{}^2\Pi_{3/2}$ level has the label F_2.

Λ-doubling The degeneracy of $\Lambda = \pm 1$ causes an energy splitting of states with labels J. For a $^2\Pi$ level, we have $S = 1/2$, $\Sigma = \pm 1/2$ and $\Lambda = \pm 1$. This yields the four possible combinations

$$\Sigma = \pm 1/2 \qquad \Lambda = \pm 1 \qquad \Lambda + \Sigma = \pm 3/2 \tag{2.20}$$

$$\Sigma = \mp 1/2 \qquad \Lambda = \pm 1 \qquad \Lambda + \Sigma = \pm 1/2 \tag{2.21}$$

In our case of a Hund's case (a) system, the doublet splitting between the $\Omega = |\Lambda + \Sigma| = 1/2, 3/2$ is large. Therefore, it is best to consider the $^2\Pi_{1/2}$ and $^2\Pi_{3/2}$ separately. For the $^2\Pi_{1/2}$ level, the states are labeled with quantum number J. Each of these states is split by the Λ-doubling into two states with $\Lambda = \pm 1$. The parity of these states is opposite and the order of the parity states alternates with J, as shown in Figure 2.6.

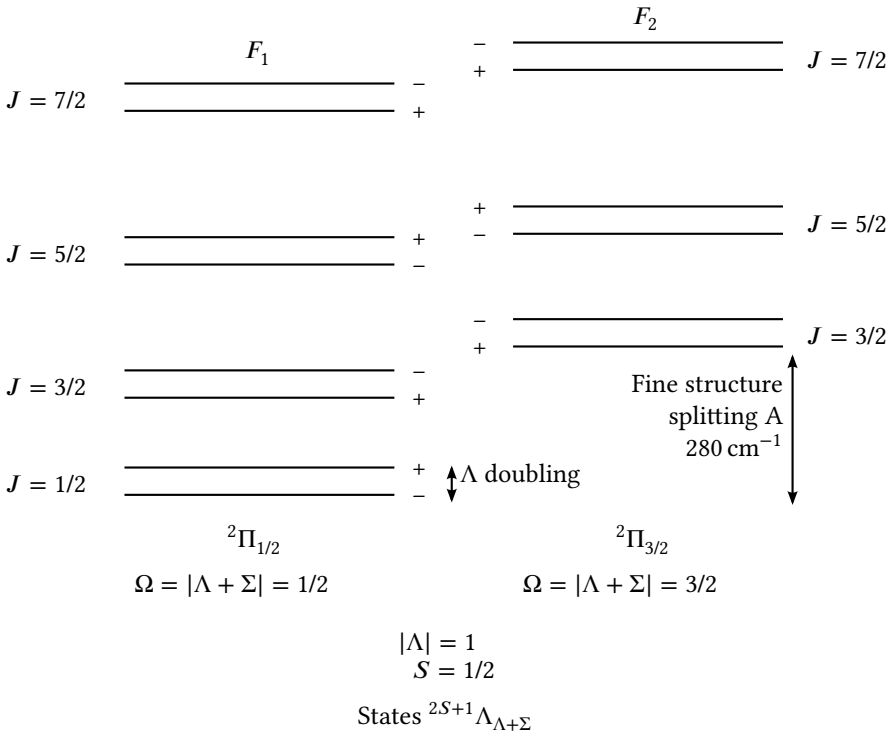

Figure 2.6: The $^2\Pi$ level in SrF. Being a typical Hund's case (a), the fine structure splitting is rather large.

2.2.4 Rotational spectra between $X\,^2\Sigma^+$ and $A\,^2\Pi_{1/2}$ in SrF

Following Herzberg [113], we summarize the lines in a rotational spectrum. For a transition between two particular vibrational states $v'' \leftarrow v'$ we can write the energy difference between the states as

$$\nu = T'_{e'} + G'_{v'} + F'_{v'} - T''_{e''} - G''_{v''} - F''_{v''}. \tag{2.22}$$

For a transition between v' and v'' the rotational dependence of the terms T and G can be safely ignored. This leaves us for the $A\,^2\Pi_{1/2} \leftarrow X\,^2\Sigma^+$ transitions with

$$\nu = \nu_0 + F'_1(J') - F''_{1,2}(J'') \tag{2.23}$$

where $\nu_0 = T'_{e'} - T''_{e''} + G'_{v'} - G''_{v''}$ is the frequency of the pure electronic-vibrational transition without any rotation. For the lower F_1 and F_2 terms, the values of J'' are $N + 1/2$ and $N - 1/2$. The rotational transitions between two J-levels follow the selection rule $\Delta J = J' - J'' = 0, \pm 1$. This allows us to drop a prime and only write down the lower level J'' quantum number as J. We then have six possible branches: P_1, P_{12} ($\Delta J = -1$), Q_1, Q_{12} ($\Delta J = 0$) and R_1, R_{12} ($\Delta J = +1$), where the indices indicate the F_1 or F_2 lower term. If we ignore the small vibrational dependence on the rotational constants such that $B'_{v'} = B''_{v''} = B$, and absorb the Ω-splitting in the constant ν_0, we can use Equations (2.17) and (2.18) to write Equation (2.23) for the six cases as:

$$P_1(J) = \nu_0 + B/4 - BJ - \gamma(J - 1/2)/2 \tag{2.24}$$

$$P_{12}(J) = \nu_0 - 3B/4 - 3BJ + \gamma(J + 3/2)/2 \tag{2.25}$$

$$Q_1(J) = \nu_0 + B/4 + BJ - \gamma(J - 1/2)/2 \tag{2.26}$$

$$Q_{12}(J) = \nu_0 - 3B/4 - BJ + \gamma(J + 3/2)/2 \tag{2.27}$$

$$R_1(J) = \nu_0 + 9B/4 + 3BJ - \gamma(J - 1/2)/2 \tag{2.28}$$

$$R_{12}(J) = \nu_0 + 5B/4 + BJ + \gamma(J + 3/2)/2 \tag{2.29}$$

The transitions are shown in Figure 2.7. We can see that the P-branches move from ν_0 towards lower frequencies, while the R-branches move towards higher frequencies. The $Q_{12}(J)$-frequencies follow the $P_1(J + 1)$ values but are slightly higher because of the spin-rotation splitting. The population distribution of the different rotational energy levels is governed by the Boltzmann distribution $n(T) = (2J + 1)e^{-E_J/k_B T}$. The intensity of a rotational line in a laser-induced fluorescence spectrum is proportional to the population in the lower state. Therefore, the intensities of the rotational lines in a measured rotational spectrum can be used to determine the rotational temperature of a molecular sample, as we see in Section 5.1.1.

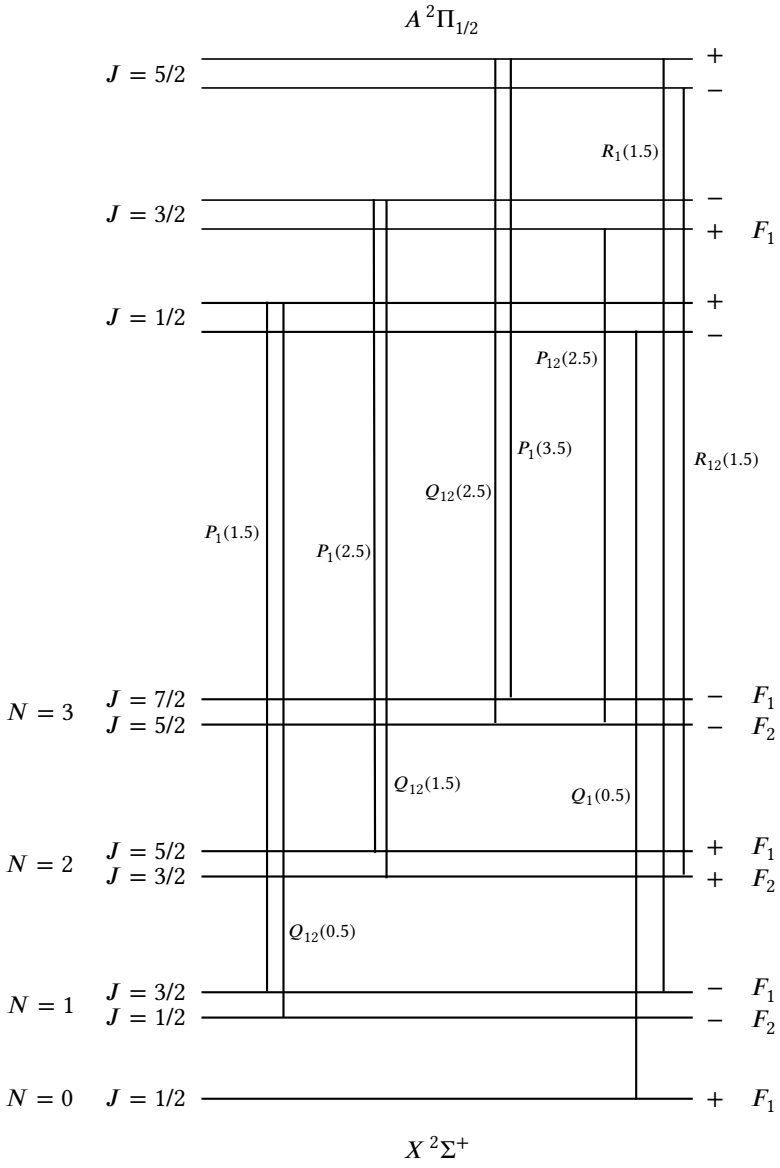

Figure 2.7: Rotational transitions between $A\,^2\Pi_{1/2} \leftarrow X\,^2\Sigma^+$ in SrF, relevant for the rest of this work. The Λ-splitting is in reality much smaller than indicated here.

3 | Traveling-wave Stark deceleration of SrF: simulations[1]

3.1 Stark deceleration of heavy diatomics

In order to address the challenge of the deceleration of heavier molecules a number of approaches has already been taken. The deceleration of molecules in a high-field seeking state (with minimum energy at maximum electric field) is possible using a multistage Stark decelerator operating in Alternating Gradient (AG) mode. From a number of proof-of-principle experiments that have been performed [102–104, 128, 129] it has become clear that the stability of such a decelerator depends very critically on the alignment of the electrodes, causing the efficiency to drop rapidly with decelerator length. Another very critical part would be the transfer from an AG decelerator to an AC trap that can trap the high-field seeking molecules.

Alternatively, the molecules can be decelerated in the weak-field seeking part of an excited rotational state [10], such as the SrF$(1, 0)$ state in Figure 2.2, using a multistage Stark decelerator. As only a limited electric field strength can be used, a long decelerator would be required. Unfortunately the coupling of longitudinal and transverse motion in a multistage decelerator reduces the phase-space acceptance considerably, which is problematic for long decelerators. A possible solution, especially if one does not have to reach standstill, is to use a different switching mode in the decelerator [94, 130, 131]. For heavy molecules,

[1] This chapter is based on J. E. van den Berg, S. H. Turkesteen, E. B. Prinsen, and S. Hoekstra, *Deceleration and trapping of heavy diatomic molecules using a ring-decelerator*, Eur. Phys. J. D **66**, 235 (2012) doi: 10.1140/epjd/e2012-30017-5.

however, this is not a viable solution, as the increased transverse stability is obtained by using the high electric fields in between the electrodes. Such high electric fields would drive the heavier molecules into the high-field seeking regime, which would lead to additional losses.

The purpose of the study presented here is to evaluate the performance of a traveling-wave Stark decelerator using ring-shaped electrodes (called traveling-wave decelerator) for the deceleration and trapping of heavy diatomic molecules in weak-field seeking states. In a recent experiment with this type of decelerator the deceleration of CO in the metastable $a^3\Pi_1$, $J = 1$ state has been demonstrated [11]. As was mentioned in [11], a traveling-wave decelerator is promising for heavy diatomic molecules because the molecules remain confined during the deceleration process in a trap with limited electric field strength. A second advantage is the stability of the deceleration process, which allows for the construction of efficient long decelerators. Finally, losses in the transfer from the decelerator to a separate trap [132] are avoided, because molecules can be stopped and trapped by the same electrodes that form the decelerator. We have picked the SrF molecule as the prototype molecule for our simulations, because it is predicted to be a sensitive probe for molecular parity violation [16], because it has a reasonable electric dipole moment (3.5 Debye), rotational moment and corresponding Stark shift, and because is not too heavy so that it can still be decelerated in a reasonable size decelerator.

3.2 Traveling-wave deceleration of SrF

3.2.1 Principle of operation

Here we explain the operational principle of a traveling-wave decelerator based on the review by Van de Meerakker et al. [22]. For more details we refer to the existing literature on this type of decelerator [11, 93]. A large number of ring-shaped electrodes (depending on the length of the decelerator a few hundred to a few thousand) are mounted in a periodic array such that every ninth electrode is at the same voltage. The eight sets of electrodes are connected to 8 high-voltage supplies. Oscillating voltages $V_n(t) = V_0 \sin(-\phi(t) + 2n\pi/8)$; $n = 0, 1, \ldots, 7$ are applied to these sets of ring electrodes with a phase-difference of $2\pi/8$ and a common varying phase $\phi(t)$. The electrodes thereby sample a sinusoidally varying electric potential along their longitudinal axis. This electric potential configuration yields two electric field minima per period of 8 rings on their central axis. The electric field gradient at the location of these minima is such that low-

field seeking molecules are confined in both radial and longitudinal directions. These potential minima (potential wells) are therefore three-dimensional traps for low-field seeking molecules. For a constant phase ϕ the potential wells are static. They can be translated at a constant speed by varying $\phi(t)$ linearly. When the voltages on the electrodes are modulated at a frequency $f(t)$, the phase can be expressed as $\phi(t) = 2\pi \int_0^t f(\tau)\,\mathrm{d}\tau$. As one oscillation period moves the traps by one decelerator period of 8 rings with length L, the instantaneous velocity of the traps is $v = f(t)L$. By chirping the frequency, the traps can be decelerated or accelerated. In Figure 3.1 lines of equal electric field strength are drawn on a longitudinal cut through a section of the decelerator for an applied voltage $V_0 = 8\,\mathrm{kV}$. The electric field dependence of the Stark shift determines the shape of the trapping potential created by this electric field. As the frequency of the applied voltage determines the velocity of the moving traps, the amplitude determines the depth of the traps. Initially, as the molecules enter the decelerator, the traps are set to move at the same speed as the molecules. Then, gradually, the oscillation frequency of the voltages is swept down resulting in the deceleration and ultimately stopping of the traps, with (a fraction of) the molecules remaining in these traps.

The deceleration of the traps can be added as a pseudo force to the force that the molecules experience in the frame of the moving traps, as shown in Figure 1.5b. With increasing deceleration strength the addition of the deceleration force in the form of a potential reduces the trap volume, until a maximum deceleration force is reached that is equal in strength to the trapping force. This is shown in Figure 3.2. At this point the acceptance of the decelerator is reduced to zero. Therefore, to stop a molecule in a specific state with a given initial velocity, a minimum length of the decelerator is required. Increasing the length of the decelerator beyond this minimum will increase the fraction of decelerated molecules. An important difference between a traveling-wave decelerator and a multistage Stark decelerator is the stability in long decelerators: we discuss this in more detail in Section 3.3.

3.2.2 Parameters and input for the simulations

Using finite-element calculational methods we have determined the time and position dependent electric field in the decelerator. Cylindrical symmetry is used to speed up the calculations. The electric fields are assumed to be periodic in the decelerator structure. We sample the movement of the traps due to an entire sinusoidal period in 80 frames. Edge-effects such as distortions of the electric field

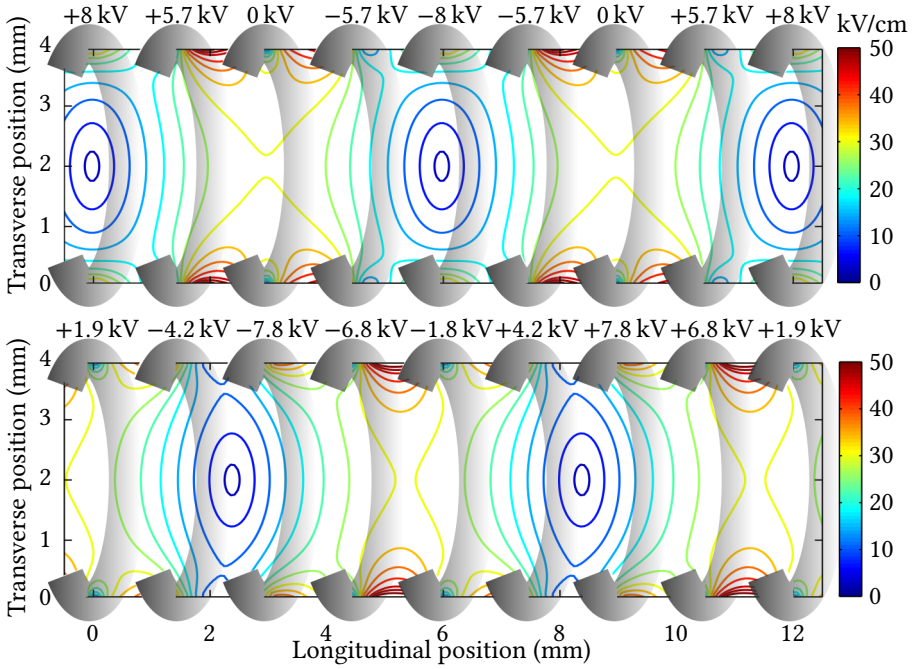

Figure 3.1: Lines of equal electric field strength show the electric field minima in this longitudinal cut through a section of the decelerator for two different phases ($\phi = \pi/2$ and $\phi = 0.71 \times 2\pi$) of the traveling wave of 8 kV amplitude. The numbers above the rings indicate the applied voltage on that ring. The minima move through the decelerator with a velocity that is determined by the oscillation frequency of the potential on the electrodes. During this movement, the shape of the contour lines, and thereby the shape of the traps, changes as described in the text.

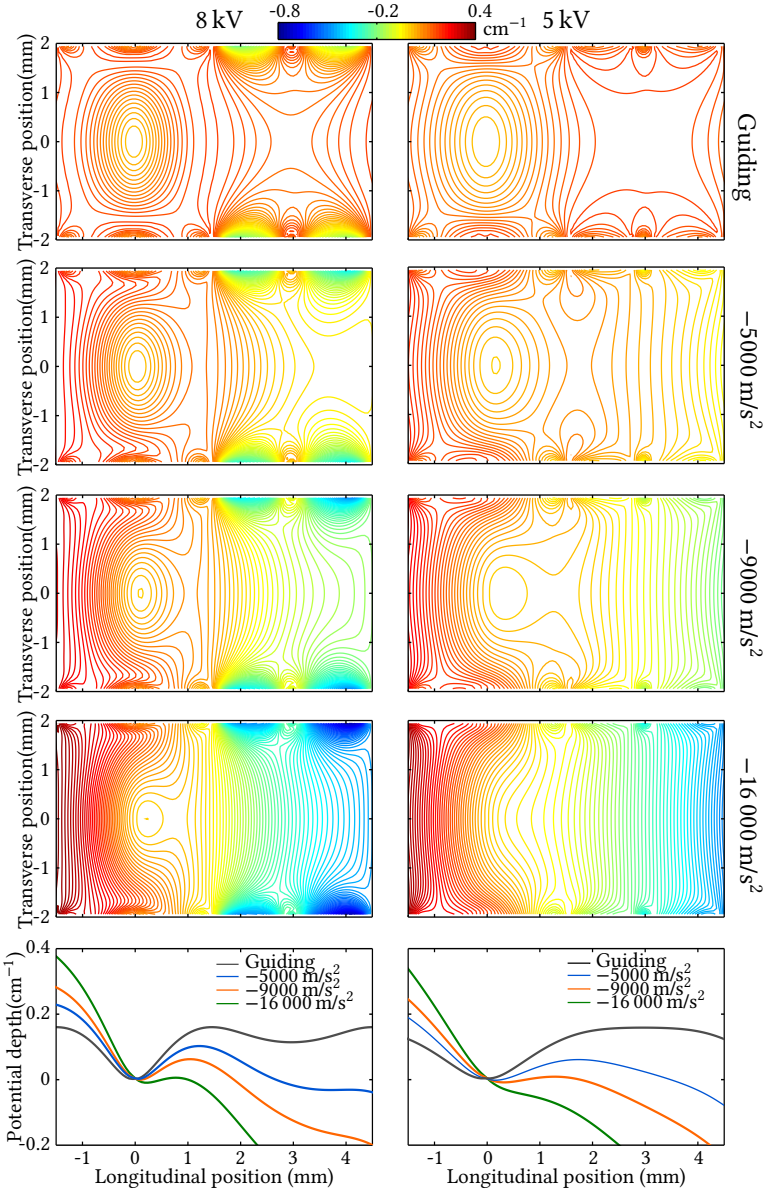

Figure 3.2: Potential depth for SrF(1, 0) molecules in a decelerating frame for 8 kV (left) and 5 kV (right). The 8 figures on top show a 2D-contour plot through the longitudinal plane of the decelerator for different deceleration strengths. The two bottom figures show the potential depth along the axis of the decelerator. It can be seen that the traps get shallower at higher deceleration strengths.

lines at the entrance of the decelerator are not present in the simulations but are expected to play a role in the experiment. We have not taken into account intermolecular collisions or collisional loss through interactions with the background gas. Since the pressure in the decelerator chamber is of order $<1 \times 10^{-7}$ mbar, collisions with background gas can safely be neglected [84]. Using the Stark shift of the molecular state the electric field map is transformed to a potential, from which the force is derived. The trajectory of the molecules through the decelerator is then calculated numerically using MATLAB [133]. By comparing to the experimental results [11] on the traveling-wave deceleration of CO we could check the validity of our simulation code.

Our group performed numerical simulations to determine the optimal dimensions for the decelerator [134]. The optimal value for the inner diameter of the ring electrodes is 4 mm, the electrodes have a thickness of 0.6 mm, and the center-to-center spacing of the electrodes is 1.5 mm. These dimensions correspond to the traveling-wave decelerator that has been used to decelerate CO [11]. The applied voltage to a set of electrodes is a sine wave with an amplitude that we have varied in the simulation over a range from 5 kV to 8 kV (peak-to-peak voltage of 10 kV to 16 kV). The availability of suitable high voltage supplies to operate the decelerator will determine the voltage that can be applied in actual experiments. Between each of the 8 sets of electrodes a phase shift of $2\pi/8$ is applied. We have calculated the deceleration process for various $(N, M = 0)$ states of the SrF molecule, denoted in the following text as SrF$(N, 0)$. The Stark shift of SrF is calculated with the aid of PGOPHER [119] and molecular parameters available from literature [121, 135–137].

3.2.3 Total 1D phase-space acceptance

As a first assessment of the performance of the decelerator for SrF we have calculated the phase-space acceptance of the decelerator, as a function of the applied voltage and deceleration strength. In this first step we have neglected 3D effects. Further on in this chapter we will discuss such effects of coupling between the longitudinal and transverse motion. The longitudinal 1D acceptance is calculated as the area within the phase-stable area, called the separatrix. Molecules within this area will oscillate longitudinally around the trap center and are kept together during the deceleration process. Molecules outside this area cannot be decelerated in a phase-stable manner. A similar procedure is used to obtain the transverse 1D phase-space acceptance. The resolution for the 1D-separatrix is 0.1 m/s per axis and is limited by the discrete set of starting velocities used. The

product of the areas in phase-space within the region bounded by the three 1D separatrices we call the total 1D phase-space acceptance.

Guiding

The guiding of molecules at constant velocity is the mode of operation of the decelerator with the highest phase-space acceptance. The longitudinal and transverse separatrices for the guiding of SrF(1, 0) and SrF(2, 0) are plotted for different applied voltages in Figure 3.3. The traps, with a size of about 4 mm × 4 mm, can typically confine molecules with a velocity of between 5 m/s and 10 m/s relative to the guiding traps. For SrF(1, 0) the peculiar situation arises that for *increasing* voltage (in the range of 5 kV to 8 kV) the acceptance *decreases*, which is a consequence of the particular shape of the Stark curve. The result is a spatial compression of the trap for higher voltages. For guiding with the chosen geometry 5 kV has the highest acceptance, as for 4 kV (not shown) the maximum of the Stark curve is not yet reached. For SrF(2, 0) the situation is reversed, as can be seen in Figure 3.3. For this state the maximum of the Stark shift has not yet been reached at the applied voltages; therefore the acceptance volume keeps growing with increasing voltage. There is a dependence of the 1D acceptance on the position relative to the electrodes in the decelerator, as depicted in Figure 3.1. During guiding, the molecules therefore see the trap shape oscillating. If this oscillation frequency is comparable to the trap frequency, parametric heating can occur, leading to losses. We found a trap frequency of 100 Hz–200 Hz, and this corresponds to a trap movement of much less than 10 m/s. Simulations showed that the largest loss was for molecules traveling at 4 m/s and amounted to 7 % after guiding for 33 ms at this velocity [134]. This speed is in practice only reached at the very end of the deceleration process such that the molecules will have this velocity for much less than a millisecond. Hence, the losses due to the changing trap shape can be safely assumed to be less than 5 %.

Decelerating

When operating the device in deceleration mode, the acceptance is decreased compared to guiding. The amount depends on the deceleration strength, the state of the molecule, and the applied voltage. For a range of deceleration strengths we have calculated the total 1D phase-space acceptance, for both the SrF(1, 0) and SrF(2, 0) states. The results are summarized in Figure 3.4. For SrF(1, 0) it can be seen that with increasing deceleration strength the initially relatively high

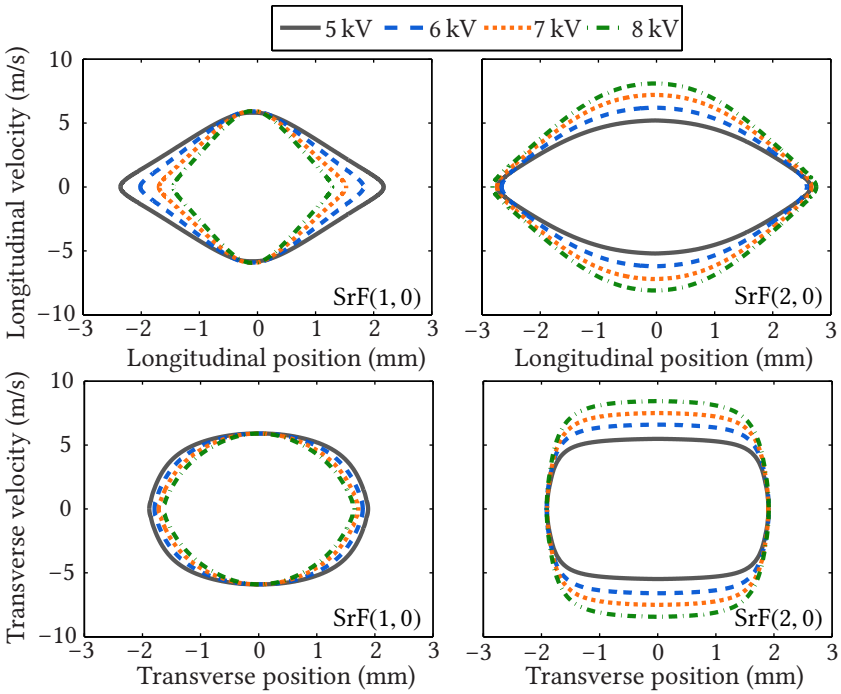

Figure 3.3: Longitudinal and transverse 1D separatrices for SrF(1, 0) and SrF(2, 0) for guiding, for four different applied voltages.

acceptance for low voltages is reduced, until around a deceleration of 8000 m/s^2 the total acceptance for deceleration of SrF(1, 0) is practically independent of the applied voltage. This can be understood from the steeper slope of the trapping potential (at the cost of a smaller trap volume) for the higher voltages. For SrF(2, 0) the situation is simpler. At low deceleration strengths and high voltages the acceptance for SrF(2, 0) is about 10 times larger than for SrF(1, 0), whereas for the very high deceleration strengths SrF(1, 0) has a slightly higher acceptance. This difference in the acceptance at very high deceleration strengths between the SrF(1, 0) and SrF(2, 0) level reflects the difference in the slope of the Stark curves.

With a deceleration strength of 9000 m/s^2 a beam of SrF molecules with an initial velocity of 300 m/s (which can be reached in a cooled supersonic expansion using xenon as a carrier gas) can be stopped using a five meter long decelerator. This length is similar to that needed for alternative deceleration approaches. The typical length of multistage Stark decelerators for light molecules such as OH, NH_3 and CO is around one meter.

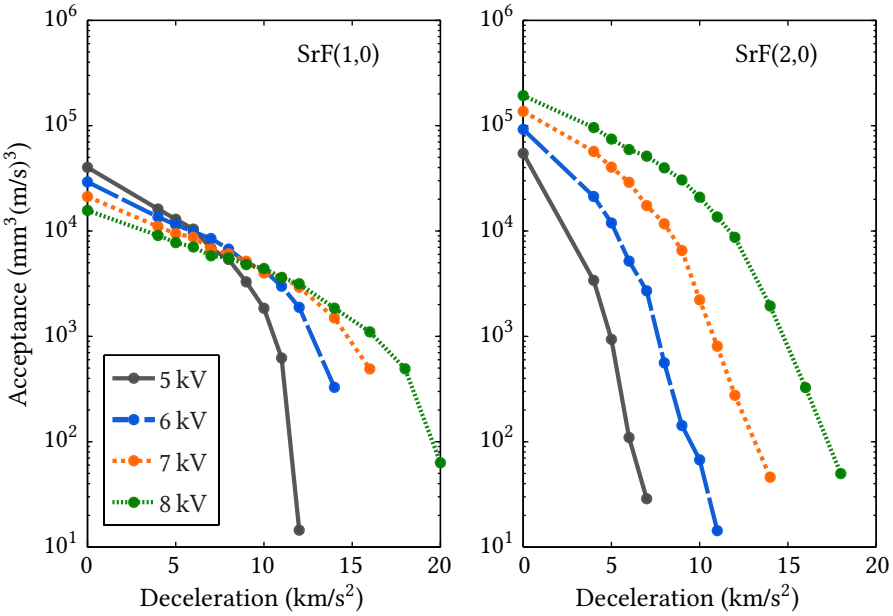

Figure 3.4: The total 1D acceptance of the traveling-wave decelerator for SrF(1, 0) and SrF(2, 0), as a function of deceleration strength, for different applied voltages. In this calculation there was no coupling between the longitudinal and transverse motion.

3.2.4 Total 3D phase-space acceptance

In this section we present a full 3D calculation of the deceleration of SrF molecules using a traveling-wave Stark decelerator. It has been shown for multistage Stark decelerators [94, 131] that molecules are lost from within the 1D separatrices during the deceleration process due to coupling of the longitudinal and transverse motion. This effect leads to larger losses for longer decelerators. There is also a minimum length required to stop a reasonable fraction of the molecules. For multistage decelerators there exists therefore an optimum length to reach a desired final velocity. A furthermore especially critical part is around low velocities where the molecules are transversely over-focused and hit the electrodes. The situation for a traveling-wave decelerator is quite different, as is illustrated by Figure 3.5. Here the result of a full 3D calculation is compared to the calculated 1D longitudinal acceptance, for the SrF(2, 0) state with a deceleration strength of 9000 m/s^2 and 8 kV applied voltage. The fact that almost the complete 1D separatrix is uniformly filled by the particles illustrates the stability of the deceleration

process in the traveling-wave decelerator.

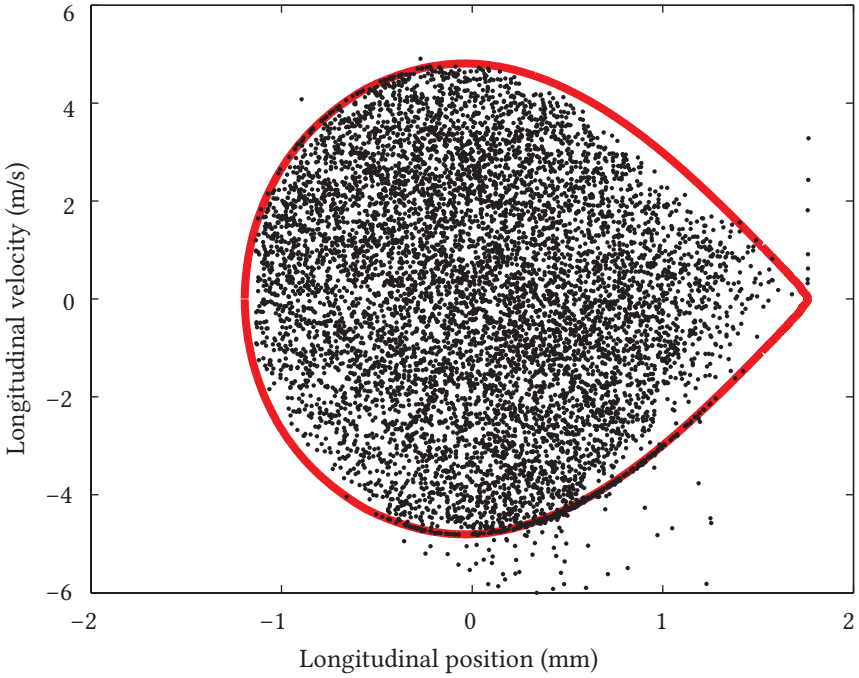

Figure 3.5: The 1D longitudinal separatrix for the deceleration with 9000 m/s^2 of SrF(2, 0) at 8 kV (red solid line), with the result of a full 3D simulation of 50 000 molecules (black dots). The fact that almost the complete 1D separatrix is uniformly filled by the particles illustrates the stability of the deceleration process in the traveling-wave decelerator.

For every datapoint in the 3D acceptance simulations shown in Figure 3.6 we used 5000 molecules distributed over the 1D separatrix acceptance. The results of the 3D acceptance calculations have a statistical scatter of 5 %–10 %.

Over 75 % of the molecules that started within the total 1D acceptance make it to the end in this 5 m long decelerator. Some molecules are lost through collisions with the ring-shaped electrodes, or escape longitudinally over the potential barrier. The small phase-space reduction caused by the movement of the trap as it moves along the electrodes clearly does not lead to large losses. This high stability is a key issue for the good performance of long traveling-wave decelerators for heavy diatomic molecules.

In Figure 3.6 the total 3D acceptance of the traveling-wave decelerator for

SrF(1, 0) and (2, 0) is shown, as a function of stopping distance, for 5 kV and 8 kV. For a fixed initial velocity of 300 m/s the deceleration strength is varied, leading to a different decelerator length in order to reach a standstill. This is the result of a full 3D simulation, allowing for coupling between the longitudinal and transverse motion. We uniformly and randomly fill the total 1D acceptance volume at the beginning of the simulation, and then track the fraction of molecules that remain within this volume. The total acceptance that is shown on the vertical axis is the product of the total 1D acceptance cubed as it is plotted in Figure 3.4 and the fraction of molecules that remain within the 1D separatrices throughout the full 3D calculation. The performance for an applied voltage of 8 kV is clearly superior to 5 kV, especially when using SrF(2, 0). Comparing SrF(2, 0) at 8 kV to SrF(1, 0) at 5 kV, the same acceptance can be reached for a 3 m long decelerator instead of a 5 m long decelerator. If a 5 m long decelerator would be used at 8 kV for SrF(2, 0), the total acceptance is 20 times higher than for 5 kV SrF(1, 0).

3.3 Comparison to other deceleration approaches

In this section we compare the results on traveling-wave deceleration that we presented in the previous paragraphs to the two different approaches that can be taken to decelerate heavy diatomic molecules: alternating gradient (AG) deceleration and multistage Stark deceleration in a weak-field seeking (WFS) excited rotational state. Multistage Stark deceleration in the $s = 3$ overtone mode does not seem a viable option, because the losses for velocities below 150 m/s are too severe [94]. Since no heavy molecules have been fully stopped or trapped yet, we rely on the results of simulations. The two alternative methods have been compared for YbF molecules by Tarbutt et al. [10]. The data from their simulations are plotted in Figure 3.7. It shows the decrease in the acceptance for a given deceleration strength as the molecules travel through the decelerator. The deceleration strength is sufficient to reach a low enough velocity that the molecules could be loaded into a trap. The final two datapoints at around 5 m are also included in Figure 3.6. For the WFS deceleration a multistage decelerator with a gap of 4 mm square and an applied voltage of $\pm$40 kV was assumed, for the AG deceleration the same voltage difference was used. For the WFS simulation the YbF(5, 0) molecules were taken; since normally in the supersonic expansion this state is barely populated special microwave pumping schemes would have to be used before entering the decelerator. For both deceleration techniques about 5 meter of decelerator is required to bring the molecules to a sufficiently low ve-

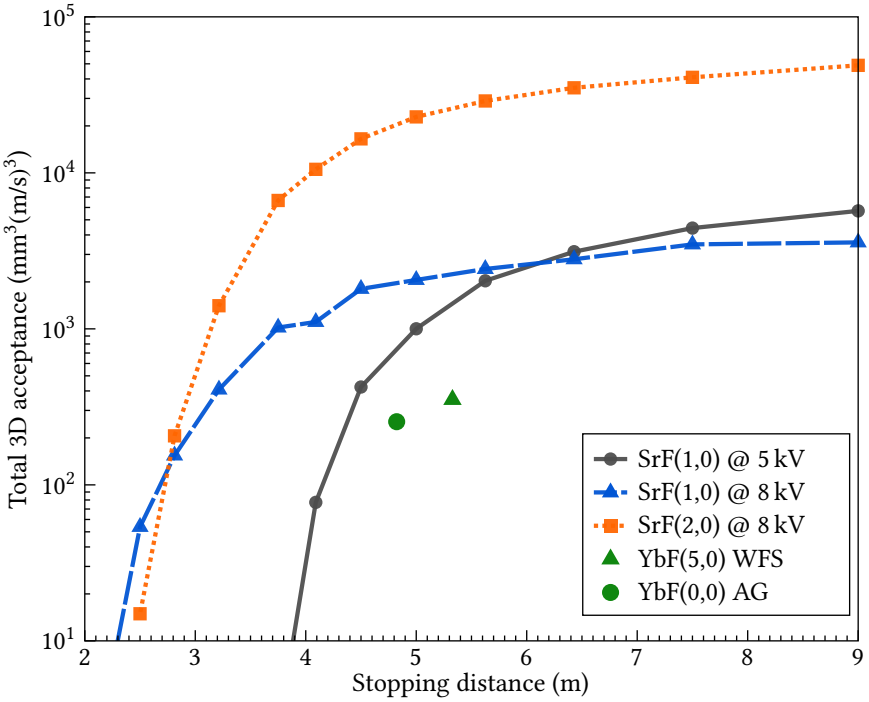

Figure 3.6: The total 3D acceptance of the traveling-wave decelerator for SrF(1, 0) and SrF(2, 0) as a function of the stopping distance, for two different applied voltages. The deceleration strength is varied leading to different stopping distances to stop and trap the molecules from an initial velocity of 300 m/s. The two points denote calculation results [10] for other deceleration methods, which are discussed in the text.

locity such that they can be trapped. The decrease in acceptance is due to lens aberrations, suboptimal focusing, and coupling of longitudinal and transverse motion [10]. The electrode alignment in an AG decelerator is therefore very critical. We have used our simulation code to quantify the effects of misalignment in the traveling-wave decelerator and found the alignment errors to be less critical and well under control [134], as described in more detail in Chapter 4.

The data from the simulation of the traveling-wave deceleration of SrF is also plotted in Figure 3.7. Here, the acceptance is obtained just as in [10] by multiplying the initial 3D acceptance with the fraction of molecules that remains inside the acceptance region after having flown a certain distance inside the decelerator. Direct quantitative comparison between the different deceleration methods

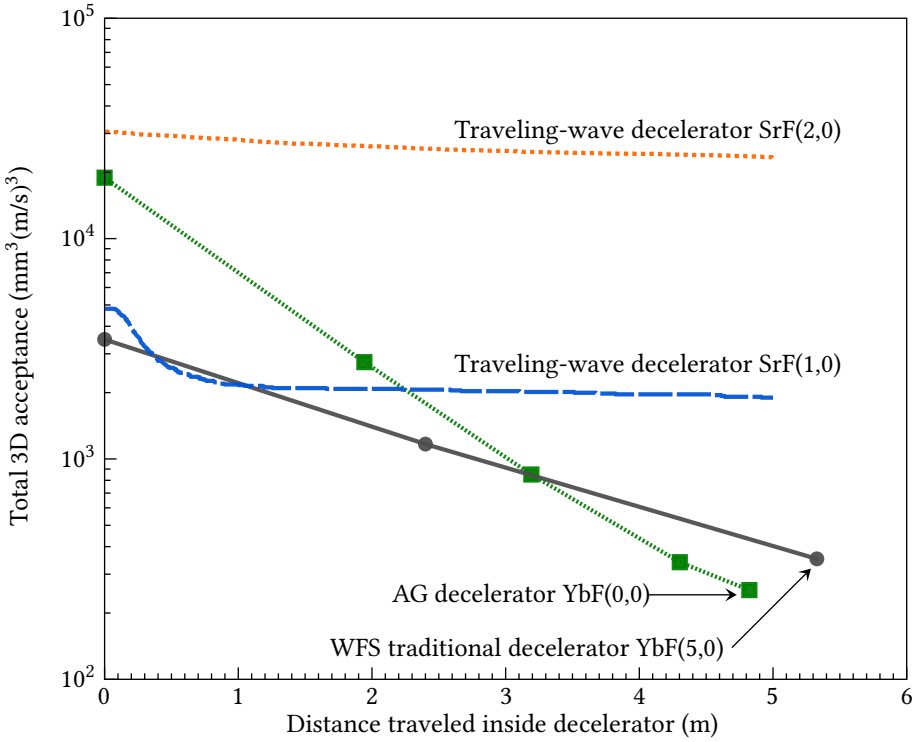

Figure 3.7: A comparison of the decrease of the calculated total phase-space acceptance during the deceleration process for different types of decelerators for heavy diatomic molecules. For the traveling-wave decelerator the acceptance for the SrF$(1,0)$ and SrF$(2,0)$ states at ± 8 kV is shown (this work). The acceptances for the other decelerator types have been calculated by Tarbutt et al. [10]. The alternating gradient (AG) deceleration data is for YbF in the $(0,0)$ state, the weak-field seeking (WFS) multistage deceleration is for YbF in the $(5,0)$ state. For both decelerators the total length required to decelerate the molecules to a velocity that can be trapped is about 5 m, the initial velocity is 340 m/s, and the applied voltages are ± 40 kV.

is limited because the performance of the decelerators depends very strongly on the electrode geometry and decelerator length, the applied voltages, the molecule and which state is used. This can be seen in Figure 3.6. Nevertheless, it is clear from these figures that the traveling-wave decelerator can outperform these alternative methods by at least an order of magnitude while using much lower electric field strengths. The main reason for this is that during the deceleration

process a much larger fraction of the molecules remains trapped, due to the high phase-space stability in the traveling-wave decelerator.

3.4 Trapping

At the end of the deceleration process the moving trap, including the molecules, is brought to a standstill. The molecules remain trapped in the last section of the decelerator, where further experiments can be performed. As a result there are no additional losses of molecules in the transfer from the decelerator to the trap. For multistage decelerators this step can lead to substantial (factor 4–6) losses [132]. For heavy diatomics the depth of the trap is limited by the maximum energy at the turning point of the Stark curve: for SrF$(1, 0)$ this is $0.15\,\mathrm{cm}^{-1}$ for guided molecules and $0.0083\,\mathrm{cm}^{-1}$ for SrF$(1, 0)$ decelerated at $9000\,\mathrm{m/s}^2$. A decelerated SrF molecule with this maximum kinetic energy moves at 1.4 m/s, which is the most probable velocity for a gas at a temperature of 12 mK. Operating the trap at higher voltages will, due to the special shape of the Stark curve for SrF in the $(1, 0)$ state, not lead to a deeper trap, but to a trap with the same depth and a reduced volume. To further reduce the temperature either sympathetic cooling (which has so far only been analyzed for lighter systems [138–140]) or direct laser cooling techniques need to be further explored. Recently laser cooling of SrF has been shown [107, 141], in the first demonstration of the laser cooling of a molecule. We would further like to remark that the effect of blackbody radiation on the trapped molecules [98, 142] is only significant on timescales larger than one second.

3.5 Using decelerated molecules for precision measurements

As pointed out in Chapter 1, cold molecules can be used to perform very sensitive precision measurements concerning fundamental physics questions. Here we will briefly discuss the gain in statistical sensitivity that can be obtained by our deceleration technique. The use of a Stark decelerator to make slow molecular beams that allow for longer, more precise measurements, was first reported by Van Veldhoven et al. [143] in a spectroscopic measurement on the hyperfine structure of $^{15}ND_3$. A parity violation measurement in molecules using a Stark-interference technique was proposed by DeMille et al. [16]. The statistical uncertainty of such an experiment scales as $\sigma \sim 1/\sqrt{N\tau}$, where N denotes the

number of molecules and τ the coherent measurement time.

In order to compare the flux of molecules with a molecular beam experiment we first estimate the number of trapped molecules. As the SrF source is very similar to the YbF source reported on in [86], we assume that the same ground state beam flux of 1.4×10^9 molecules/sr can be achieved for SrF(1, 0). Accordingly, 2.4×10^6 molecules would pass the skimmer per shot. Taking into account the reduced acceptance for decelerating at 9000 m/s^2 from Figure 3.4, we estimate that 1 % of these molecules can be decelerated. Since no more molecules are lost upon trapping, we expect to achieve $\sim 10^4$ trapped SrF(1, 0) per shot. For operation of the decelerator at 10 Hz repetition rate this corresponds to a flux $N = 10^5$/s. This number is therefore comparable to the proposed cryogenic molecular beam experiment [16], and reflects just the flux of molecules. Trapping the molecules enables detection of multiple photons per molecule, which increases the statistical sensitivity as compared to a molecular beam experiment.

We now consider the potential gain in interaction time. Since the environment of an electrostatic trap introduces a number of challenges for precision experiments, the use of slow and/or laser-cooled (but not trapped) molecules is currently the most promising approach, although the combination of laser-cooled molecules and a deep trap, where the molecules would only sample the very central, homogeneous part of the trapping fields, is also worth investigating [10]. In a molecular beam experiment the interaction time τ is limited by the longitudinal velocity of the beam and the length of the interaction region that it traverses. For a typical cryogenic beam velocity of $v_\parallel = 140$ m/s, $v_\perp = 28$ m/s [20], and a measurement region of 50 mm × 5 mm × 5 mm [16], this results in $\tau = 0.3$ ms. The transverse velocity determines the size of the molecular beam at the exit of the measurement region. For a measurement region length of 50 mm and a beam with $v_\parallel \geq 10 \times v_\perp$, the transverse size increase of the beam is limited to ≤5 mm. The cryogenic beam of [20] has a larger transverse velocity, which limits the number of molecules that can fully exploit the whole length of the measurement region. As pointed out in the previous section, the decelerated packets of molecules have a velocity of ≤1.5 m/s. To make use of these molecules while keeping them in the 50 mm × 5 mm × 5 mm interaction region we would have to give the packet of molecules a longitudinal velocity of ∼15 m/s. This results in a modest gain in the interaction time of a factor of eight. Clearly, one can only make significant gains in the interaction time using molecular beams if the transverse velocity is also significantly reduced. This can be achieved by laser cooling of the decelerated molecules, by which the temperature can be expected to be

reduced to the Doppler temperature $T_D \sim 150\,\mu K$. At this temperature the most probably velocity is 0.17 m/s, indicating that a longitudinal velocity of 1.7 m/s would be sufficient to keep the beam within the above mentioned size criteria, resulting in an interaction time increase by a factor ∼75. However, in practice it turns out that temperatures well above the Doppler limit must be expected, as shown by the MOT experiment which yields a temperature of $T = 2.4\,mK$ [18]. It would therefore be more convenient to change the experimental geometry to an empty cube-shaped measurement zone with edge size 50 mm. This is better suited for ballistic expansion of the released cloud of molecules. Then, the interaction time would be 17 ms for the 12 mK trapped sample, and 150 ms for the 0.15 mK laser cooled sample. This corresponds to a gain in τ of 40 and 370, respectively.

Table 3.1: An overview of the possible coherence times for a parity violation measurement. The first entries give the time of flight of a beam trough an interaction zone of 50 mm × 5 mm × 5 mm. The last two entries describe a ballistically expanding cloud of molecules in a cubic interaction zone of 50 mm × 50 mm × 50 mm.

Experiment	T/mK	$v_\parallel$/(m/s)	$v_\perp$/(m/s)	τ/ms
Slow beam [20]	-	150	28	0.4
Decelerated	15	15	1.5	3.3
Decelerated, laser cooled	0.15	1.7	0.17	30
Trapped	15	-	1.5	17
Trapped, laser cooled	0.15	-	0.17	150

3.6 Deceleration of other molecules

Following this analysis of the deceleration of SrF molecules in a three to five meter long traveling-wave decelerator, we turn to an assessment of the deceleration of other relevant molecules. The alkaline-earth monohalides CaF, BaF and also YbF all have an $X\,^2\Sigma^+$ ground state with a similar Stark shift as SrF. For the $(1, 0)$ states we assume that a sufficiently high voltage can be applied such that the maximum of the Stark curve is limiting the acceptance. It can be seen from Figure 2.2 that the maximum value of the Stark shift is proportional to the rotational constant B only. When the full Stark energy can be used, the decelerator

length is independent of the electric dipole moment of the molecule. Therefore, the required length of the decelerator to reach a comparable deceleration efficiency as for SrF(1, 0) is proportional to the ratio of the mass and the rotational constant. For RaF we do not have the complete information for an estimate [17]. The results are given in Table 3.2.

Table 3.2: Traveling-wave deceleration of other alkaline-earth monohalides in the $X\,^2\Sigma^+\, v = 0$, rotational (N, M)-states and PbF in the $X^2\Pi_{1/2}\, v = 0$, (J, M) e-parity state.

Molecule	Mass/ u	μ_e/ Debye	B/ cm^{-1}	Relative length
CaF(1, 0) [120]	59	3.07	0.34	0.4
SrF(1, 0) [121, 122]	106	3.49	0.25	1
BaF(1, 0) [123, 124]	156	3.17	0.21	1.8
YbF(1, 0) [125]	192	3.91	0.24	1.9
PbF(3/2, 1/2) [126]	226	3.5	0.23	2.0

Deceleration is not restricted to molecules in $^2\Sigma$ states. For example, the deceleration of PbF in the $X\,^2\Pi$ state appears to be promising, as a Stark shift of $\sim$0.2 cm^{-1} is reached at moderate electric fields of 34 kV/cm. And finally we point out that also for the lighter molecules a long traveling-wave decelerator would compare favorably to existing Stark decelerators, if one wants to go to very low velocities. For example, we have employed a traveling-wave Stark decelerator in combination with a multistage Stark decelerator to bring a sample of ammonia molecules to standstill [73], fully exploiting the stability and versatility of a traveling-wave decelerator [74].

3.7 Conclusions and outlook

In this chapter we have presented a quantitative study of the deceleration and trapping of heavy diatomic molecules using a traveling-wave Stark decelerator. Trapped samples of such molecules are very promising for the study of the violation of fundamental discrete symmetries. For a selected prototype molecule, SrF, we show that a 5 meter long decelerator with modest voltages applied (amplitude of 8 kV) has a total phase-space acceptance for deceleration in the second excited rotational state of about 2×10^4 $mm^3(m/s)^3$. This is at least one order of magnitude larger compared to alternative deceleration methods using a similar

decelerator length and deceleration strength, but operating at much higher voltages ($\pm$40 kV).

We have estimated the potential gain in sensitivity of using the decelerated molecules for a parity violation measurement. Compared to a cryogenic molecular beam experiment, the decelerated molecules provide a gain in sensitivity of up to two orders of magnitude due to the increased interaction time, while maintaining a comparable molecular flux. By combining this efficient form of Stark deceleration with a final laser cooling stage a robust method to create ultracold trapped samples of heavy diatomic molecules is within reach. Based on the results calculated in this chapter, we have set forward to build a 5 m long traveling-wave Stark decelerator, which will be described in the next chapter.

4 | Experimental setup

In this chapter we describe the experimental setup that was built in our laboratory in order to decelerate SrF molecules. The device consists of a source chamber where the supersonic molecular beam is produced, the decelerator where the molecules are slowed down, and finally a detection chamber where the molecules are detected with laser light. A schematic overview of the experiment is given in Figure 4.1.

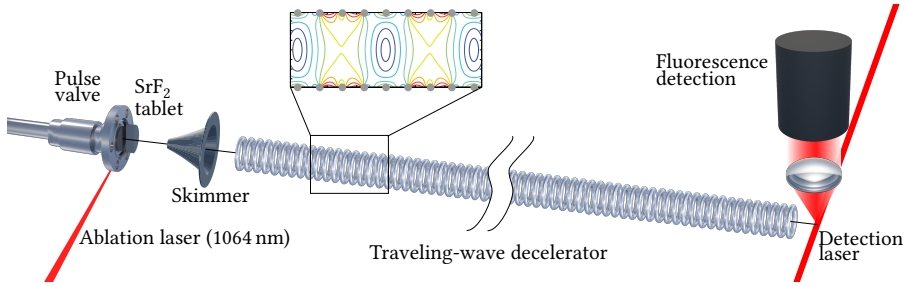

Figure 4.1: A schematic overview of the experimental setup. SrF molecules are created by laser ablation from a tablet. A pulsed supersonic xenon expansion cools the SrF molecules and takes them to the ring structure where the molecules are guided or decelerated. Further downstream SrF molecules are detected by laser induced fluorescence.

4.1 Source chamber

Historically, large source chambers with large vacuum pumps have been used in molecular beam experiments in order to provide enough pumping capacity to maintain a reasonable vacuum pressure. It was pointed out by Jansen et al. [144] that a small chamber with turbomolecular pumps covering most of the wall sur-

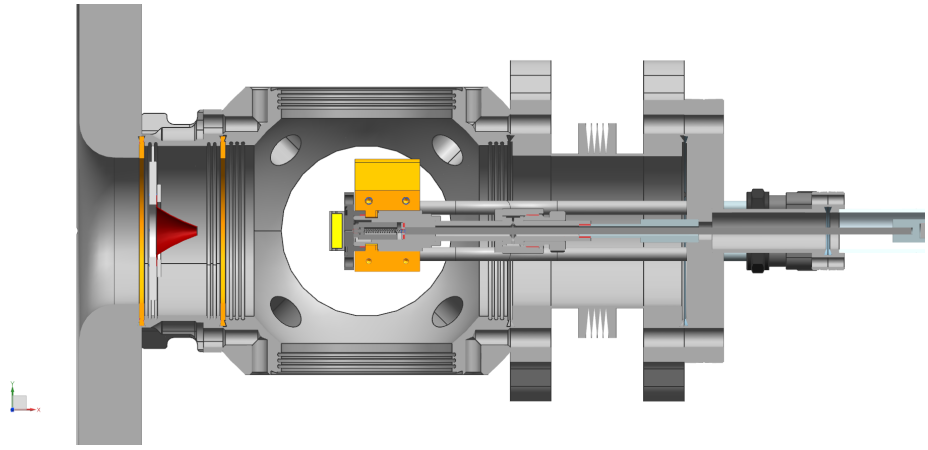

(a)

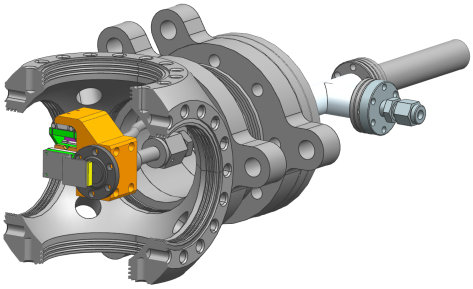

(b)

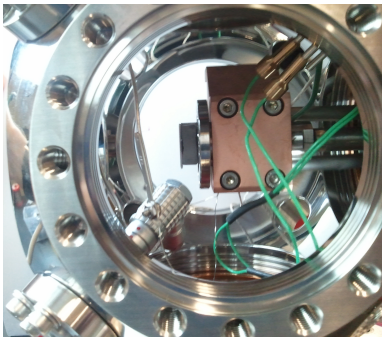

(c)

Figure 4.2: Drawings (a, b) and a photo (c) of the source chamber. Inside the CF63 spherical cube is the pulse valve which is enclosed in a copper block that is used for cooling. At the exit of the valve the sample consisting of a compressed mixture of 90 % SrF_2 and 10 % B is mounted on a piezo translation stage. The molecules exit the chamber through a 2 mm diameter aperture skimmer (red in (a)).

faces is a much more cost effective and more compact alternative. We have built such a compact source chamber (CF63 Kimball Spherical Cube) in which we create a supersonically expanding beam of SrF in Xe. A picture showing the inside of the chamber is shown in Figure 4.2. A 100 mJ, 5 ns pulse from a Q-switched Nd:YAG laser (Quantel Brilliant) at its fundamental wavelength of 1064 nm with a beam spot size of around 0.5 cm is used to ablate SrF radicals from the cutting edge of a homemade tablet sample, pressed with 30 kN for two hours, cleaved in half, consisting of 90 % SrF_2 and 10 % B. The addition of boron is found to make the tablet much more stable [145]. We mounted the tablet on a piezo-electrical translation stage (Smaract SLC-1720) to be able to optimize the tablet position and to provide a fresh ablation spot after a number of laser shots in order to prevent wearing of the tablet. We have observed that the ablation process can create craters on the tablet surface, worsening the SrF yield. By moving the tablet up and down we distribute these craters over the whole surface, mitigating the yield loss and resulting in shot-to shot variations of about 20 %. We usually replace the tablet once per six months.

The ablation takes place in a supersonic expansion of Xe gas from a General Valve series 9 pulse valve which we modified by making the back plane adjustable to accommodate for changing spring constants at lower temperatures. The valve is enclosed in a copper housing that incorporates a channel for a coolant to flow through. The stagnation pressure is 3 bar and the valve is opened for 300 µs. We trigger the opening of the valve relative to the ablation pulse using a pulse-and-delay generator (Berkeley Nucleonics BNC 575). The valve is operated at a rate of 10 Hz and it can be cooled with cold nitrogen gas, resulting in an average molecular beam speed of 300 m/s. The nitrogen gas comes from a dewar containing liquid nitrogen and the temperature of the gas can be regulated by a heater element wound around the transport tube. In principle the readings from two thermocouples can be used for this regulation: one measures the temperature of the valve housing while the other one measures the temperature of the heater element. In practice, during the first measurements presented in this thesis, only the latter thermocouple value could be used as a proxy for the valve body temperature in the automatic feedback regulation system because the response time of the system was quite slow. Upon optimization of the source we expect to be able to reach a comparable output as a supersonic source for YbF molecules [86].

In order to contain the high pressure inside the source chamber, only the central part of the molecular beam with the lowest transverse velocity is let through a skimmer with a diameter of 2 mm, placed 60 mm downstream from the ab-

lation spot. The start of the decelerator is located 125 mm downstream from the ablation spot. The source chamber is pumped by two 71 l/s turbomolecular pumps (Pfeiffer HiPace 80) and each decelerator chamber by a 685 l/s turbopump (Pfeiffer HiPace 700). All the pumps share a fore-vacuum pump of 35 m^3/h (Edwards XDS35i). During operation the pressure in the source chamber rises from 2×10^{-8} mbar to at most 5×10^{-4} mbar while it remains below 2×10^{-7} mbar downstream in the decelerator.

4.2 Decelerator

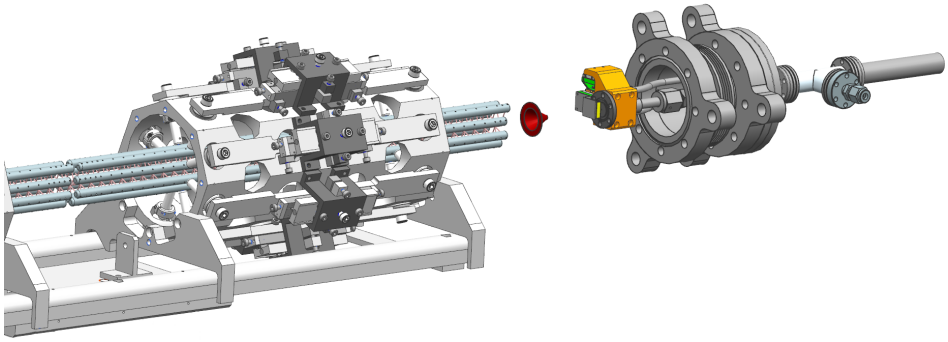

Figure 4.3: The molecular beam source and the first module of the decelerator. The position of the pulse valve can be adjusted through the bellows. A skimmer (red) separates the source chamber from the decelerator.

The dimensions of the ring-shaped electrodes and the method in which these are positioned relative to each other is based on the design of Meek et al. [12]. Since we require a rather long decelerator however, we will combine 10 modules of 50.4 cm each to form a horizontally oriented decelerator with a length of 5.04 m. This thesis covers the completion of 4 m of the decelerator and shows measurements taken with the declerator when it comprised 4 modules. Each module contains 336 ring-shaped electrodes made of tantalum wire of 0.6 mm diameter. The electrodes are mounted on eight 8 mm thick stainless steel rods which are placed in an octagonal pattern on the outside of a circle with circumference of 26 mm, as shown in Figures 4.4 and 4.5. Every rod is electrically isolated by two MACOR posts from the aluminum bars on which it is mounted. The bars are mounted on an aluminum octagon in an adjustable way to make precise alignment along five axes possible. The rings with an aperture of 4 mm

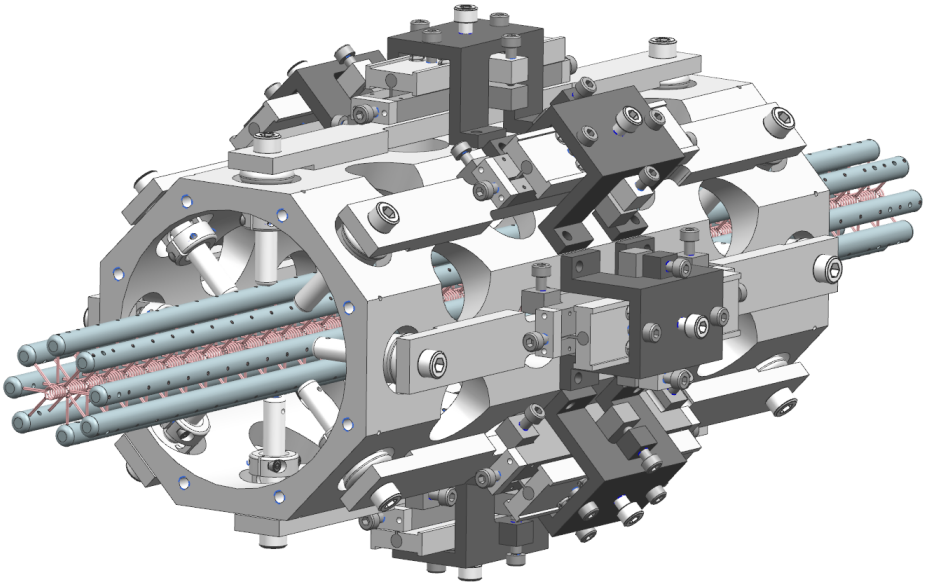

(a)

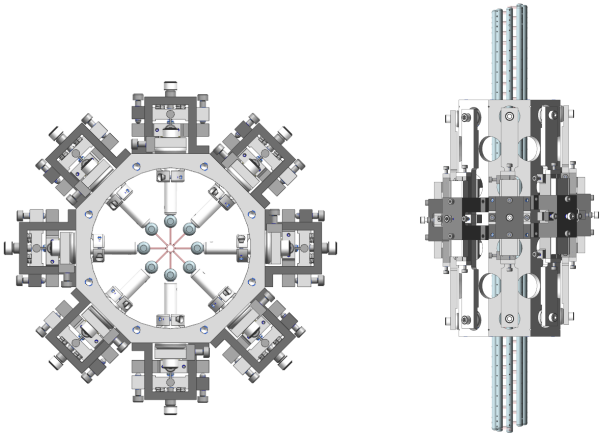

(b) (c)

Figure 4.4: Drawings of (a) 3D view, (b) front view, (c) top view of a module of the traveling-wave decelerator, showing the periodic ring structure and the alignment mechanisms. The stainless steel rods are mounted using electrically insulating MACOR posts onto aluminum bars, which can be positioned using the alignment mechanism.

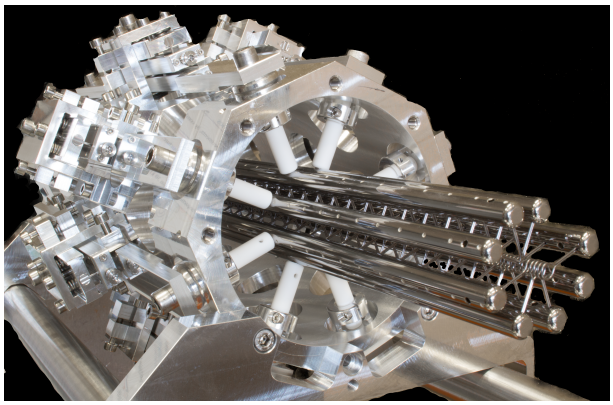

(a)

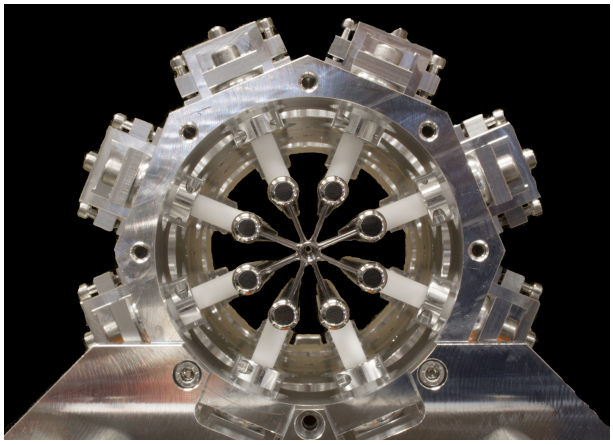

(b)

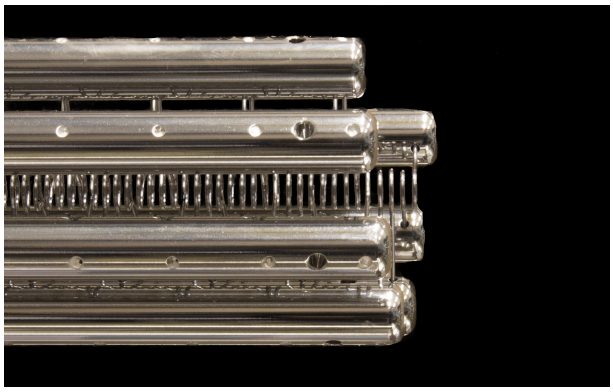

(c)

Figure 4.5: (a, b) Photos of one module of the traveling-wave decelerator, showing the periodic ring structure and the alignment mechanisms. The stainless steel rods are mounted via insulating MACOR posts onto aluminum bars, which can be precisely positioned using the alignment mechanism. (c) A close-up of the electrodes mounted on the stainless steel bars.

are mounted in a periodic manner such that every ninth ring is on the same rod. The gap between two consecutive rings is 0.9 mm, resulting in a periodicity of $L = 12$ mm. Two decelerator modules are placed in a 1 m long CF300 vacuum chamber on 80 cm long aluminum rails, which are mounted from the center on an alignment platform to ensure proper alignment of the two modules with respect to those in the next vacuum chamber. Rods of adjacent modules are electrically connected through copper plates. A stainless steel annulus is placed in between the two vacuum chambers for differential pumping.

4.2.1 Design parameters and accuracy

We have performed simulations to estimate the loss of molecules due to imperfect alignment of the decelerator [134]. In these simulations, the effects of varying the electrode radius, the distance between two electrodes, the horizontal angle between two modules, and the electrode center height were studied. We used the outcome of these simulations to determine the tolerances on the alignment for which at least 50 % of the molecules would be transmitted through the decelerator in the 9000 m/s^2 deceleration experiments. We thereby required that each of the individual defects would lead to a loss of at most 16 %. Based on these simulations we made the design drawings and listed the required accuracies. These target accuracies and the values we obtained in the real apparatus are listed in Table 4.1. Our target accuracies are based on our simulations and were determined before the paper by Meek et al. [12] was published. Their reported accuracies are better than our values listed in Table 4.1. However, our values in the last column of Table 4.1 should be regarded as an upper limit. The reason for this is that we have not measured all the electrodes separately but only ensured that their alignment is within the given tolerances. In general, the alignment error is well below the listed value. Further experiments and simulations should be performed to investigate whether the higher alignment precision of the decelerator by Meek et al. indeed leads to a better performance of the machine.

In order to achieve these accuracies we have constructed tools and established quality control procedures. For correctly bending the electrodes we first cut 1.52 m of 0.6 mm diameter tantalum wire and run an electrical current of 4 A at 4 V through it while it is positioned inside a vacuum chamber at a a few millibar residual gas pressure. After this annealing procedure we stretch the wire by hanging it from a beam and attaching a large weight at the bottom end. In this condition the wire is polished with very fine sandpaper to prevent electric sparking due to surface imperfections. The resulting wire of diameter 0.59 mm

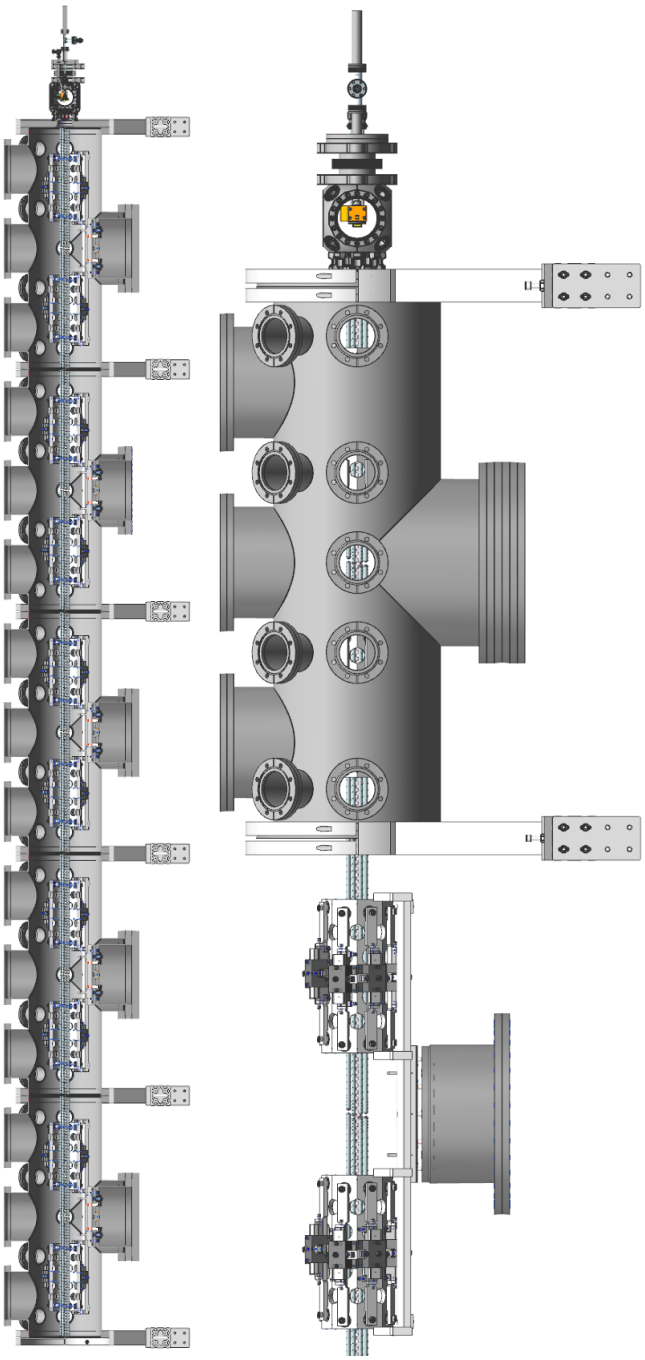

(a) (b)

Figure 4.6: Drawings of the full 5 m length decelerator (a) and a zoom-in on the first two meter and the source chamber (b).

(a) (b) (c)

Figure 4.7: (a) We use a brass bending tool to mechanically shape the electrodes. (b) The tool is operated by turning the upper disk. (c) The resulting electrode.

Table 4.1: A list of design parameters and accuracies achieved in the constructed decelerator.

Parameter	Design tolerance	Achieved accuracy
Electrode diameter	0.3 mm	$< +$ 0.2 mm
Electrode center height	0.2 mm	50 µm
Electrode perpendicular to rod	not specified	0.2 mrad
Electrode twist	not specified	2 mrad
Distance between two electrodes	160 µm	100 µm (typical 50 µm)
Angle between two modules	3 mrad	2.5 mrad

is then bent using a homemade brass bending tool shown in Figure 4.7a. Finally, the electrodes have the shape shown in Figure 4.7c. Although they are not perfectly circular individually, all together approximate a cylinder of 4.00 mm inner diameter when assembled in an octagon. We verified that the deformations do not constitute a problem by performing simulations of the electric field produced with realistically shaped electrodes in COMSOL [146].

The holes for holding the electrodes in the stainless steel rods were precisely drilled in a CNC milling machine. After machining, the rods were ground and polished in a trough vibrator from Walther Trowal. We secure the rod onto the aluminum bar via the MACOR isolation pieces such that a possible curvature is fixed from that point on. With the electrodes loose in the holes the rod is then put upside down in our homemade alignment tool which is depicted in Figure 4.8. In this way, the center of the electrode rings is determined solely by the flatness of the alignment tool even when the rod has a curvature. The flatness of the tool proved to be better than 50 µm. The comb structure of the tool ensures that the

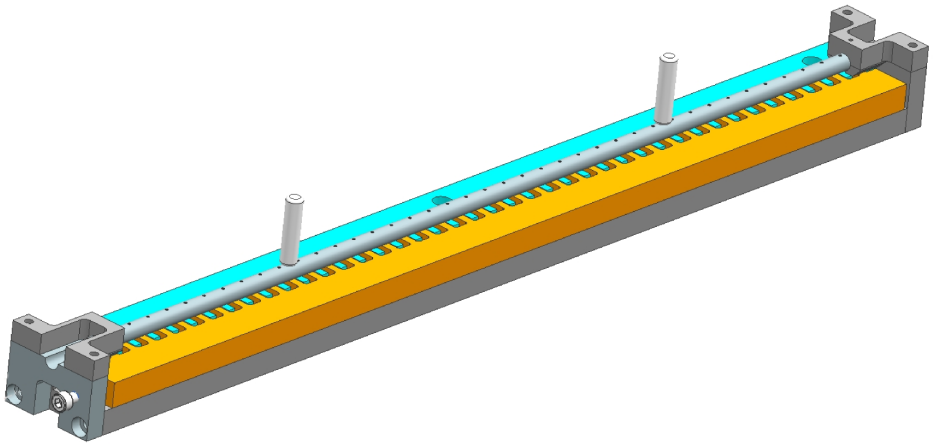

Figure 4.8: We have constructed an alignment tool to correctly align the electrodes on the rods. The comb structure makes the electrodes stand perpendicular to the rod at equal spacings. The top of the electrodes, and therefore the ring centers being on one line, are determined by the tool as well.

electrodes are aligned perpendicular to the rods and that they are straight. We then cut away the remaining electrode wire sticking out of the rods and fixed the electrodes with glue. For this we used Epotek epoxy H27D which is vacuum compatible after baking it in an oven at 150 °C for one hour. After baking, we measure and fine tune the electrode alignment using a microscope (Mitutoyo) with distance and angle scales. Fine tuning is done by manually bending the electrode into the correct position. We found that the mounted electrodes are quite stiff and can therefore be handled rather easily without the risk of damaging them or destroying the alignment. A small engineer's square is used to verify that the electrodes are not twisted within 2 mrad. For the electric field strengths that we will use, the possible small scratches that might result from this procedure have not caused any electrical discharge.

Aligning the electrode rods within the octagon was performed using optical precision telescopes, snugly fitting brass inserts, and a theodolite. The center of the octagon was found using crosshairs and used as the reference for the ring electrode centers. Our design enabled us to manipulate each rod along five axes: translation in the octagon radial and longitudinal directions, and rotation around the x, y, and z axes. Based on measurements that we performed [73] at the VU University in Amsterdam with our first module, which was not yet aligned ac-

cording to the standards described here, we concluded that the required accuracies are indeed needed for an optimally functioning decelerator. The first module has been realigned and showed better performance subsequently [72].

The alignment of the octagons inside the deceleration chamber was performed with crosshairs and telescopes as well [147]. Although the octagons are mounted on adjustable tables inside the vacuum chamber (see Figure 4.9), the requirements on the dimensions and parallelness of the end flanges were quite strict. Despite this, the tolerances on the squareness of the flanges with respect to the central axis were too large and we had to face a trapezoidal deformation of the first vacuum chamber that forced us to accept a mismatch of 1 mm between the center lines of the first set of two and the second set of two octagons. This effect affected the alignment of the decelerator modules in the third and fourth chambers too: since the range of the adjustable tables is limited we had to introduce an angle of 2.5 mrad between octagons II and III, ending up 2.5 mm to the side of the central axis.

4.2.2 High-voltage electronics

The traveling-wave decelerator works on the principle that oscillating high voltages produce moving potential wells in which the molecules are trapped. Deceleration is achieved by sweeping the frequency of the voltages down to lower values until standstill is reached for static voltages. The decelerator is basically a set of neighboring electrodes which are all capacitively coupled. A voltage supply that delivers the required voltages on the rings thus has to be able to drive a capacitive load at high voltage and at frequencies ranging from tens of kilohertz to DC. The first traveling-wave decelerator at the Fritz Haber Institute in Berlin [12] was not designed to bring molecules to standstill, and used transformers to produce the oscillating high voltages. However, transformers are not capable of producing DC voltages needed for fully stopping the molecular beam. We have therefore opted to use arbitrary waveform generators (Acquitek DA8150) in combination with fast DC-coupled high voltage amplifiers. In such a setup, the arbitrary waveform generators enable us to shape and control the trapping potentials as we like, giving us full control over the molecules. The design of the amplifiers was based on the requirements for the deceleration process, where the molecular properties of SrF and the geometry of the decelerator were leading. In general, the electric field magnitude should be at least reaching the turning points for the $(2, 0)$ and the $(1, 0)$ levels so that all the Stark energy could be used. Furthermore, the decelerator should be able to accept an incoming

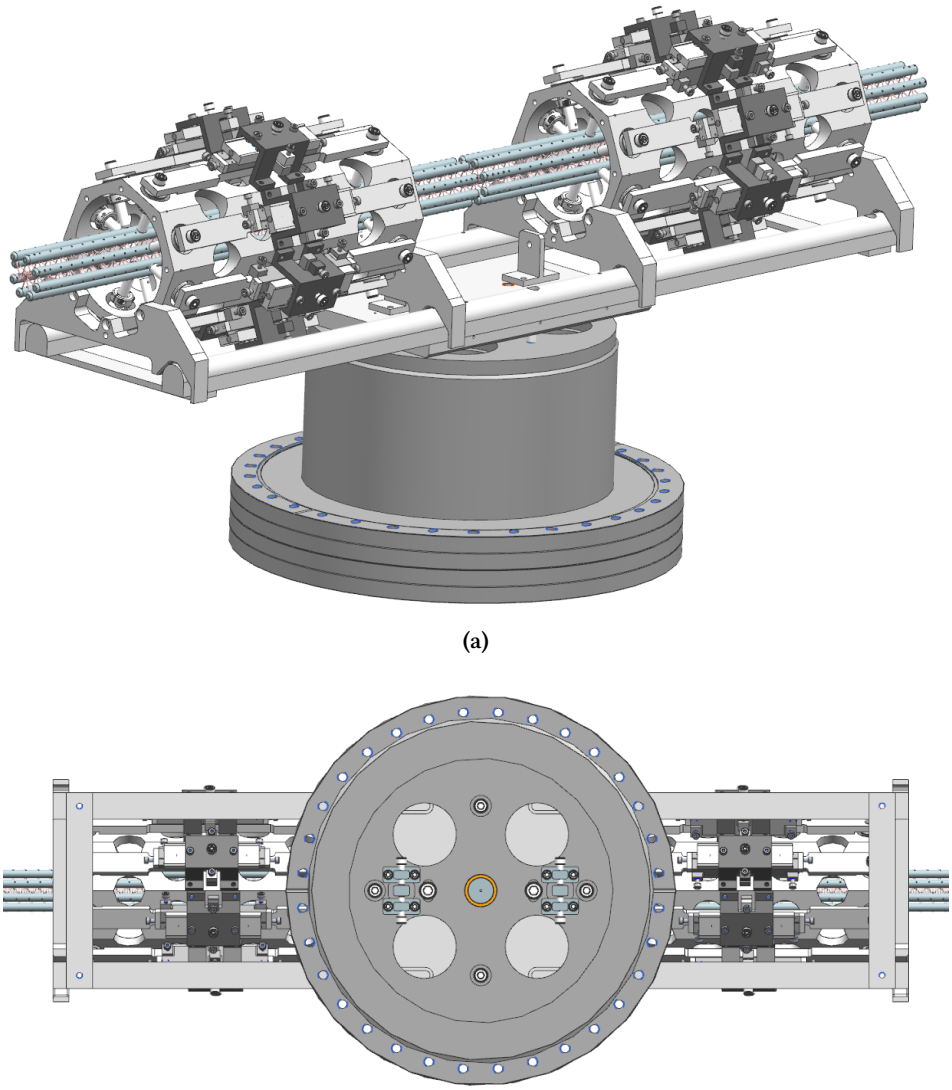

Figure 4.9: Two modules on a alignment platform (a) in 3D and (b) as seen from below. In (b) the adjustment bolts can be seen.

beam of 300 m/s, which can be achieved in a supersonic expansion in Xe from a cooled pulse valve. As the frequency is related to the periodicity $L = 12\,\text{mm}$ of

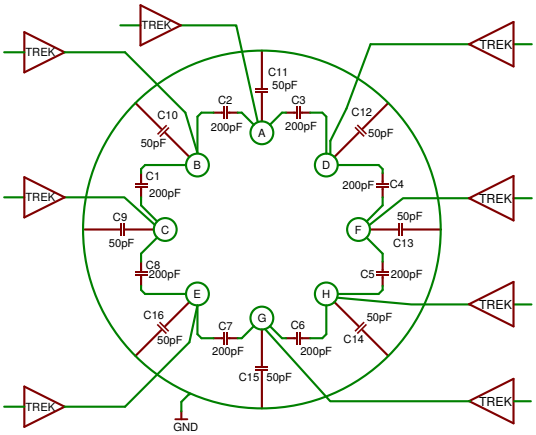

Figure 4.10: The electronic equivalent circuit of the decelerator. The values of the capacitances were measured for a 4 m long decelerator. The rods with the electrodes (labeled A through G) have each a capacitance of 50 pF to ground and 200 pF to each nearest neighbor. Each rod is connected to a Trek PD 10039 amplifier.

the electrodes via $f = v/L$, the frequency range should be from 25 kHz to DC. The amplifiers should be able to supply the voltages during a full deceleration sweep that lasts 30 ms, at a repetition rate of 10 Hz.

We measured the capacitance of the 4 m long decelerator and found that, within 10 % accuracy, each of the eight rods has a capacitance of 50 pF to ground and 200 pF to each of its nearest neighbors, as shown in Figure 4.10. To minimize capacitance from cables connecting the amplifiers to the decelerator, we use non-shielded cables and we put the amplifiers some 50 cm directly above the vacuum chamber. Based on these values, we required that the amplifiers can each handle a capacitive load of 400 pF. The only commercial offer for these requirements was from Trek Inc. from New York, USA. They succeeded in producing eight amplifiers (model PD10039) capable of delivering the required 30 ms deceleration waveform sweeping from 30 kHz to DC for 10 kV_{pp} sinusoidal voltages into a 400 pF capacitive load, followed by a 70 ms rest period. The specifications are given in Table 4.2. These amplifiers come with a dynamic adjust knob which needs to be tuned to the attached load, to prevent overshoot and oscillations. However, during operation, the current I that each individual amplifier has to supply, is not equal to $I = 2\pi f C U$ with f the frequency, C the capacitance of 400 pF and U the voltage. Instead, all the eight currents are phase-shifted by $2\pi/8$

Table 4.2: Specifications of the Trek model PD10039 high voltage amplifiers, according to the Operator's manual. All specifications are with a 400 pF load.

Parameter	Specification
Output voltage range	0 to ±5 kV DC or peak AC
Output current range	0 to ±500 mA DC or peak AC
DC Voltage gain	1000 V/V
DC Voltage gain accuracy	Better than 0.1 % of full scale
Output offset voltage	Less than ±2 V
Output noise	Less than 1.0 V_{rms}
Slew rate	Greater than 1000 V/µs
Drift with time	Less than 50 ppm/hr, noncumulative
Drift with temperature	Less than 200 ppm/°C
Settling time	Less than 50 µs for a 0 to 5 kV step

and therefore the currents need to be considered together with their phase. In our configuration with eight amplifiers and $2\pi/8$ phase-shift, it turns out that the current that the individual amplifiers have to deliver is much less. The amplifiers come with monitor outputs for the supplied voltage and current. We recorded these values and found that, for a four meter long decelerator, the equivalent load per amplifier was 188 pF. Unfortunately, the maximal amplitude of 5 kV limits the acceptance of our decelerator considerably, as calculated in Chapter 3. In particular, deceleration of SrF in the $(2, 0)$ state is not more advantageous than the $(1, 0)$ state as it is for YbF [148], because the electric field strength that we can reach with these amplifiers is not high enough.

4.3 Detection system

SrF molecules are best detected using laser induced fluorescence, since the wavelengths are in the visible part of the spectrum and laser diodes are easily available. Using lasers, it is also easy to do state-selective detection so that we can measure which states are decelerated and which are not. Furthermore, we aim for a very cold sample of SrF and are going to use laser cooling as one of the techniques to reach this goal. Hence, our group built the laser setup to perform these tasks and we will describe it briefly in this section. For a more detailed description, the intricacies of the SrF level structure and its implications for laser cooling, the

reader is referred to the thesis of Meinema [111].

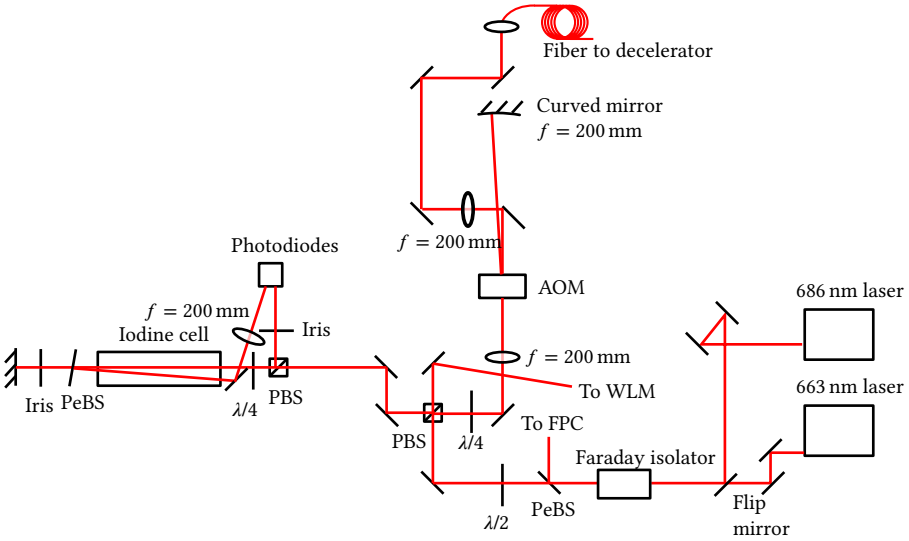

Figure 4.11: The laser setup with the iodine cell. PeBS means pellicle beam splitter, PBS polarizing beam splitter, FPC Fabry Perot cavity, AOM acousto optical modulator, and WLM wavelength meter. $\lambda/2$ and $\lambda/4$ are half- and quarter-waveplates.

For the detection of SrF we have made the setup shown in Figure 4.11 with two lasers and a heated iodine cell for absolute frequency locking. The rovibrational energy levels of SrF are shown in Figure 4.12. We have built extended cavity diode lasers (ECDL) for 663 nm (Opnext HL6545MG) and 686 nm (Opnext HL6750MG), to address the $A\,^2\Pi_{1/2} \leftarrow X\,^2\Sigma^+$ $(0,0)$ and $(0,1)$ vibrational branches. These branches are needed for laser cooling and were used here for optical detection. The output of the diodes is typically 60 mW and the light goes through a Faraday isolator and is then split into different paths. A part of the light goes via a multimode fiber to a HighFinesse Ångstrom WS/6 VIS wavelength meter. Approximately 10 mW of laser light is used to lock the laser to absorption line R(115) (6-6) a9 in molecular iodine enclosed in a quartz cell heated to 300 °C. We identify this line using frequency-modulated doppler-free saturated-absorption spectroscopy. The frequency of the laser light is modulated by the laser diode injection current and is shifted by passing through an AOM in order to bridge the frequency difference between the iodine lines and the transitions in SrF. A feedback system is implemented to enable locking of the laser frequency to a

zero crossing of a derivative of an iodine absorption line.

The ^{88}SrF molecule has hyperfine structure due to the nuclear spin $I = 1/2$ of the F atom. The basis states are best described in a $|N, S, J, I, F, M_F\rangle$ manner in which $\boldsymbol{J} = \boldsymbol{N} + \boldsymbol{S}$, and $\boldsymbol{F} = \boldsymbol{I} + \boldsymbol{J}$. If we want to detect all molecules in the $N = 1$ state, this means that the laser needs to address the four hyperfine states with $F = 0, 1$ ($J = 1/2$) and $F = 1, 2$ ($J = 3/2$). For ^{88}SrF the hyperfine energy splitting between those four levels is almost equal. As described by Shuman et al. [107] an EOM can be used to generate frequency sidebands on the laser light, so that light from one laser can be made to have reasonable spectral overlap with the four levels at the same time. We implemented this by letting the laser light pass through an EOM which modulates the light at a frequency of 41 MHz at a modulation depth of 2.6, such that almost all the power is in the first and second order sidebands with almost equal amplitudes. The laser light is subsequently coupled into a single mode optical fiber and transported to the decelerator, where we have between 5 mW–10 mW of light in the laser beam with a diameter of 3 mm. The laser light is directed through the detection region in the vacuum chamber using two mirrors as shown in Figure 4.13. The beam is retro-reflected such that it crosses the molecular beam at right angles twice. The fluorescent light is collected using two 25.4 mm diameter plano-convex lenses with a back focal length of 17.7 mm placed such that their focal point overlaps with the molecular beam axis. One of the lenses directs the light on a mirror, which reflects it back to double the amount of detected light. The collected light is sent as a parallel beam out of the vacuum chamber, where it is passed through a bandpass interference filter. We have used two filters: one (Semrock FF01-661/20, 20 nm around 661 nm) to observe 663 nm, and one (Semrock FF01-684/25, 25 nm around 684 nm) to detect 686 nm light from the $A\,^2\Pi_{1/2} \rightarrow X\,^2\Sigma^+(0,1)$ transition, which is free of background from the 663 nm excitation laser beam. After passing the filter, a lens focuses the scattered light through an adjustable iris and onto the cathode of a photomultiplier tube (PMT) from Hamamatsu (H7422P-40). The overall detection efficiency is estimated to be $\sim$2 %. The arrival time of the PMT pulses is recorded by a multi-channel analyzer (Fastcomtec MCA3).

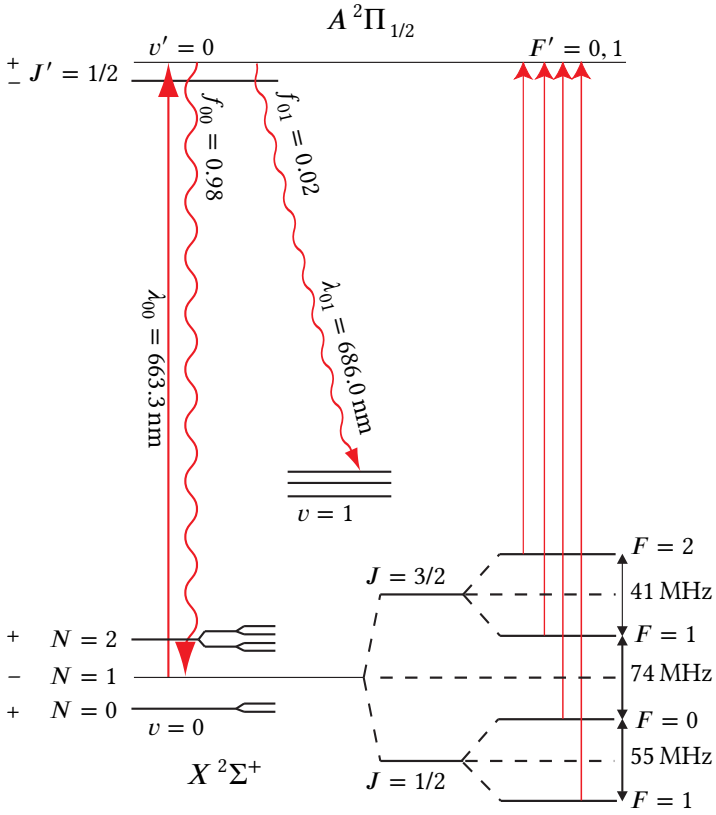

Figure 4.12: The relevant transitions in ^{88}SrF. We use a laser at a wavelength of 663 nm to excite molecules in the $N = 1$ level of the $X\,^2\Sigma^+$ vibrational ground state to the $J' = 1/2$, $v' = 0$ rovibrational ground state of the electronically excited $A\,^2\Pi_{1/2}$ state. Frequency sidebands on this laser light address all four hyperfine levels. The hyperfine splitting in the $A\,^2\Pi_{1/2}$ state of less than 3 MHz [149] is not resolved. Fluorescence detection is either done background free on the 686 nm $v' = 0 \rightarrow v = 1$ transition or on the 663 nm line. The branching ratio (Franck-Condon factor) for the spontaneous decay to the $v = 1$ level is 0.02.

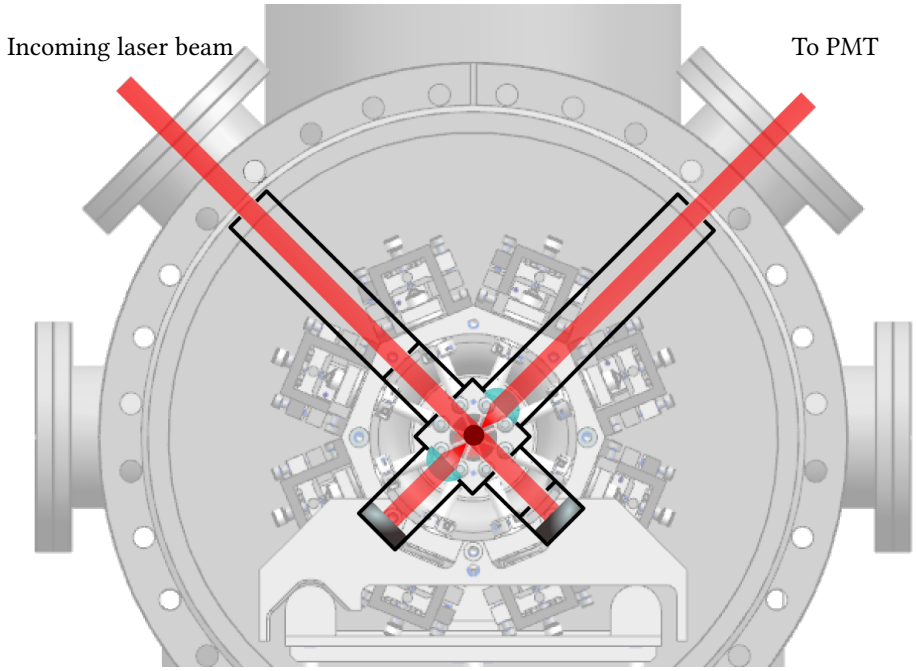

Figure 4.13: Schematic view of the detection setup. The laser beam is crossed with the molecular beam and is then back reflected off a mirror. Two lenses with a focal point at the molecular beam axis collect the light from the molecules and send it as a parallel beam towards the interference filter, a focusing lens, an aperture and the PMT outside the vacuum chamber.

5 | Experimental results

In this chapter we show and discuss experimental results that have been obtained with the setup described in Chapter 4. First we present a characterization of the molecular beam originating from our source. In the second part of this chapter we describe the first time deceleration of SrF molecules using a two meter long decelerator.

5.1 Molecular beam source

5.1.1 Rotational state population in the molecular beam under the influence of electric fields

We have measured the population in the lowest rotational quantum states of SrF molecules, seeded in an argon beam. This was done as function of the applied voltage using one decelerator module of 50 cm in DC-guiding mode, employing static voltages with alternating polarity on the rings. In DC-guiding mode, the molecules are not captured in three dimensional potential wells. Instead the low-field seeking molecules are focused onto the axis of the decelerator without any longitudinal confinement. This configuration prevents transverse spreading of the beam and therefore leads to more molecules arriving at the detection zone, as opposed to having no DC voltages applied. Since we start with a finite rotational temperature, the molecules originating from the source chamber are known to be distributed over a number of rotational states. Because each rotational state has its own Stark curve, the fraction of molecules that is successfully transported through the decelerator structure is state dependent. There has been interest in the literature concerning the purity of the quantum states in such decelerator experiments [150], especially for cold collision experiments. For our deceleration experiments, it is important as well to have most of the molecules in the $N = 1$

rotational state, which has the best suited Stark shift for our combination of high voltage amplifiers and decelerator structure.

Experimental setup

We have probed the rotational state population of the $X\,^2\Sigma^+$ electronic ground state by illuminating the molecular beam with light from a dye laser and measuring the laser induced fluorescence from the $A\,^2\Pi_{1/2} \leftarrow X\,^2\Sigma^+$ $(0,0)$ and $(0,1)$ transitions, 11.7 cm downstream from the exit of the decelerator module. We used a Coherent 699 single mode ring dye laser, pumped by a Coherent Verdi DPSS laser operating at 3 W. The dye laser was operated with DCM dye and had a linewidth of 1 MHz. The laser frequency could be scanned continuously over a range of $1\,\mathrm{cm}^{-1}$ and the output power was around 100 mW. The light from the dye laser was transported from the laser laboratory to the molecules setup through a single mode optical fiber of 25 m length. Before entering the decelerator chamber, the light was attenuated in power by a neutral density filter such that only 270 µW was used for the experiment in order to prevent power broadening of the observed transitions. In this way we could observe the hyperfine structure of the $X\,^2\Sigma^+$ ground state as well. We calibrated a frequency scan voltage output of the laser electronic control unit to a simultaneous measurement of the laser light wavelength with a HighFinesse Ångstrom WS/6 VIS wavelength meter for use as the frequency calibration for our measurement.

Results and discussion

Figure 5.1 displays the measured rotational spectrum of SrF after passing through 50 cm of the decelerator. The lowest trace is a measurement with the electrodes connected to ground and the upper trace was taken with a static voltage of ±2 kV alternating on subsequent rings. Each trace is the result of a single frequency scan and took 9 minutes to complete. In the wavenumber range between $15\,074.8\,\mathrm{cm}^{-1}$ to $15\,075.8\,\mathrm{cm}^{-1}$ we have recorded 24 lines, identified as the hyperfine-split P and Q branches originating from the $N = 1 \ldots 6$ levels in the $v = 0$ vibrational ground state. Similar spectra for the $A\,^2\Pi_{1/2} \leftarrow X\,^2\Sigma^+$ $(0,1)$ transition from the first vibrational level in the electronic ground state were obtained by scanning the wavenumber of the laser light between $14\,577.65\,\mathrm{cm}^{-1}$ to $14\,578.23\,\mathrm{cm}^{-1}$. We find that the population in the $v = 0$ and $v = 1$ states are similar in number. We estimate the rotational temperature during these measurements to be 8 K to 12 K by comparing the $(0,0)$ spectrum at 0 kV to simulations in

PGOPHER [119]. It is expected that the rotational temperature can be lowered by tuning the valve parameters (e.g. opening time, stagnation pressure) as reported by other groups such as in [86, 151], in order to increase the population in the $N = 1$ level. From the Boltzmann distribution of the rotational states we have calculated that a rotational temperature of 3.5 K, as it was reported for the YbF source [86], would improve the $N = 1$ population by a factor of three. Further cooling to 1.5 K, as reported in the same experiment [86] for an Yb/AlF_3 metal target, would improve the number of SrF molecules by a factor four.

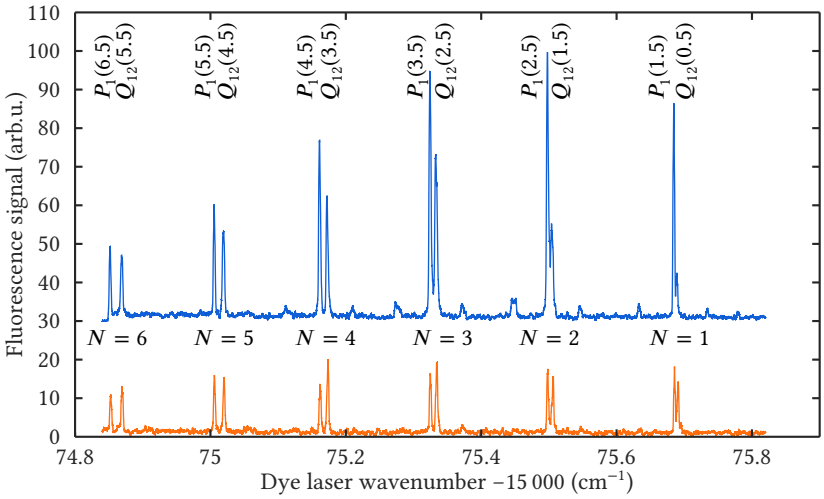

Figure 5.1: A rotational spectrum of the $A\,^2\Pi_{1/2} \leftarrow X\,^2\Sigma^+(0,0)$ transition showing the $P_1(N + 1/2)$ and $Q_{12}(N - 1/2)$ lines for $N = 1 \ldots 6$ from right to left. For deceleration we use the $N = 1$ population. The spectrum has been obtained from a molecular beam that had passed one decelerator module operated at static voltages of 0 kV (lower trace) and ±2.0 kV (upper trace, vertically offset by 30). For details, see text.

The effect of exposing the molecules to electric fields is visible from the upper trace of Figure 5.1. The configuration with static voltages alternating in polarity on subsequent electrodes creates an electric field minimum along the axis of the decelerator. Molecules in low-field seeking states are hence focused onto the molecular beam axis and are expected to arrive at the laser detection region in larger numbers, compared to the experiment without voltages applied. High-field seeking states, on the contrary, can be defocused out of the decelerator leading to a smaller fluorescence signal. Because the turning point of the Stark

curves is shifted towards higher electric field strengths for the higher rotational levels, the enhancement is most pronounced for the lowest rotational levels given the voltages used here. We also see that the P-lines in the measured spectrum are more enhanced than the Q branches. To understand this we need to take the magnetic quantum numbers of the hyperfine levels into account. Because the Stark effect couples states that have the same magnetic quantum number and one quantum difference in the rotational quantum number, it turns out that most of the states that take part in the Q-branch of the measured spectrum are high-field seekers while more states that are part of the P-branch are low-field seekers. This spectrum therefore demonstrates that the decelerator is quantum state selective in its operation. For our purposes we would like to have as much population in the $N = 1$ level as possible. To mitigate the loss in the decelerator due to the high-field seeking character of the $J = 1/2$ levels, one could transfer the $J = 1/2$ population to the $J = 3/2$ levels before entering the decelerator. This should be possible by optically pumping on the Q-branch or by using microwave radiation to make the transition.

5.1.2 Beam characteristics in DC-guiding measurement

The velocity of the supersonically expanding carrier gas is given by a distribution rather than a unique velocity. Furthermore, the valve opens only for about 300 µs. To get maximum density of ablated molecules in the decelerator, the ablation should take place when the most dense part of the gas pulse passes the ablation spot. The small plume of ablated molecules will only sample a fraction of the carrier gas velocity distribution. We have measured the velocity distribution for SrF seeded in beams of Ar en Xe as shown in Figure 5.2.

In this measurement, we created the molecular beam from a room temperature valve and focused it along the 2 m long decelerator axis by applying static voltages of 1.5 kV and alternating polarity on subsequent ring electrodes. Both measurements used a stagnation pressure of 3.8 bar and had an average source chamber pressure of 2×10^{-4} mbar at 10 Hz valve pulsing rate. Detection of the molecules in the $X\,^2\Sigma^+ (v = 0, N = 1)$ state took place after passing through the decelerator, as described in Section 4.3. As we measured the flux of molecules, we can express the beam velocity distribution as

$$f(v)\,\mathrm{d}v = C v^3 \exp\left[-\frac{M(v - v_0)^2}{2k_\mathrm{B}T}\right]\mathrm{d}v, \tag{5.1}$$

where C is a normalization constant and T is the longitudinal temperature. The

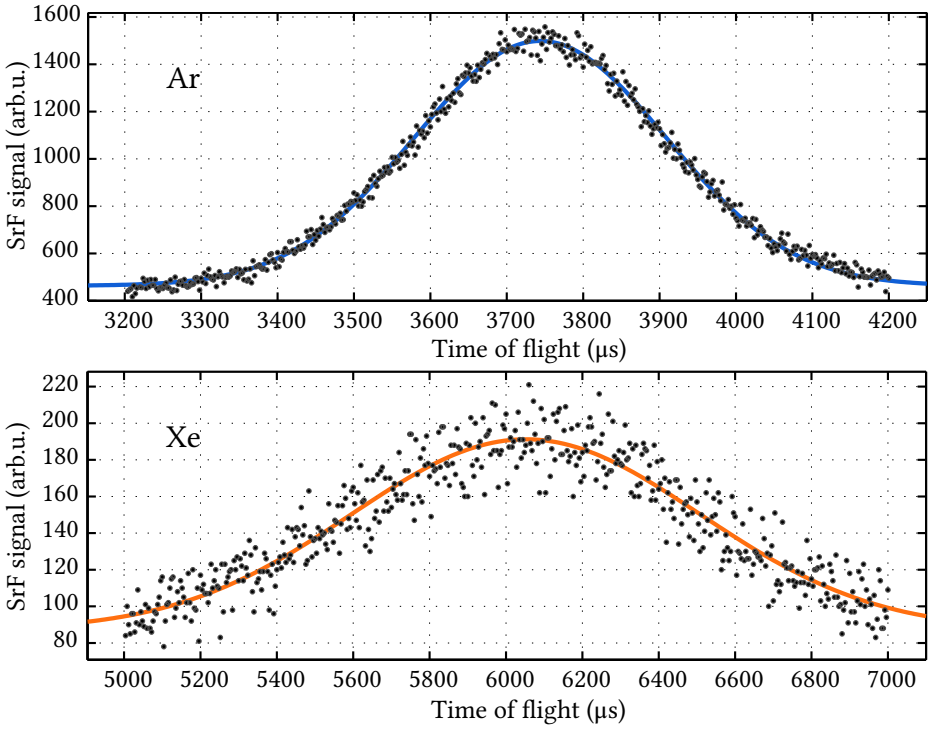

Figure 5.2: Time-of-flight measurements of DC-guided SrF molecular beams seeded in Ar and Xe. The distance traveled was 2.2415 m. Measurements are indicated by black dots. A Gaussian distribution is fitted to the data points to determine the beam velocity, which is found to be 599 m/s for Ar and 370 m/s for Xe.

velocity spread is given by $\sigma_v = \sqrt{k_B T/M}$. Converting this to a time-of-flight distribution with $t = L/v$ and $t_0 = L/v_0$, we get

$$g(t) = \frac{CL^4}{t^5} \exp\left[-\frac{ML^2}{2k_B T}\left(\frac{t-t_0}{tt_0}\right)^2\right], \tag{5.2}$$

where we assume that the molecules start from a very short pulse. When the pulse has not spread out too much, so that $t \approx t_0$, the TOF-distribution takes the Gaussian shape with variance $\sigma^2 = k_B T t_0^4/ML^2$:

$$g(t) \approx \frac{CL^4}{t_0^5} \exp\left[-\frac{ML^2}{2k_B T}\frac{1}{t_0^4}\left(t-t_0\right)^2\right]. \tag{5.3}$$

We fitted the Gaussian distribution of Equation (5.3) to the data and found, for a length $L = 2241.5$ mm the times t_0 and the full width at half maximum FWHM =

$2\sqrt{2\ln 2}\sigma$ to be $t_0 = 3744\,\mu s$ and FWHM $= 384\,\mu s$ for Ar, and $t_0 = 6052\,\mu s$ and FWHM $= 1095\,\mu s$ for Xe. Although we have occasionally measured the carrier gas beam directly, using hearing aid microphones [152], here we did not. However we assume that we can use the SrF arrival times to get accurate values for the Ar and Xe beams, since the velocity slip is reported to be of order 5 %–10 % [86]. Then, the analysis yields translational temperatures of 3 K and 13 K, respectively. From this, we obtain beam velocity distributions with mean velocities of 599 m/s for Ar and 370 m/s for Xe, with FWHM = 61 m/s for Ar and FWHM = 67 m/s for Xe. Although both SrF beams were not fully optimized, it can be concluded that the Xe beam is significantly hotter than the Ar beam, and this might be the reason why the SrF(1, 0) signal is significantly less in the Xe beam. Furthermore, the translational temperature of 3 K for the argon beam is significantly lower than the rotational temperature of 10 K that we measured in the rotational spectroscopy experiment months earlier. The conditions in these two experiments were presumably not equal, making it difficult to compare the two temperatures. However, the fact that the SrF signal in Ar is much stronger here than in Xe, together with the report by Tarbutt et al. [86] that they always find the same value for the translational and rotational temperatures, hints in the direction that the rotational temperature in our rotational spectroscopy measurement could have been lower if it were properly optimized.

5.2 AC-guiding and deceleration experiments[1]

Figure 5.3 shows a schematic view of our deceleration experiment consisting of a supersonic expansion source, the decelerator and a laser-induced fluorescence detection zone. A 100 mJ pulse from a Nd:YAG laser at its principal wavelength is used to ablate SrF radicals from a home-pressed tablet consisting of 90 % SrF_2 and 10 % B into a supersonic expansion of Xe gas from a pulsed General Valve. The valve is operated at 10 Hz and it can be cooled with cold nitrogen gas to −30 °C. The molecular beam enters the decelerator located 125 mm downstream of the valve through a skimmer with a diameter of 2 mm, placed 60 mm from the ablation spot.

The dimensions of the ring-shaped electrodes and the method in which these

[1] Parts of this section are published as J. E. van den Berg, S. C. Mathavan, C. Meinema, J. Nauta, T. H. Nijbroek, K. Jungmann, H. L. Bethlem, and S. Hoekstra, *Traveling-wave deceleration of SrF molecules*, J. Mol. Spectrosc. **300**, Spectroscopic Tests of Fundamental Physics, 22–25 (2014) doi: 10.1016/j.jms.2014.02.004.

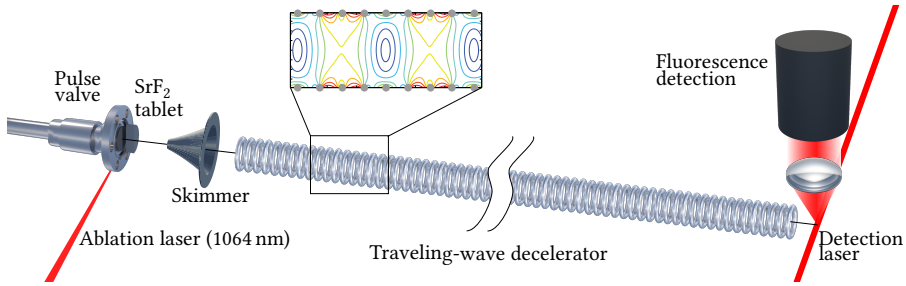

Figure 5.3: A schematic view of the experiment. SrF molecules are created by laser ablation from a tablet. A pulsed supersonic Xe expansion cools the SrF molecules and takes them to the ring structure where the molecules are guided or decelerated. Further downstream the SrF is detected by laser induced fluorescence.

are positioned relative to each other are described in Section 4.2. We combine four decelerator modules of 50.4 cm in order to form a horizontally oriented decelerator with a length of 2.016 m.

Arbitrary waveforms are generated using DACQ8150 Acquitek PCI cards and amplified by eight custom-made high-voltage amplifiers from Trek Inc. These amplifiers were operated at their maximal output voltage of ±5 kV with sinusoidal waveforms having frequencies between 30 kHz and 19.4 kHz for beam velocities between 367 m/s and 230 m/s. The arbitrary waveforms can be used to tailor the shape of the potential at will or to manipulate the trap as we like [74]. We used this functionality to abruptly go from deceleration to acceleration of a molecular beam.

5.2.1 Detection

After deceleration and 116.5 mm of free flight, the molecules are state-selectively detected using a resonant laser-induced fluorescence scheme. Light at 663.3 nm to drive the $A^2\Pi_{1/2}(v = 0) \leftarrow X^2\Sigma^+(v = 0)$ $P(1/2), Q(1/2)$ transitions, which probes the population in the lowest low-field seeking $N = 1$ rotational level, is generated with the setup described in Section 4.3. It is this state which is the starting point for a parity violation measurement, and the state for which laser cooling has been demonstrated to work. The $N = 1$ state is also the best choice for deceleration given the electric field strength available to us. The light used for SrF detection is sent through an EOM driven at 41 MHz for the creation of sidebands that overlap with the resolved hyperfine levels in the SrF

$X^2\Sigma^+(v = 0, N = 1)$ state [107]. It reaches the detection chamber through a single mode optical fiber where it is directed through the detection region using two mirrors. The beam is retro-reflected such that it crosses the molecular beam at right angles twice. Typically, the laser power is 2 mW and the beam diameter is 3 mm. A system of lenses focuses the fluorescent light through an interference filter onto the cathode of a photomultiplier tube (PMT). We have an overall detection efficiency of 2 %. The arrival time of the PMT pulses is recorded by a multi-channel analyzer with 1 µs bins. The time-of-flight spectra are started with the ablation pulse.

5.2.2 Results

In this section we present the results obtained from AC-guiding, decelerating, and accelerating SrF(1, 0) molecules with the traveling-wave decelerator. We show the measured time-of-flight (TOF) spectra next to simulations, as well as some simulated phase space diagrams. The TOF profiles show very distinct fea-

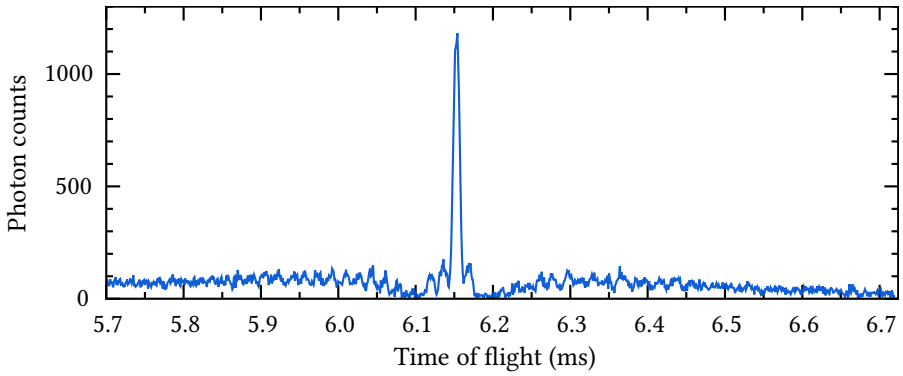

Figure 5.4: Measured time-of-flight profile for SrF(1, 0) molecules originating from a room temperature valve using Xe, after 2 m of AC-guiding at a speed of 367 m/s.

tures which are best seen in the guiding measurement shown in Figure 5.4, where we used xenon gas from a room temperature valve. The basis for the spectrum is a Gaussian distribution due to the velocity spread of the beam, as shown in Figure 5.2. In addition to the Gaussian background there is a sharp peak at 6.15 ms that corresponds to molecules that are trapped in a moving electric trap. This is illustrated in Figure 5.5 where we show the simulated phase space occupation of the guided molecules at 367 m/s. The small maxima next to the main peak

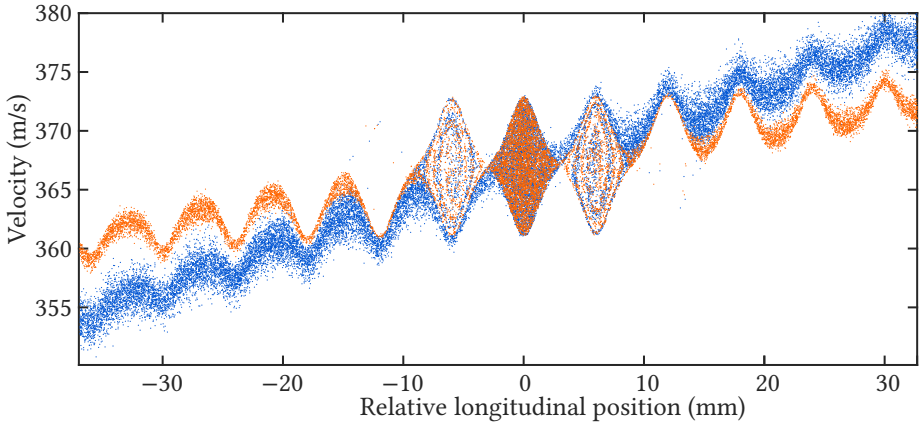

Figure 5.5: Simulated phase space occupation of the molecules for a guided beam of 367 m/s after flight times of 2.9 ms (blue) and 5.8 ms (orange). The initial packet size is such that apart from the central potential well located at the origin of the coordinate system, also the adjacent wells are partly filled with SrF molecules. The molecules that are not trapped undergo a rotation in phase space and are bunched because of the shape of the electric field.

are due to molecules that were trapped in potential wells adjacent to the central well. Depending on the size of the SrF cloud at the entrance of the decelerator only one or a few potential wells are loaded with SrF molecules. The size of our ablation spot of about 1 mm causes the vast majority of the trapped molecules to end up in only one trap, as long as the high-voltage switch-on time is properly synchronized with the molecular packet. If this switching-on occurs when the molecular packet is just in between two potential wells, both will be filled with a part of the molecules. The molecules that are collected in these wells leave behind a dimple in the final TOF spectrum which is broadened because of flight time. The molecules that fall outside the longitudinal phase-space acceptance of the trap but remain inside the transverse phase-space acceptance of the decelerator are not captured in the potential well, but are still guided through and detected. These molecules end up in the broad wings that are observable in the guiding signal. The modulation that is visible on these broad wings is caused by bunching in phase space on the moving potential hills in between the electric field minima, as can be seen from the phase space plot in Figure 5.5.

The left sides of Figures 5.6 and 5.7 show measured time-of-flight (TOF) spectra of SrF(1, 0) molecules. Figure 5.6 shows the first deceleration results of SrF in a traveling-wave decelerator, obtained with the pulsed valve at room tempera-

ture giving an initial beam velocity of 367 m/s. Later measurements with a valve cooled to −25 °C started with a speed of 300 m/s and are shown in Figure 5.7. For each spectrum a small constant background due to stray light has been subtracted. The spectra have been given a vertical offset for clarity. Each spectrum shown is the sum of 10 240 ablation shots, except for the strongest deceleration of the 300 m/s beam which is the average of twice as many shots because of frequent unlocking of the spectroscopy laser. In the 300 m/s guiding experiment we detected 5 photons per shot from molecules trapped in the central well. We estimated the detection efficiency to be 2 %, therefore we guided 2.5×10^2 molecules per shot, indicative of a rather low beam density. Being cautious not to damage the ablation tablet, we have used the lowest possible laser beam power for ablation that enabled us to measure still with a good signal-to-background ratio. Obtaining the time-of-flight traces took about 17 minutes per trace. The mean speeds of the beams were 367 m/s and 300 m/s and the starting speeds for the decelerator waveforms were set accordingly by using frequencies of 30.6 kHz and 25 kHz. The arrival time of the molecules is plotted for guiding at constant speed

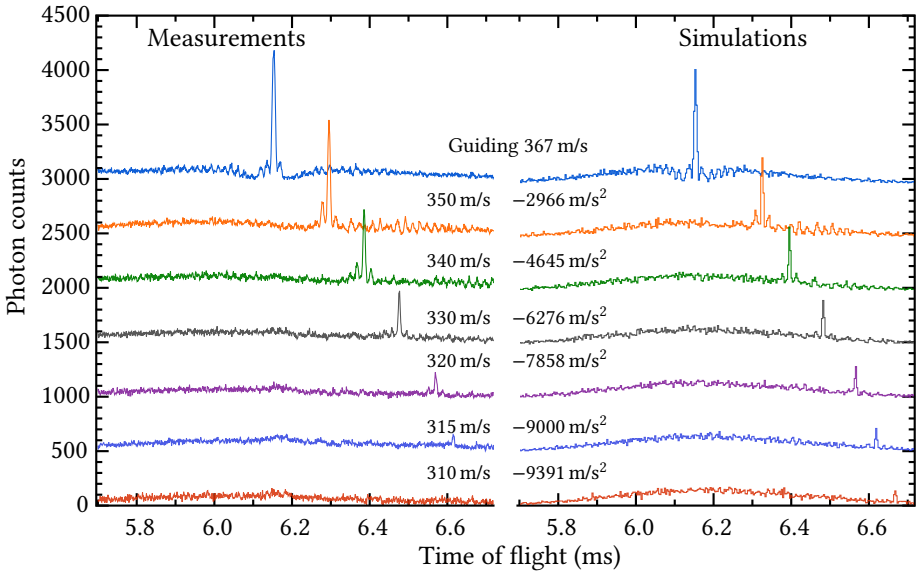

Figure 5.6: Measured (left) and simulated (right) time-of-flight profiles for SrF(1, 0) molecules after 2 m of deceleration, starting at 367 m/s. The labels indicate the final velocity and the deceleration strength. A vertical offset was added for clarity.

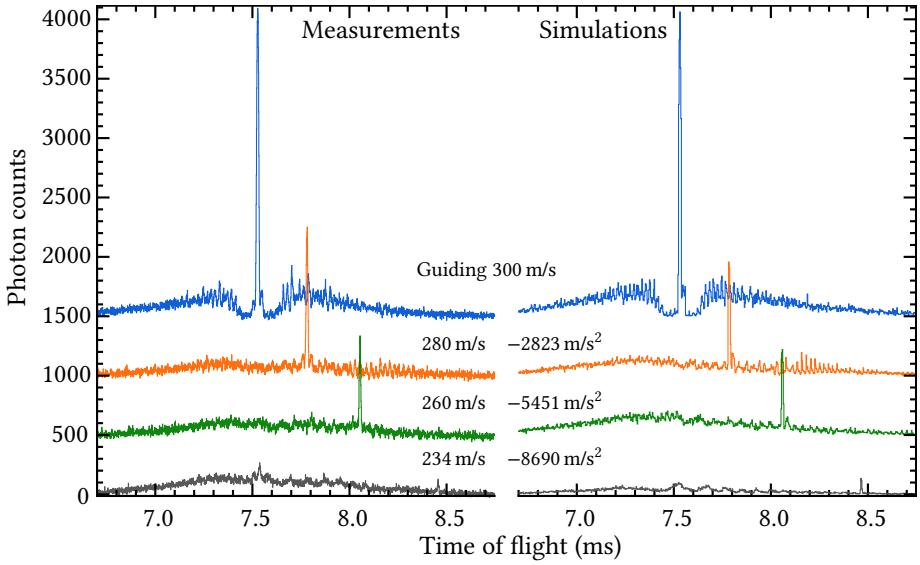

Figure 5.7: Measured (left) and simulated (right) time-of-flight profiles for SrF(1, 0) molecules after 2 m of deceleration, starting at 300 m/s. The labels indicate the final velocity and the deceleration strength. A vertical offset was added for clarity.

and a range of deceleration strengths, each of which was constant throughout the full 2 m length of the decelerator. The delayed arrival of the main package of molecules with increasing deceleration strength is clearly visible. In the cold valve experiment at the highest deceleration of 8.7 km/s^2 the package of decelerated molecules is arriving around 8.45 ms, corresponding to molecules that were decelerated from 300 m/s to 234 m/s. This corresponds to a removal of almost 40 % of the kinetic energy.

In Chapter 3 we have calculated the phase space acceptance of the decelerator for different deceleration strengths as shown in Figure 3.6. As an addition to this we have now simulated the TOF spectra as well, including the effects of the shape of the initial distribution. All the simulations are based on the work described in Chapter 3 and take into account the free flight from the ablation point to the decelerator entrance, the traversing of the fields inside the decelerator, the free flight to the detection zone and the size of the laser beams used for detecting the molecules. Further optical parameters such as laser power or frequency were not included, all molecules were set to be in the low-field-seeking part of the $N = 1$

rotational state and assumed to be detected by the laser.

By comparing the simulations to the measurements, we derive the properties of the molecular beam after the supersonic expansion. For the measurements with the 300 m/s beams from the cold valve we find a longitudinal velocity distribution with a mean speed of 300 m/s and a standard deviation of 20 m/s. Furthermore the simulations match best with a starting size of the molecular packet of order 1 mm, which matches to the spot size of the ablation laser on the tablet. This spot size is much smaller than the 9.7 mm that was used in the YbF(2, 0) deceleration experiments [148] at 10 kV amplitude waveforms. For this reason our TOF-spectra show most of the molecules in one peak, whereas for YbF they were distributed over three potential wells. For the rest the results are very similar.

As displayed on the right sides of Figures 5.6 and 5.7 all the features of the measurements are reproduced in the simulations. The smaller peaks for higher deceleration strengths can be understood from the decreasing phase space acceptance only. On that basis we conclude that other loss mechanisms, such as collisions with background gas or nonadiabatic spin-flips [154, 155] to high-field seeking states can indeed be neglected [12].

Applying a very strong deceleration of 9.7 km/s^2 as was tried in the deceleration of a beam from 367 m/s to 310 m/s reduces the phase space acceptance too much for molecules to come through, although the simulations still show a peak. In that regime, we are clearly at the edge of the decelerator's capabilities, and it might be that with careful optimization of the initial beam and detection conditions a few molecules could be detected. More importantly, the measurements confirm our calculations on the deceleration strength the machine was designed for: molecules can be decelerated by 8.7 km/s^2, making it possible to completely stop a 295 m/s SrF(1, 0) beam in a 5 m long decelerator.

The simulations have been scaled on the guiding signal to match the intensity of the non-decelerated part of the detected molecules. The height of the decelerated peak in the simulation for the strongest deceleration is higher than measured, which we attribute mostly to suboptimal experimental conditions. During the experiments the laser ablation power gradually reduced and the poor regulation of the valve temperature caused the supersonic expansion to change slightly. The experiment with the strongest deceleration is the most sensitive to these effects, because of the increased sensitivity to the timing of the molecular pulse relative to the start of the deceleration, since the phase-space acceptance is rather small.

Even with these suboptimal experimental conditions, we transported 4 % of

the SrF(1, 0) molecules at the designed maximal deceleration strength for the 300 m/s beam. Improving the stability of the cold source will result in better timing control over the beam such that the synchronization between supersonic expansion, ablation, and high-voltage switch-on times can lead to more densely filled potential wells. Under those circumstances, transporting 10 % of the guided molecules seems feasible.

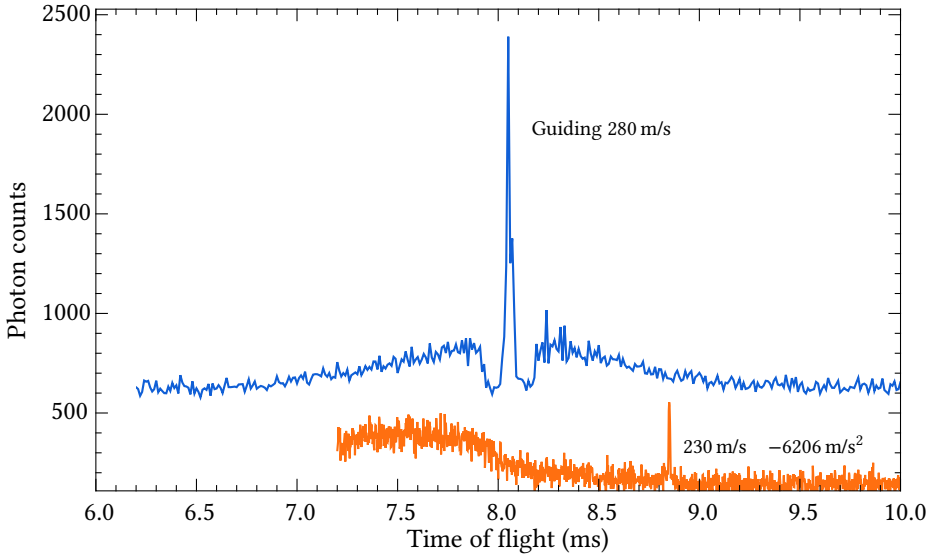

Figure 5.8: Slow beams having an initial velocity of 280 m/s in the laboratory frame were produced. Here we show the TOF for a guided beam at this velocity, and such a beam being decelerated to a final velocity of 230 m/s. A different vertical offset was added to the measurements for clarity.

Further valve cooling for lower initial velocities We have optimized the valve cooling in order to start with the lowest beam velocities possible. As described above, obtaining beams of 300 m/s was an easy routine in the lab. To go further down in velocity, lower temperatures were needed but the regulation system we used at the time to stabilize the valve temperature was not working reliably as described in Chapter 4. Furthermore, the thermocouple readings from the valve body were sometimes inaccurate because of the wires making electrical contact to other parts inside the source chamber. As lower temperatures increased the risk of creating Xe clusters or droplets, we could only create good beams with a velocity of 280 m/s for a few days on and off. In the meantime we have worked

on stabilizing the temperature and expect to be able to use the starting velocity of 280 m/s for future deceleration experiments. The first results obtained with these slow beams are shown in Figure 5.8 and demonstrate that we can make and successfully decelerate these slow beams. The results show that cooling of the valve does not reduce the beam luminosity, making it the preferred option rather than taking the less populated slow part of the velocity distribution from a hotter valve. Reducing the initial velocity from 300 m/s to 280 m/s makes it possible to reach standstill using only 4.5 m of decelerator at full deceleration strength, instead of needing 5 m: an improvement of 10 %. Alternatively, using a full length of 5 m, the deceleration strength could be reduced from 8710 m/s^2 to 7840 m/s^2, increasing the phase space acceptance of the decelerator by a factor 2–3 as can be deduced from Figures 3.4 and 3.6.

Acceleration We have performed acceleration measurements with a beam of initial velocity 341 m/s, in order to show the versatility of the decelerator using arbitrary waveform generators. In the first experiment we accelerated the beam to 371 m/s and in a second measurement we started with decelerating the beam to 330 m/s and then halfway the decelerator started accelerating back to 341 m/s. The TOF spectra are shown in Figure 5.9a and demonstrate that this procedure works. It can be seen that the spectrum from the 341 m/s → 330 m/s → 341 m/s measurement is heavily modulated. This is because the phase space bunching now happens twice as shown in the phase space diagram of Figure 5.9b. Furthermore the molecules undergo an abrupt repositioning because the trap positions shift while changing from deceleration to acceleration. For this shift in position we can correct using modified waveforms as we described in [74], however that was not done here. Instead, the high number of molecules detected after undergoing deceleration and acceleration, together with the phase space plot show the stability of the traveling-wave deceleration process against sudden changes in the electric fields.

5.3 Conclusions

In this chapter we reported the first Stark deceleration of SrF molecules and the first use of a modular traveling-wave Stark decelerator in general. These measurements demonstrate the successful combined operation of the supersonic expansion source of SrF(1, 0) molecules, the 2 m long modular decelerator and the laser-induced fluorescence detection. We observe good signal to background ra-

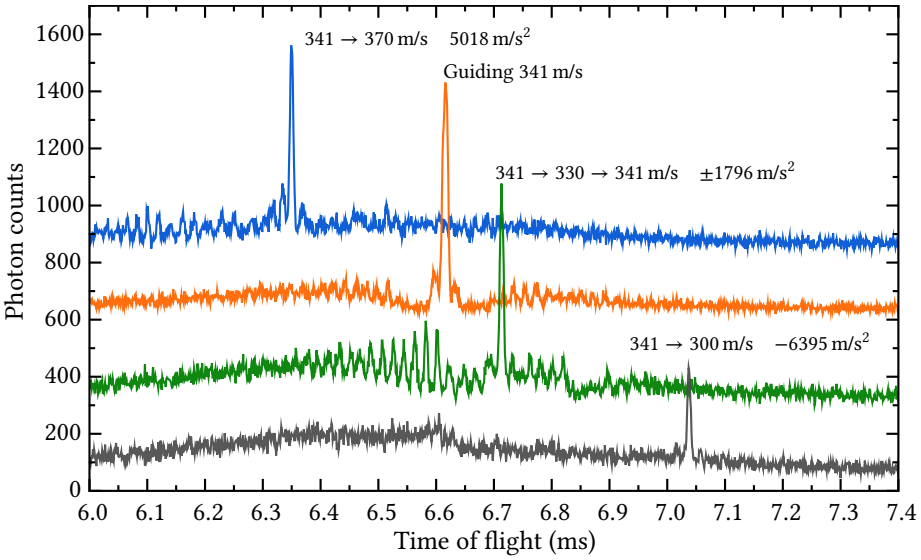

(a) From top to bottom, TOF spectra are shown for: acceleration from 341 m/s to 370 m/s, guiding at 341 m/s, deceleration from 341 m/s to 330 m/s for half of the decelerator length followed by acceleration to 341 m/s, and deceleration from 341 m/s to 300 m/s. A different vertical offset was added to the measurements for clarity.

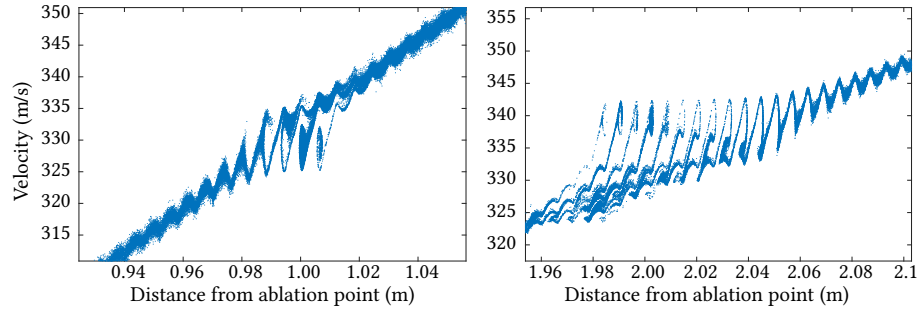

(b) The simulated phase space diagram for the combined deceleration-acceleration experiment, for the molecules after 3 ms (left) and 6 ms (right) of flight time, showing the bunching effect.

Figure 5.9: Guiding, deceleration and acceleration of molecules in the 2 m long decelerator.

tios and find that the measured TOF spectra can be well described by simulations. In later experiments, not shown here, we have seen that the ablation power could be increased significantly without damaging the tablet, giving a correspondingly

higher yield of SrF molecules. A further increase in SrF signal may be obtained by better rotational cooling of the beam in the supersonic expansion, or by means of transferring population to the low-field seeking sub-states of the $N = 1$ level. Extension of the decelerator to 5 m is underway, and based on the results presented in this work it is expected to deliver completely stopped bunches of SrF molecules. We have also shown that, by cooling the valve, SrF beams with an initial velocity of 280 m/s can be created, making it possible to fully stop the beam in a decelerator of 4.5 m. This can be exploited to reduce the decelerator length and construction effort, or to increase the phase space acceptance of the decelerator by lowering the deceleration strength. Such a decelerator is a generic device, extending the range of molecules that can be decelerated and trapped. These include relatively heavy molecules with an unfavorable Stark shift such as SrF, YbF and PbO, larger complex molecules such as benzonitrile [104], but also lighter molecules that have so far eluded Stark deceleration such as water. We expect these cold samples of molecules, especially in combination with further cooling methods, to be the starting point for many exciting future experiments.

6 | Summary and outlook

Recent advances in molecular spectroscopy have finally opened the realm of performing the most precise fundamental physics tests. It was already predicted in the 1960s and 1970s that the energy level structure of diatomic molecules leads to much enhanced sensitivities to violation of the fundamental symmetries parity, time reversal, and charge conjugation. It has taken almost forty years of research and technical development before these enhanced sensitivities in molecules could be exploited in experiments. In the last decade experiments with molecular beams were able to set limits on theories beyond the Standard Model of particle physics that are more stringent than those coming from the high-energy collider experiments. The key factors in this kind of molecular experiments are, besides the intrinsic high sensitivity of the molecules, the available number of molecules, their quantum state purity and the very high degree of experimental control over the molecules. With all these parameters under control the molecular beam velocity becomes the limiting factor, because it prohibits long coherent measurement times. A major improvement in the experiments can therefore be obtained with cold and slow packets of molecules.

In cold samples the population is distributed over only a small number of states. Thus, most of the molecules in the sample can be used for the measurement, improving the statistics of measurements. Experiments with cold samples suffer less from Doppler broadening and can be confined to small spaces such that it is easier for the experimenter to guarantee homogeneity of applied electric and magnetic fields. Other systematic errors that depend on the molecules' velocity or motion can also be reduced. Since cold samples can be confined in space, the measurement time can be longer than for a sample that passes through the apparatus at high velocity. Cold samples allow for coherent measurement times on molecules up to 1 s, mostly limited by blackbody radiation losses. So far, most of the experiments have used cold molecular beams. These beams are

internally cold, such that the quantum state purity and high numbers in the relevant states are guaranteed. However, the velocity of these beams is of order 100 m/s to 600 m/s and the interrogation time of the molecules is thus limited by the size of the apparatus. This time is usually around a few hundred microseconds only, and this is where the potential for improvement lies. Reducing the speed of the beam would extend the measurement time by an order of magnitude, whereas fully stopping a molecular beam and confining the sample in a trap would mean the ultimate completion of this idea.

In this thesis we describe the development, building and working of an experiment that has the goal of fully decelerating and trapping a molecular beam for the purpose of fundamental physics experiments. Based on available literature, we selected the SrF radical as an excellently suited candidate molecule because of its high sensitivity as a probe of parity violation, its suitable properties for deceleration and laser cooling at a later stage. For the deceleration, we build on

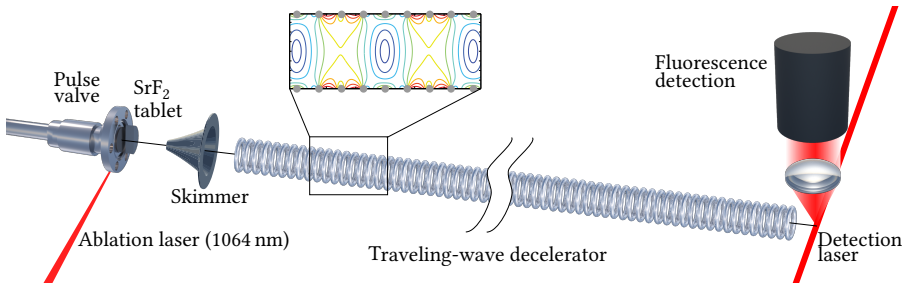

Figure 6.1: A schematic overview of the experimental setup. SrF molecules are created by laser ablation from a tablet. A pulsed supersonic xenon expansion cools the SrF molecules and takes them to the ring structure where the molecules are guided or decelerated. Further downstream SrF molecules are detected by laser induced fluorescence.

the pioneering experiments from the group of Meijer at the Fritz Haber Institute in Berlin [11, 12]. They showed the first deceleration of molecules using the Stark effect, and also developed a traveling-wave Stark decelerator. Traveling-wave deceleration is based on genuine three-dimensional potential wells which are formed by closed electric field lines as depicted in Figure 6.1. Molecules with an electric dipole moment oriented such that their energy is lowest in the minimum of the electric field can be trapped inside these field lines. Once trapped in such a moving potential well, the potential wells can be slowed down, thereby exerting a force on the trapped molecules so that they decelerate as well. This

principle is truly stable and does not lead to molecule losses. Our particular molecule, however, has quite a higher mass than the CO molecule for which the traveling-wave decelerator was demonstrated to work. Furthermore, the Stark shift in SrF is much smaller and also not of low-field seeking character for all electric field strengths. It was therefore necessary to first study the traveling-wave deceleration process for SrF with simulations. We found that it is indeed possible for a beam of SrF coming from a supersonic expansion in xenon to be decelerated to standstill in a length of 5 m, and this is reported on in **Chapter 3**. We calculated that a 5 meter long decelerator with modest applied voltages (amplitude of 8 kV) has a total phase-space acceptance for deceleration in the second excited rotational state of about 2×10^4 mm^3(m/s)^3. This is at least an order of magnitude larger compared to alternative deceleration methods using a similar decelerator length and deceleration strength, but operating at much higher voltages ($\pm$40 kV). We have also estimated the potential gain in sensitivity of using the decelerated molecules for a parity violation measurement. Compared to a cryogenic molecular beam experiment, the decelerated molecules provide a gain in sensitivity of up to two orders of magnitude due to the increased interaction time, while maintaining a comparable molecular flux. By combining this efficient form of Stark deceleration with a final stage of laser cooling a robust method to create ultracold trapped samples of heavy diatomic molecules is within reach.

In **Chapter 4** we have described the design and construction of a 5 m long traveling-wave Stark decelerator, based on the results from the simulations. We demonstrated that we could build the decelerator within the designed tolerances. We use custom-made high voltage amplifiers to generate the high voltages for the decelerator. The capacitive load on these amplifiers is such that they can only work at a maximal amplitude of 5 kV. This limits the acceptance of our decelerator considerably. However, these amplifiers, combined with arbitrary waveform generators, enable us to exert full control over the trapping potentials and manipulate them as we like. Also in **Chapter 4**, we have described the rest of the experimental setup. To produce SrF molecules, we have built a compact supersonic expansion source using xenon as the carrier gas, in which we seed SrF by laser ablation from a pressed SrF_2 target. For detecting the molecules, a laser system was set up in the lab, together with a detection system for laser induced fluorescence detection.

The results of all the preparatory work are reported in **Chapter 5**. In this chapter we first show the characteristics of the molecular beam as it originates from the source. We have shown that it is indeed possible to create stable beams

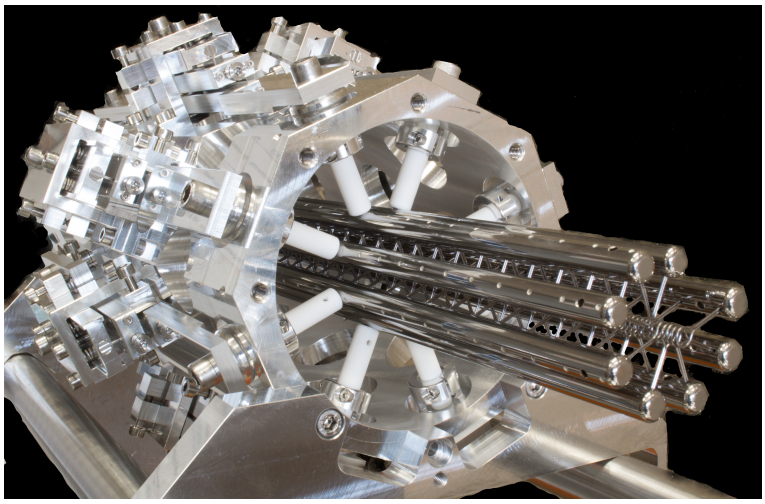

Figure 6.2: A photo of one module of the traveling-wave decelerator, showing the periodic ring structure and the alignment mechanisms. The stainless steel rods are mounted via insulating MACOR posts onto aluminum bars, which can be precisely positioned using the alignment mechanism.

of SrF with a speed of 300 m/s, and showed promising steps towards even lower velocities. Rotational spectra were measured that indicate that the rotational temperature of the molecules in the beam is around 10 K. These spectra demonstrate that indeed the beam is cold and that there are sufficient molecules in the rotational state to show deceleration. After having established this, we showed the first deceleration of SrF radicals in a traveling-wave Stark decelerator. It also constituted the first successful use of a modular traveling-wave Stark decelerator in general. Using a decelerator of 2 m length, we were able to decelerate a beam from 300 m/s to 234 m/s, thereby taking away about 40 % of the kinetic energy. These measurements demonstrate the successful combined operation of the supersonic expansion source of SrF$(1, 0)$ molecules, the 2 m long modular decelerator and the laser-induced fluorescence detection. We compared the measured time-of-flight spectra to simulations and found a good agreement between the two, demonstrating that we understand the working of the apparatus very well.

Outlook

Extension of the decelerator to 5 m is underway, and based on the results presented in this thesis it is expected to deliver completely stopped bunches of SrF molecules. We have also shown that, by cooling the valve, SrF beams with an initial speed of 280 m/s can be created, making it possible to fully stop the beam in a decelerator of 4.5 m length. This can be exploited to reduce the decelerator length and construction effort, or to increase the phase space acceptance of the decelerator by lowering the deceleration strength. We have identified a number of points on which the SrF source could be improved. Stabilizing the valve temperature would allow for proper optimization of the overlap of the gas pulse and the ablation, and for optimization of the rotational temperature. Furthermore, the ablation process itself could be improved by using more laser power. With all those improvements, it should be possible to decelerate to standstill about 1×10^3 SrF$(1, 0)$ molecules per shot. It is also worthwhile to investigate optical pumping of molecules from high-field seeking states to low-field seeking states in order to increase the number of decelerated molecules. The traveling-wave deceleration of SrF will be combined with laser cooling to decrease the temperature of the trapped molecules. The unique combination of a Stark decelerator and laser cooling would make it possible to make 10^3 ultracold SrF molecules per shot, making the combination of the two techniques a factor of two better than direct laser cooling SrF from a cryogenic buffer gas source [156].

Our long, modular traveling-wave decelerator is a generic device, extending the range of molecules that can be decelerated and trapped. These include relatively heavy molecules with an unfavorable Stark shift such as SrF, YbF and PbO, larger complex molecules such as benzonitrile [104], but also lighter molecules that have so far eluded Stark deceleration such as water. However, it seems not practical and not affordable to build modular decelerators that are much longer than 5 m. Therefore, in order to be able to fully stop beams of molecules heavier than SrF, lowering the initial beam velocity is a necessity. This can be achieved by replacing the supersonic expansion source by a cryogenic buffer gas source. For some molecules, laser slowing before entering the decelerator can also be an option. In general, using higher voltages than 5 kV would be beneficial for the traveling-wave deceleration process. If more powerful high-voltage amplifiers cannot be built, transformers could be used to provide the voltages for the first part of the decelerator. The final slowing and static trapping can then be left to the amplifiers, reducing the load on those considerably. We have shown in collaboration experiments [73, 74] with the group of Bethlem at the VU University

in Amsterdam that the use of arbitrary waveform generators for providing the deceleration voltages enables full control over the traps as we like. This makes it possible to cool the trapped molecules by adiabatically expanding the trap. Further work on laser cooling the decelerated SrF is underway [111], as well as optical dipole trapping of SrF. That will be the starting point for exciting new molecular experiments, for example on parity violation, electron EDMs, dark matter searches, or dipole-dipole interactions.

7 | Nederlandse samenvatting

Het bouwen van een bijna vijf meter lange molecuulafremmer, bestaande uit duizenden onderdelen die op honderdsten van een millimeter precies moeten worden uitgelijnd, is geen eenvoudige opgave. Zo'n complexe machine is echter wel een van de weinige manieren om relatief zware moleculen in een vacuümkamer tot stilstand te kunnen brengen. Met die stilgezette moleculen kunnen we vervolgens zeer precieze metingen doen om te testen of het zogenaamde Standaardmodel van de deeltjesfysica wel klopt, of dat er uitbreidingen van dat model nodig zijn. Het Standaardmodel beschrijft in één samenhangende theorie hoe alle elementaire deeltjes door middel van de zwakke kernkracht, de sterke kernkracht en elektromagnetisme met elkaar wisselwerken. Ook verklaart het dat de deeltjes massa hebben vanwege het onlangs ontdekte Higgsdeeltje. Hoewel het Standaardmodel zeer succesvol en extreem nauwkeurig is, weten we ook dat het niet alles in de natuurkunde omvat. Zo wordt de zwaartekracht er niet door beschreven, geeft het geen verklaring voor het nagenoeg ontbreken van antimaterie in het heelal, beschrijft het niet de donkere materie en donkere energie die nagenoeg de totale energiedichtheid van het heelal vormen en verklaart het evenmin waarom sommige natuurconstanten de waarde hebben die ze nu eenmaal hebben. Inmiddels hebben theoretisch natuurkundigen talloze uitbreidingen op het Standaardmodel voorgesteld, die een of meerdere van deze hiaten proberen te vullen. Veel van die theorieën voorspellen het bestaan van extra fundamentele deeltjes die ook in experimenten te zien zouden moeten zijn. Zeer bekende experimenten die naar zulke nieuwe deeltjes zoeken worden uitgevoerd met de gigantische deeltjesversneller LHC bij CERN in Genève. Daar probeert men, door zeer snel bewegende deeltjes met enorme energieën frontaal op elkaar te laten botsen, nieuwe deeltjes te ontdekken in de brokstukken die na de botsingen verschijnen.

Een molecuulafremmer is zo'n beetje het tegenovergestelde van een deeltjes-

versneller. Maar ook een afremmer kan gebruikt worden om naar afwijkingen aan het Standaardmodel te zoeken. Nieuwe deeltjes veroorzaken namelijk ook indirect zeer subtiele afwijkingen in de structuur van moleculen. Omdat die afwijkingen zo klein zijn, kun je ze alleen meten als je zeer precieze metingen doet die ongevoelig zijn voor allerlei verstorende externe factoren. Juist door moleculen in vacuüm stil te zetten met een afremmer, en ze heel koud te maken, kunnen de moleculen zo geprepareerd worden dat de gewenste precisie haalbaar wordt. Dat stilzetten is het doel en pas ongeveer vijftien jaar geleden is het afremmen van molecuulbundels voor het eerst gedemonstreerd in de groep van Meijer in Nijmegen. Men gebruikte toen een type afremmer dat goed werkte voor lichte moleculen maar dat problemen had met zwaardere, vooral bij langzame eindsnelheden. Juist de zware moleculen zijn het meest geschikt om precisiemetingen aan het Standaardmodel te doen, omdat ze een grote intrinsieke gevoeligheid hebben voor het bestaan van nieuwe fysica. Helaas is het afremmen lastiger, om twee redenen. Ten eerste zorgt de grotere massa, bij een gelijke beginsnelheid, voor een langere remweg, waardoor een langere afremmer nodig is. Ten tweede zorgt de molecuulstructuur ervoor dat de maximale vertraging die bij het afremmen gebruikt kan worden vrij laag is, waardoor eveneens de afremmer langer dient te zijn. Een traditionele, geschakelde afremmer zou vanwege die lengte te veel verliezen kennen, en is daarom ongeschikt. Als alternatief werd, eveneens in de groep van Meijer, nu in Berlijn, een 50 cm lange lopendegolf-Starkafremmer gebouwd en gebruikt voor het afremmen van het lichte molecuul CO. Dit type afremmer kent in principe geen verliezen, waardoor een grotere lengte mogelijk is. Op die manier zouden ook de gewenste zware moleculen kunnen worden afgeremd. In dit proefschrift wordt eerst met computersimulaties aangetoond dat dit inderdaad het geval is om vervolgens de bouw van een lange afremmer te beschrijven en het daadwerkelijk succesvol afremmen van zware SrF (strontiummonofluoride) moleculen te demonstreren. We hebben SrF gekozen omdat het goede eigenschappen heeft voor het afremmen, het verder afgekoeld kan worden met laserlicht en het gevoelig is voor pariteitschending. Pariteitsymmetrie, ofwel spiegelsymmetrie, wordt volgens het Standaardmodel geschonden door de zwakke kernkracht. Om deze schending te kunnen onderzoeken zijn zeer precieze metingen nodig, omdat het effect zo klein is. Met atomen zijn dergelijke metingen al verricht maar met moleculen nog niet, hoewel de gevoeligheid in SrF tot honderdduizend keer groter is. Met afgeremde en stilgezette moleculen worden zeer beperkt geteste parameters van het Standaardmodel toegankelijk voor metingen. Op basis van deze eigenschappen lijkt SrF dus een uitstekend

molecuul om af te remmen.

Een schematisch overzicht van het experiment is te zien in Figuur 7.1. In het kort bestaat het uit een molecuulbron die pakketjes moleculen met hoge snelheid in de afremmer schiet. In de afremmer worden de moleculen bij elkaar gehouden en als pakketje afgeremd. Aan het eind van de afremmer worden de afgeremde moleculen gedetecteerd of verdere experimenten gedaan. We zullen nu eerst de werking van de afremmer uitleggen alvorens de verdere details en uitkomsten van het onderzoek te bespreken.

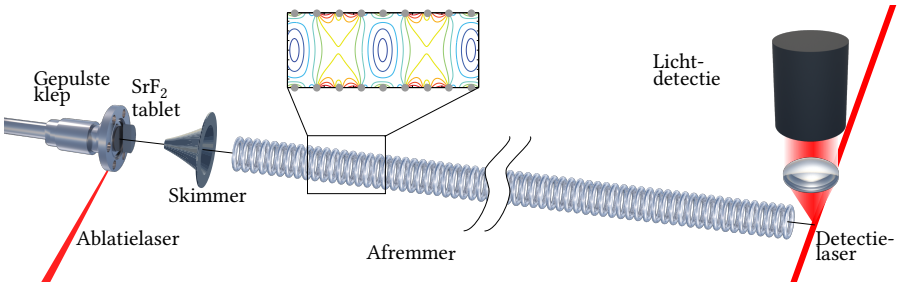

Figuur 7.1: Een schematisch overzicht van het experiment. In werkelijkheid bevindt alles zich in een grote vacuümkamer. Voor een volledige uitleg, zie de tekst. In het kort worden SrF moleculen gemaakt door middel van laserablatie. Een gepulste expansie van xenongas koelt de SrF moleculen en neemt deze mee in de afremmer. Daarbij laat de skimmer alleen de moleculen door die in een rechte lijn op de as bewegen. De afremmer bestaat uit ringvormige elektrodes. Door elektrische spanningen op de elektrodes te zetten ontstaan elektrische velden zoals weergegeven in de uitvergroting. Aan het einde van de afremmer kunnen de moleculen met laserlicht gedetecteerd worden.

Neutrale moleculen afremmen met het Stark-effect

Deeltjesversnellers kunnen efficiënt werken omdat ze gebruik maken van geladen deeltjes of ionen. Met elektrische en magnetische velden kunnen ionenbundels versneld en gestuurd worden. Wij zijn echter geïnteresseerd in neutrale moleculen, die geen lading hebben. We kunnen wel slim gebruik maken van de ladingsverdeling in het molecuul. Ieder eenvoudig lineair molecuul dat uit twee verschillende atomen bestaat heeft netto meer negatieve lading bij het ene atoom en netto meer positieve lading bij het andere. Zo'n molecuul heeft hierdoor een zogenaamd dipoolmoment. Wanneer zo'n molecuul in een elektrisch veld geplaatst wordt, zal het gaan draaien totdat het anti-parallel ligt aan de elektrische

veldlijnen, ongeveer zoals een kompasnaald dat doet in een magneetveld. Verder zorgen kwantummechanische effecten ervoor dat deze moleculen aangetrokken worden tot hoge of lage elektrische veldsterktes, afhankelijk van de toestand waarin de moleculen geprepareerd worden. Dat principe gebruiken we in de afremmer. Onze afremmer bestaat uit ringvormige metalen elektrodes die in een lange rij achter elkaar geplaatst zijn. Op elk van die elektrodes wordt een elektrische spanning gezet. Daardoor ontstaat er een elektrisch veld in de afremmer. In Figuur 7.2 is te zien hoe dat eruitziet. In de afremmer ontstaan een soort drie-

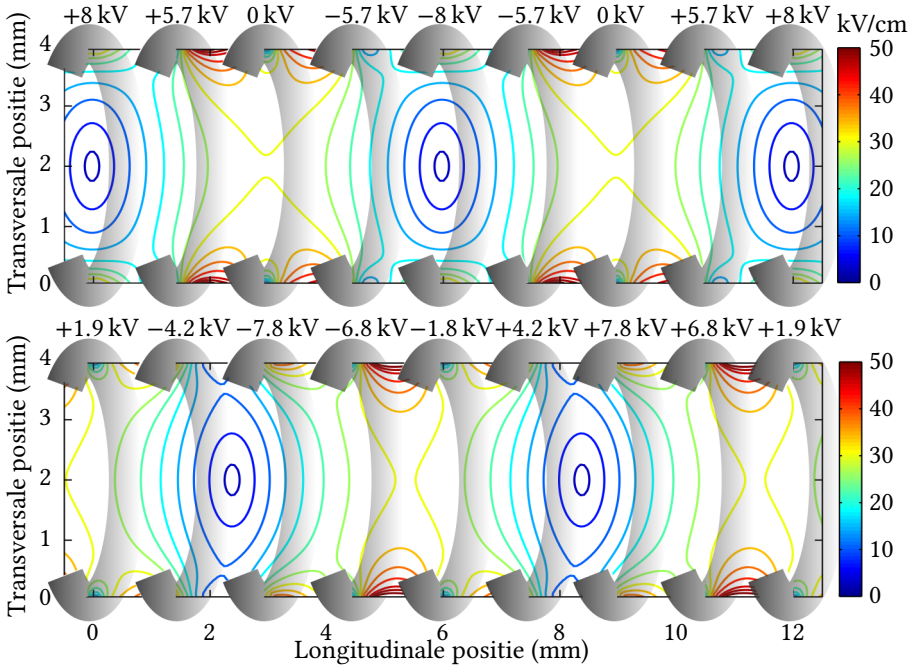

Figuur 7.2: Een langsdoorsnede door de ringetjes van de afremmer op twee verschillende tijdstippen. Binnen de ringen zijn lijnen van gelijke elektrische veldsterkte getekend. De blauwe cirkels vormen een minimum van het elektrisch veld, en zijn daarmee een soort driedimensionaal putje waarin laagveldzoekende moleculen gevangen worden. Door de spanningen in een golf over de ringetjes te laten lopen, bewegen de putjes naar rechts.

dimensionale putjes waarvan in het centrum het elektrisch veld minimaal is. Als een laagveldzoekend molecuul eenmaal daarin belandt, kost het energie om daar weer uit te klimmen. Indien het putje diep genoeg is, dan zal het molecuul erin opgesloten blijven en niet kunnen ontsnappen. Omdat onze moleculen met on-

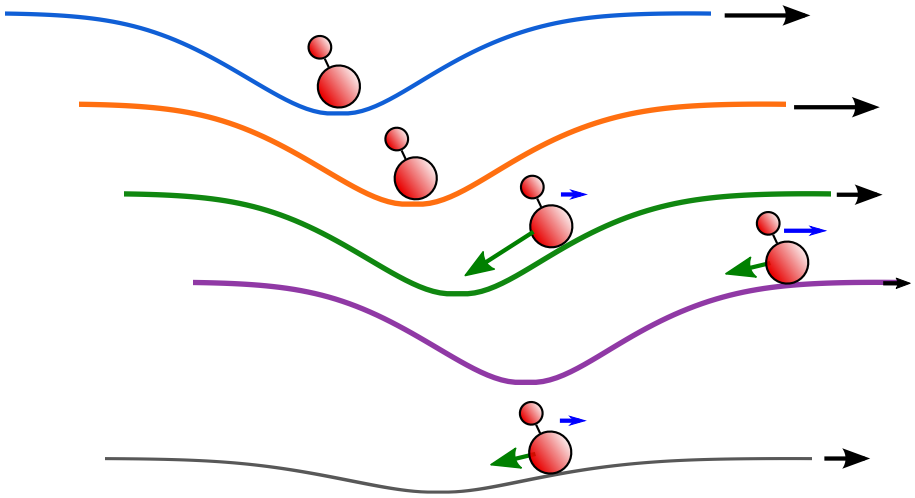

Figuur 7.3: Een schematische weergave van de moleculen in afremmende putjes. Blauw en oranje: een molecuul zit gevangen in het diepste punt en de putjes en moleculen bewegen met dezelfde snelheid. Het molecuul blijft in het putje gevangen. Groen: het putje remt af dus schiet het molecuul naar voren (blauwe pijl). Door de diepte en steilheid van het putje wordt het nog steeds aangetrokken naar het diepste punt (groene pijl) waardoor het niet kan ontsnappen. Paars: het putje wordt te snel afgeremd waardoor het molecuul nauwelijks nog tot het diepste punt wordt aangetrokken. Het molecuul ontsnapt. Grijs: bij een ondiep putje is de aantrekkingskracht lager en ontsnapt het molecuul eerder.

geveer 1100 km/h de afremmer binnenvliegen, moeten we de putjes ook met die snelheid laten bewegen om de moleculen in te vangen. Anders vliegen ze er hard in, om er aan de andere kant weer uit te rollen, net als een knikker die met te veel vaart aan de andere kant van het putje er weer uit rolt. Maar als we ze eenmaal in de bewegende putjes gevangen hebben, kunnen we de moleculen gaan afremmen door de snelheid van de putjes geleidelijk omlaag te brengen. Hierbij geldt dat hoe dieper het putje is, hoe harder we kunnen afremmen. Dit is goed te begrijpen door naar een treinreiziger te kijken met een bekertje koffie in zijn hand: als de trein te hard remt dan klotst de koffie over de randen van het bekertje. Te hard afremmen zorgt er op dezelfde manier voor dat de moleculen uit de putjes vliegen en verloren raken voor het experiment. Schematisch is dit te zien in Figuur 7.3. We bewegen de putjes door de hoogspanning over de ringetjes als een wisselspanningsgolf te laten lopen. Vandaar de term lopendegolf-Starkafremmer.

De snelheid van de golf kunnen we regelen door de frequentie van de wisselspanning aan te passen tussen de 30 kHz en gelijkspanning voor stilstand. Hiervoor zijn speciale hoogspanningsversterkers nodig. Het is in theorie eenvoudig om de elektrische putjes veel dieper te maken door de elektrische spanning op te schroeven of de ringetjes dichter bij elkaar te plaatsen. Helaas is dat in de praktijk technisch onhaalbaar; de versterkers die we gebruiken voor de hoogspanning zijn uniek en speciaal gebouwd om het maximale uit ons experiment te halen. Bovendien is de diepte van de putjes ook afhankelijk van de gevoeligheid van de moleculen zelf voor de elektrische velden. De grootste uitdaging van de voor ons interessante moleculen is dat die gevoeligheid vrij laag is en zelfs afneemt als de elektrische veldsterkte wordt opgevoerd voorbij een bepaald punt. De natuur beperkt ons hier dus in de maximale vertraging die gebruikt kan worden voor het afremmen.

Dit proefschrift: afremmen van SrF

In **Hoofdstuk 3** van dit proefschrift hebben we computersimulaties gedaan om te berekenen wat de maximale vertraging kan zijn en hoe lang de afremmer dan moet worden. Het blijkt mogelijk te zijn om SrF moleculen die met een beginsnelheid van 300 m/s (1080 km/h) binnenvliegen, in vijf meter af te remmen met een vertraging van 9000 m/s^2, wat ongeveer duizend keer sterker is dan de maximale remvertraging van een auto. De hele afremprocedure duurt dan 33 duizendste van een seconde. De hoeveelheid SrF moleculen die succesvol kan worden afgeremd zonder in het proces verloren te gaan is ongeveer tien keer meer dan in andersoortige afremmers. We berekenden ook hoe de gevoeligheid voor een meting van pariteitschending verbeterd wordt door de moleculen na het afremmen in de stilgezette putjes vast te houden. Op die manier kan er langer, en dus preciezer, gemeten worden. In combinatie met verdere laserkoeling verbetert de precisie van zo'n meting met een factor van een paar honderd ten opzichte van snelle moleculaire bundelexperimenten.

In **Hoofdstuk 4** wordt vervolgens de bouw van een lange afremmer beschreven. Allereerst moest er een bronkamer gebouwd worden. SrF moleculen zijn radicalen en zo reactief dat ze niet in een flesje verkrijgbaar zijn. Daarom moeten ze ter plekke in een vacuümkamer gemaakt worden. In de bronkamer maken we tien keer per seconde een molecuulwolkje door met een gepulste laser op een tablet van samengeperst SrF_2 te schieten. Door het intense laserlicht wordt het tablet plaatselijk verhit waardoor er een wolkje SrF moleculen verdampt. Dat proces heet ablatie. Tegelijkertijd wordt er heel kort een gasklepje geopend waar-

door xenongas de kamer binnen kan stromen. Dit xenongas botst vervolgens met het zojuist gemaakte wolkje SrF en neemt dit vervolgens mee op zijn weg naar de afremmer. Hierbij koelen de moleculen ook aanmerkelijk af: doordat het xenongas vanuit hoge druk vrij expandeert in het vacuüm wordt het kouder, net als het gas dat uit spuitbussen komt. De temperatuur van de moleculen is na de expansie ongeveer 10 graden boven het absolute nulpunt, oftewel −260 °C. Die lage temperatuur is belangrijk omdat alleen de echt koude moleculen elektrische laagveldzoekers zijn die we kunnen vangen in de afremputjes. Helaas gaat alleen voor niets de zon op, want die lage temperatuur kan alleen gehaald worden als het xenongas zo snel mogelijk uit de klep vliegt. Dat heeft tot gevolg dat de SrF moleculen met een zeer hoge snelheid de afremmer binnenvliegen, te snel om in vijf meter af te remmen. Om deze snelheid te reduceren, en toch een goede koeling te behouden, wordt de klep waaruit het xenon stroomt gekoeld met zeer koud stikstofgas. We konden door de koeling de snelheid van ruim 1300 km/h terugbrengen naar 1080 km/h, waardoor het afremmen binnen de vijf meter moet lukken.

Het ontwerp van de afremmer en de toleranties daarop zijn vastgesteld op basis van de computersimulaties. Ook zijn er verschillende hulpstukken gemaakt om bij de constructie van de afremmer binnen de toleranties te blijven. Nagenoeg alle onderdelen van de afremmer zijn in de eigen instrumentmakerij van het KVI gemaakt. De afremmer bestaat uit modules van 50 cm die achter elkaar worden geplaatst in de vacuümkamers. Uiteindelijk is er in het tijdsbestek van dit promotieonderzoek een afremmer van vier meter gebouwd die voldoet aan alle ontwerpeisen. Voor het genereren van de hoogspanningsvoltages op de elektrodes werden speciale versterkers gebouwd door Trek Inc. uit de Verenigde Staten. De maximale uitgangsspanning van 5 kV maakt dat de molecuulputjes minder diep zijn dan gewenst. Het gebruik van betere versterkers zou het aantal ingevangen moleculen sterk kunnen verhogen.

Hoofdstuk 4 besluit met de beschrijving van de laser- en detectiesystemen die gebouwd zijn om de moleculen in de afremmer te detecteren. De SrF moleculen kunnen gedetecteerd worden door er met laserlicht van een specifieke golflengte op te schijnen, waarna de moleculen oplichten. Het oplichten van de moleculen kan met een lichtgevoelige detector worden waargenomen. Door het detectiesysteem aan het eind van de afremmer te plaatsen, en de tijd te registreren wanneer het licht wordt waargenomen ten opzichte van de laserpuls die in de bronkamer de SrF moleculen maakt, kan de vluchttijd van de moleculen in de afremmer worden bepaald. Aangezien de lengte van de afremmer bekend is,

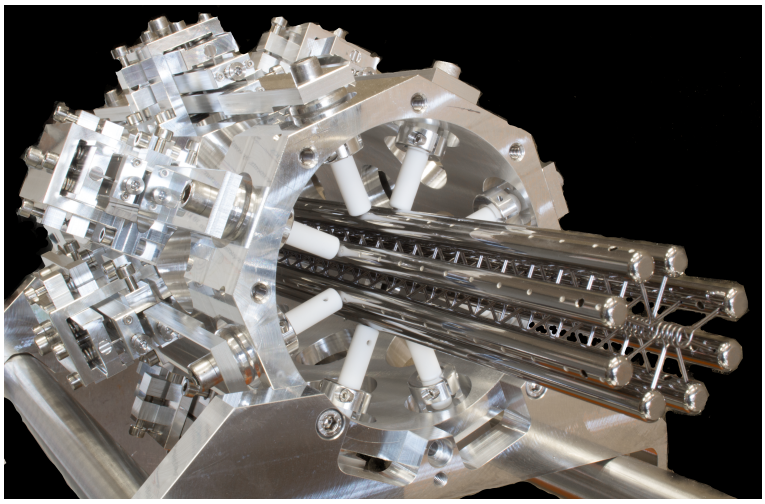

Figuur 7.4: Een foto van één van de afremmodules. Te zien zijn de stangen met ringvormige elektrodes in een achthoekige behuizing. Aan de buitenkant bevinden zich verschillende instelmechanismes. De witte staafjes dienen als elektrische isolatie tussen de behuizing en de staven onder hoogspanning.

volgt daaruit dan ook de gemiddelde snelheid.

De resultaten van al deze voorbereidende simulatie- en bouwwerkzaamheden staan vermeld in **Hoofdstuk 5**. Eerst tonen we dat het inderdaad mogelijk is om met de gekoelde klep de relatief langzame, koude SrF molecuulbundels te maken. Bovendien liggen nog lagere snelheden in het verschiet, mits de klepkoeling verder gestabiliseerd wordt. Nadat de werking van de bron voldoende was aangetoond, hebben we als eersten het afremmen van SrF in dit type afremmer laten zien. Bovendien was dit de eerste keer dat de goede werking van een modulaire lopendegolf-Starkafremmer gedemonstreerd werd. De metingen aan het afremmen werden gedaan toen de afremmer nog maar twee meter lang was. Met deze twee meter afremmer konden we SrF afremmen van 1080 km/h naar 842 km/h. Dat komt overeen met een reductie van 40 % van de bewegingsenergie van de moleculen. We maten met de lichtdetectie de aankomsttijd van de moleculen en vergeleken die met computersimulaties. We vonden een goede overeenkomst tussen beide. Hieruit concluderen we dat we een goed begrip van de werking van de afremmer hebben.

Vooruitblik

Op basis van de genoemde resultaten met de twee meter afremmer kan ervan worden uitgegaan dat het compleet tot stilstand brengen van SrF moleculen in een vijf meter lange afremmer inderdaad gaat lukken. Een paar metingen lieten zien dat de gasklep nog beter gekoeld kan worden. Hierdoor zouden lagere snelheden mogelijk zijn die afremmen tot stilstand in vierenhalve meter mogelijk maken. Dat zou het constructieproces van de volledige afremmer kunnen bekorten. Alternatief kan toch de volledige vijf meter gebouwd worden, en de vertraging minder sterk worden ingesteld waardoor er meer moleculen afgeremd kunnen worden. Tijdens het onderzoek zijn er punten aan het licht gekomen die verbeterd kunnen worden. Dit betreft met name de stabilisatie van de kleptemperatuur, de juiste overlap van de xenonpuls met de SrF wolk en het laservermogen dat gebruikt wordt in het ablatieproces. Met verbeteringen op die punten moet het mogelijk zijn om per schot duizend SrF moleculen tot stilstand te brengen.

Als de moleculen tot stilstand zijn gekomen zullen ze nog verder worden afgekoeld met laserlicht. De unieke combinatie van een afremmer en laserkoeling maakt het mogelijk om duizend ultrakoude SrF moleculen per schot te maken, een factor twee meer dan wat nu elders wordt gehaald door middel van directe laserkoeling.

Onze lange, modulaire lopendegolf-Starkafremmer is een uniek en veelzijdig apparaat. Het stelt ons in staat om zware, interessante moleculen die eerder niet voor afremmen in aanmerking kwamen, toch stil te zetten. Als voorbeelden noemen we SrF, YbF, PbO en grotere complexe moleculen zoals benzonitril, maar ook lichtere moleculen zoals water. Doordat de lengte van vijf meter in de praktijk niet gauw overschreden zal worden, is het voor de zwaardere moleculen dan SrF wel noodzakelijk om de beginsnelheid van de moleculen aanzienlijk te verminderen. Dit kan door een ander type bron te gebruiken. Ook zou het afremmen beter gaan met hoogspanningsversterkers die hogere spanningen kunnen leveren. Ook is het opdelen van de afremmer in secties een optie. In het begin zouden dan transformatoren kunnen worden ingezet, en de hoogspanningsversterkers in het laatste stuk. Op die manier kunnen alle voordelen van de versterkers, zoals volledige controle over de vorm en tijdsontwikkeling van de hoogspanning, gebruikt worden voor het in de val opgesloten houden en manipuleren van de moleculen. We hebben reeds in een samenwerking met de Vrije Universiteit Amsterdam de voordelen hiervan laten zien in een experiment waarin we ammoniakmoleculen in een module van onze afremmer tot stilstand hebben gebracht en gedurende langere tijd hebben opgesloten. We verwachten dat de door onze ontwikkelin-

gen mogelijk gemaakte koude wolkjes opgesloten moleculen het begin zullen zijn van vele spannende toekomstige experimenten.

Dankwoord

De afgelopen jaren heb ik met zeer veel plezier mogen werken aan dit proefschrift. Het bouwen van 's werelds grootste molecuulafremmer was een gigantische uitdaging die je alleen met een heel goed team aan kunt gaan. Ik ben dankbaar voor alle hulp, expertise en ook gezelligheid die iedereen van het koudemoleculenteam mij heeft gegeven. Allereerst Imko Smid die de ontwerpen voor de afremmer heeft gemaakt en soms ook onderdelen heeft gemaakt. Imko, volgens jou moest de basis goed zijn, en gelukkig heb jij die gelegd. Dankzij jouw ervaring en vakmanschap konden we alles uitlijnen zoals we het wilden. Bovendien zorgde jouw ongeduld ervoor dat we de nodige vaart maakten met de metingen. Als een tweede directeur gaf je haast leiding aan het experiment. Ook na je pensionering herinnert je foto in de Imko Smidzaal ons daar nog dagelijks aan. Heel veel dank voor al je inzet tijdens je laatste KVI-project. Mijn grote bewondering en dank gaan ook uit naar de instrumentmakerij van het KVI. Roelof Dussel, Dirk Tilman, Sandra Eggens, Nanko de Vries en André de Vries: jullie hebben mij laten zien wat precisie en kwaliteit betekenen. Meestal als ik met een idee bij jullie kwam, werd ik eerst raar aangekeken hoe ik dat nou in mijn hoofd had kunnen halen, waarna jullie een natuurlijk veel betere oplossing opperden en die meestal ook gelijk realiseerden. André, jij was ons aanspreekpunt en je hebt de meeste onderdelen van de afremmer gemaakt. Hartelijk dank voor je grote betrokkenheid bij het project en de heel fijne samenwerking.

Zonder Leo Huisman had dit project geen kans van slagen gehad. Meneer Leo, oneindig veel dank voor het assembleren van de modules, het uitlijnen van de hele afremmer, het bouwen van vacuümsystemen, elektronica, het werk aan de Arduinos en alle andere (technische) ondersteuning. Het was me een enorm genoegen en groot plezier om met jou samen te mogen werken. Ook de knutselprojectjes voor de open dagen of de wetenschapsquiz waren één groot feest.

De aanstichter van dit hele project is natuurlijk mijn promotor Steven Hoeks-

tra. Steven, ik wil je hartelijk danken voor je fijne begeleiding de afgelopen jaren en de vrijheid die je me hebt gegeven in de uitvoering van het project. Ook bij het geven van voordrachten hoefde ik gelukkig nooit te vrezen voor jouw kritische blik vanuit de zaal. Met je kritische blik en instelling probeerde je wel steeds mij aan te sporen om nog diepere inzichten te verkrijgen uit de meetresultaten of zaken scherpzinniger te formuleren. Meestal leidde een vraag aan jou dus, naast het krijgen van een antwoord, ook weer tot verdere vragen. Zoiets houdt het onderzoek leuk. Naast het werk zorgde je ook voor sociale cohesie in het koudemoleculenteam door het geven van kerstdiners bij jou thuis, meestal rond juni. Met name het Braziliaanse zaagselgerecht zal ik niet gauw vergeten.

Mijn promotor Klaus Jungmann wil ik zeer hartelijk danken voor al zijn steun gedurende de afgelopen jaren. Klaus, vanaf het college Subatomaire Fysica heb ik veel over allerlei uiteenlopende natuurkundige onderwerpen van je mogen leren. Je neemt altijd ruim de tijd om vragen te beantwoorden en te voorzien van een bredere context. Hoewel je de inhoud aan Steven overliet, ben ik je wel dankbaar voor je voortdurende belangstelling voor de algemene voortgang van het project. Ook ben ik blij met de vele mogelijkheden die ik heb gehad om verschillende buitenlandse conferenties te bezoeken.

Mijn collega-promovendi Corine, Sreekanth en Artem dank ik voor de samenwerking in het lab en wens ik veel succes met het afmaken van hun eigen proefschriften. Ik ben benieuwd wat voor resultaten er met de afremmer bereikt gaan worden! Veel werk is ook verricht door de afstudeerstudenten en Franse stagiairs. Bedankt Eric, Samuel, Tom, Aernout, Janko, Peter, Nathan, Joram, Jonathan; merci Camille, Franck, Nicolas, Anthony I et Anthony II. Het koudemoleculenonderzoek vindt plaats in het grotere geheel van de groep Fundamentele Symmetriën en Interacties, voorheen TRIμP. Dat zorgde voor de nodige structuur. Donderdagochtend vergadering om kwart over negen met Hans als voortvarende voorzitter, Gerco tegenover mij en altijd weer aan mij de vraag wie moest notuleren. Dank aan iedereen van de groep, voor de belangstelling voor ons experiment en jullie behulpzaamheid: Lorenz, Otto, Oliver, Olivier, Duurt Johan, Wilbert, Amita, Nivedya, Elwin, Auke, Hilde, Corine, Sreekanth, Artem, Bodha, Stefan, Umakanth, Andrew, Gouri en Hendrik. Oscar, het was me een eer en groot genoegen om met jou te werken en ik dank je voor de inzichten die je met me deelde over de natuurkunde in andere labs. Mayer, muchas gracias para llevarme a Colombia para mostrarme tu país, y para tus abrazos. Ook de bevriende theoreten wil ik hier noemen: Rob, Keri, Jacob, Wouter, Jordy en Sophie. Lotje, dank voor al je welgemeende levensadviezen. Dank ook aan de organisatie van

de FANTOM-weken en mijn geweldige projectgenoten die voor overwinningen bij de publieksjury's zorgden. Verder wil ik al het ondersteunend personeel van het KVI bedanken voor al hun hulp bij het onderzoek en daaromheen.

I would like to thank the three members of my thesis approval committee, professors Ronnie Hoekstra, Jochen Küpper, and Gerard Meijer, for carefully reading my thesis and for being so kind to send me very detailed comments that I could use to improve this thesis. Ronnie, ook dank dat je mijn extern adviseur was, hoewel al je adviezen meestal niet over molecuulafremmers gingen.

De fijne samenwerking met de groep molecuulafremmers van het LaserLaB aan de VU heeft tot mooie publicaties geleid. Daarvoor wil ik Rick Bethlem, Marina Quintero-Pérez, Paul Jansen en Thomas Wall hartelijk danken.

Naast het onderzoek heb ik een heel leuke en leerzame tijd gehad in de Centrale Ondernemingsraad van FOM. Daarvoor bedank ik graag alle leden van de COR 2013-2014 en de ambtelijk secretaris. Hoewel het in een terugblik erger klinkt dan het was, hebben we nog best onze stempel op het drank-, drugs-, vrouwenbeleid en de liquide middelen weten te drukken.

In het vertrouwen dat mijn beide paranimfen, Corine en Elwin, me ook op die laatsgenoemde vlakken zullen steunen tijdens en kort na de verdediging, dank ik ze bij voorbaat alvast.

Mijn ouders wil ik bedanken voor de belangstelling die ze altijd hadden voor mijn onderzoek, en met name mijn vader die bij een ontwerpprobleem gelijk driftig schetsen begon te maken voor onderdelen in RVS.

Als allerlaatste grote dank aan mijn favoriete collega. Het wordt vaker gezegd op deze plek, maar zonder jouw hulp was dit proefschrift echt niet geweest wat het nu is. Ik wens je heel veel sterkte en succes bij de laatste loodjes van je eigen boekje. In ieder geval wordt je omslag mooier dan de mijne. Ik hoop dat je nog lang mijn favoriete huisgenoot blijft.

List of publications

Ra^+ ion trapping: toward an atomic parity violation measurement and an optical clock, M. Nuñez Portela, E. A. Dijck, A. Mohanty, H. Bekker, J. E. van den Berg, G. S. Giri, S. Hoekstra, C. J. G. Onderwater, S. Schlesser, R. G. E. Timmermans, O. O. Versolato, L. Willmann, H. W. Wilschut, and K. Jungmann, Applied Physics B **114**, 173–182 (2014) doi: 10.1007/s00340-013-5603-2.

Traveling-wave deceleration of SrF molecules, J. E. van den Berg, S. C. Mathavan, C. Meinema, J. Nauta, T. H. Nijbroek, K. Jungmann, H. L. Bethlem, and S. Hoekstra, J. Mol. Spectrosc. **300**, Spectroscopic Tests of Fundamental Physics, 22–25 (2014) doi: 10.1016/j.jms.2014.02.004.

Deceleration and trapping of ammonia molecules in a traveling-wave decelerator, Paul Jansen, Marina Quintero-Pérez, Thomas E. Wall, Joost E. van den Berg, Steven Hoekstra, and Hendrick L. Bethlem, Phys. Rev. A **88**, 043424 (2013) doi: 10.1103/PhysRevA.88.043424.

First test of Lorentz invariance in the weak decay of polarized nuclei, S. E. Müller, E. A. Dijck, H. Bekker, J. E. van den Berg, O. Böll, S. Hoekstra, K. Jungmann, C. Meinema, J. P. Noordmans, M. Nuñez Portela, C. J. G. Onderwater, C. Pijpker, A. P. P. van der Poel, B. Santra, A. Sytema, R. G. E. Timmermans, O. O. Versolato, L. Willmann, H. W. Wilschut, and K. Yai, Phys. Rev. D **88**, 071901 (2013) doi: 10.1103/PhysRevD.88.071901.

Towards a precise measurement of atomic parity violation in a single Ra^+ ion, M. Nuñez Portela, J. E. van den Berg, H. Bekker, O. Böll, E. A. Dijck, G. S. Giri, S. Hoekstra, K. Jungmann, A. Mohanty, C. J. G. Onderwater, B. Santra, S. Schlesser, R. G. E. Timmermans, O. O. Versolato, L. W. Wansbeek, L. Willmann, and H. W. Wilschut, Hyperfine Interact. **214**, 157–162 (2013) doi: 10.1007/s10751-013-0774-0.

Static Trapping of Polar Molecules in a Traveling Wave Decelerator, Marina Quintero-Pérez, Paul Jansen, Thomas E. Wall, Joost E. van den Berg, Steven Hoekstra, and Hendrick L. Bethlem, Phys. Rev. Lett. **110**, 133003 (2013) doi: 10.1103/PhysRevLett.110.133003.

Deceleration and trapping of heavy diatomic molecules using a ring-decelerator, J. E. van den Berg, S. H. Turkesteen, E. B. Prinsen, and S. Hoekstra, Eur. Phys. J. D **66**, 235 (2012) doi: 10.1140/epjd/e2012-30017-5.

Isotope shifts of the $6d^2D_{3/2} - 7p^2P_{1/2}$ transition in trapped short-lived $^{209-214}Ra^+$, G. S. Giri, O. O. Versolato, J. E. van den Berg, O. Böll, U. Dammalapati, D. J. van der Hoek, K. Jungmann, W. L. Kruithof, S. Müller, M. Nuñez Portela, C. J. G. Onderwater, B. Santra, R. G. E. Timmermans, L. W. Wansbeek, L. Willmann, and H. W. Wilschut, Phys. Rev. A **84**, 020503 (2011) doi: 10.1103/PhysRevA.84.020503.

Precision spectroscopy of trapped radioactive radium ions, G. S. Giri, O. O. Versolato, L. W. Wansbeek, J. E. van den Berg, D. J. van der Hoek, K. Jungmann, W. L. Kruithof, C. J. G. Onderwater, B. K. Sahoo, B. Santra, P. D. Shidling, R. G. E. Timmermans, L. Willmann, and H. W. Wilschut, Can. J. Phys. **89**, 69–72 (2011) doi: 10.1139/P10-089.

Hyperfine structure of the $6d^2D_{3/2}$ level in trapped short-lived $^{211,209}Ra^+$ ions, O. O. Versolato, G. S. Giri, J. E. van den Berg, O. Böll, U. Dammalapati, D. J. van der Hoek, S. Hoekstra, K. Jungmann, W. L. Kruithof, S. Müller, M. Nuñez Portela, C. J. G. Onderwater, B. Santra, R. G. E. Timmermans, L. W. Wansbeek, L. Willmann, and H. W. Wilschut, Phys. Lett. A **375**, 3130–3133 (2011) doi: 10.1016/j.physleta.2011.07.002.

Atomic parity violation in a single trapped radium ion, O. O. Versolato, L. W. Wansbeek, G. S. Giri, J. E. van den Berg, D. J. van der Hoek, K. Jungmann, W. L. Kruithof, C. J. G. Onderwater, B. K. Sahoo, B. Santra, P. D. Shidling, R. G. E. Timmermans, L. Willmann, and H. W. Wilschut, Can. J. Phys. **89**, 65–68 (2011) doi: 10.1139/P10-051.

Laser spectroscopy of trapped short-lived Ra^+ ions, O. O. Versolato, G. S. Giri, L. W. Wansbeek, J. E. van den Berg, D. J. van der Hoek, K. Jungmann, W. L. Kruithof, C. J. G. Onderwater, B. K. Sahoo, B. Santra, P. D. Shidling, R. G. E. Timmermans, L. Willmann, and H. W. Wilschut, Phys. Rev. A **82**, 010501 (2010) doi: 10.1103/PhysRevA.82.010501.

Bibliography

[1] Hendrick L. Bethlem and Gerard Meijer, *Production and application of translationally cold molecules*, Int. Rev. Phys. Chem. **22**, 73–128 (2003) doi: 10.1080/0144235021000046422.

[2] Sebastiaan Y. T. van de Meerakker, Hendrick L. Bethlem, and Gerard Meijer, *Taming molecular beams*, Nat Phys **4**, 595–602 (2008) doi: 10.1038/nphys1031.

[3] J. Doyle, B. Friedrich, R. V. Krems, and F. Masnou-Seeuws, *Editorial: Quo vadis, cold molecules?*, Eur. Phys. J. D **31**, 149–164 (2004) doi: 10.1140/epjd/e2004-00151-x.

[4] Lincoln D. Carr, David DeMille, Roman V. Krems, and Jun Ye, *Cold and ultracold molecules: science, technology and applications*, New J. Phys. **11**, 055049 (2009) doi: 10.1088/1367-2630/11/5/055049.

[5] O. Dulieu and C. Gabbanini, *The formation and interactions of cold and ultracold molecules: new challenges for interdisciplinary physics*, Rep. Prog. Phys. **72**, 086401 (2009) doi: 10.1088/0034-4885/72/8/086401.

[6] J. J. Hudson, B. E. Sauer, M. R. Tarbutt, and E. A. Hinds, *Measurement of the Electron Electric Dipole Moment Using YbF Molecules*, Phys. Rev. Lett. **89**, 023003 (2002) doi: 10.1103/PhysRevLett.89.023003.

[7] J. J. Hudson, D. M. Kara, I. J. Smallman, B. E. Sauer, M. R. Tarbutt, and E. A. Hinds, *Improved measurement of the shape of the electron*, Nature **473**, 493–496 (2011) doi: 10.1038/nature10104.

[8] A. C. Vutha, W. C. Campbell, Y. V. Gurevich, N. R. Hutzler, M. Parsons, D. Patterson, E. Petrik, B. Spaun, J. M. Doyle, G. Gabrielse, and D. DeMille, *Search for the electric dipole moment of the electron with thorium monoxide*, J. Phys. B: At., Mol. Opt. Phys. **43**, 074007 (2010) doi: 10.1088/0953-4075/43/7/074007.

[9] The ACME Collaboration, J. Baron, W. C. Campbell, D. DeMille, J. M. Doyle, G. Gabrielse, Y. V. Gurevich, P. W. Hess, N. R. Hutzler, E. Kirilov, I. Kozyryev, B. R. O'Leary, C. D. Panda, M. F. Parsons, E. S. Petrik, B. Spaun, A. C. Vutha, and A. D. West, *Order of Magnitude Smaller Limit on the Electric Dipole Moment of the Electron*, Science **343**, 269–272 (2014) doi: 10.1126/science.1248213.

[10] M. R. Tarbutt, J. J. Hudson, B. E. Sauer, and E. A. Hinds, *Prospects for measuring the electric dipole moment of the electron using electrically trapped polar molecules*, Faraday Discuss. **142**, 37–56 (2009) doi: 10.1039/B820625B.

[11] Andreas Osterwalder, Samuel A. Meek, Georg Hammer, Henrik Haak, and Gerard Meijer, *Deceleration of neutral molecules in macroscopic traveling traps*, Phys. Rev. A **81**, 051401(R) (2010) doi: 10.1103/PhysRevA.81.051401.

[12] Samuel A. Meek, Maxwell F. Parsons, Georg Heyne, Viktor Platschkowski, Henrik Haak, Gerard Meijer, and Andreas Osterwalder, *A traveling wave decelerator for neutral polar molecules*, Rev. Sci. Instrum. **82**, 093108 (2011) doi: 10.1063/1.3640413.

[13] O.P. Sushkov and V.V. Flambaum, *Parity breaking effects in diatomic molecules*, Sov. Phys. JETP **48**, 608 (1978).

[14] V. V. Flambaum and I. B. Khriplovich, *On the enhancement of parity nonconserving effects in diatomic molecules*, Phys. Lett. A **110**, 121–125 (1985) doi: 10.1016/0375-9601(85)90756-X.

[15] M. G. Kozlov and L. N. Labzowsky, *Parity violation effects in diatomics*, J. Phys. B: At., Mol. Opt. Phys. **28**, 1933 (1995) doi: 10.1088/0953-4075/28/10/008.

[16] D. DeMille, S. B. Cahn, D. Murphree, D. A. Rahmlow, and M. G. Kozlov, *Using Molecules to Measure Nuclear Spin-Dependent Parity Violation*, Phys. Rev. Lett. **100**, 023003 (2008) doi: 10.1103/PhysRevLett.100.023003.

[17] T. A. Isaev, S. Hoekstra, and R. Berger, *Laser-cooled RaF as a promising candidate to measure molecular parity violation*, Phys. Rev. A **82**, 052521 (2010) doi: 10.1103/PhysRevA.82.052521.

[18] J. F. Barry, D. J. McCarron, E. B. Norrgard, M. H. Steinecker, and D. DeMille, *Magneto-optical trapping of a diatomic molecule*, Nature **512**, 286–289 (2014) doi: 10.1038/nature13634.

[19] S. M. Skoff, R. J. Hendricks, C. D. J. Sinclair, M. R. Tarbutt, J. J. Hudson, D. M. Segal, B. E. Sauer, and E. A. Hinds, *Doppler-free laser spectroscopy of buffer-gas-cooled molecular radicals*, New J. Phys. **11**, 123026 (2009) doi: 10.1088/1367-2630/11/12/123026.

[20] J. F. Barry, E. S. Shuman, and D. DeMille, *A bright, slow cryogenic molecular beam source for free radicals*, Phys. Chem. Chem. Phys. **13**, 18936–18947 (2011) doi: 10.1039/C1CP20335E.

[21] J. F. Barry, E. S. Shuman, E. B. Norrgard, and D. DeMille, *Laser Radiation Pressure Slowing of a Molecular Beam*, Phys. Rev. Lett. **108**, 103002 (2012) doi: 10.1103/PhysRevLett.108.103002.

[22] Sebastiaan Y. T. van de Meerakker, Hendrick L. Bethlem, Nicolas Vanhaecke, and Gerard Meijer, *Manipulation and Control of Molecular Beams*, Chem. Rev. **112**, 4828–4878 (2012) doi: 10.1021/cr200349r.

[23] Nicholas R. Hutzler, Hsin-I Lu, and John M. Doyle, *The Buffer Gas Beam: An Intense, Cold, and Slow Source for Atoms and Molecules*, Chem. Rev. **112**, 4803–4827 (2012) doi: 10.1021/cr200362u.

[24] Edvardas Narevicius and Mark G. Raizen, *Toward Cold Chemistry with Magnetically Decelerated Supersonic Beams*, Chem. Rev. **112**, 4879–4889 (2012) doi: 10.1021/cr2004597.

[25] Christiane P. Koch and Moshe Shapiro, *Coherent Control of Ultracold Photoassociation*, Chem. Rev. **112**, 4928–4948 (2012) doi: 10.1021/cr2003882.

[26] T. D. Lee and C. N. Yang, *Question of Parity Conservation in Weak Interactions*, Phys. Rev. **104**, 254–258 (1956) doi: 10.1103/PhysRev.104.254.

[27] C. S. Wu, E. Ambler, R. W. Hayward, D. D. Hoppes, and R. P. Hudson, *Experimental Test of Parity Conservation in Beta Decay*, Phys. Rev. **105**, 1413–1415 (1957) doi: 10.1103/PhysRev.105.1413.

[28] J. H. Christenson, J. W. Cronin, V. L. Fitch, and R. Turlay, *Evidence for the 2π Decay of the K_2^0 Meson*, Phys. Rev. Lett. **13**, 138–140 (1964) doi: 10.1103/PhysRevLett.13.138.

[29] Michael E. Peskin and Daniel V. Schroeder, *Introduction to Quantum Field Theory* (Perseus Books Publishing L.L.C, 1995).

[30] G. Hinshaw, D. Larson, E. Komatsu, D. N. Spergel, C. L. Bennett, J. Dunkley, M. R. Nolta, M. Halpern, R. S. Hill, N. Odegard, L. Page, K. M. Smith, J. L. Weiland, B. Gold, N. Jarosik, A. Kogut, M. Limon, S. S. Meyer, G. S. Tucker, E. Wollack, and E. L. Wright, *Nine-year Wilkinson Microwave Anisotropy Probe (WMAP) Observations: Cosmological Parameter Results*, The Astrophysical Journal Supplement Series **208**, 19 (2013) doi: 10.1088/0067-0049/208/2/19.

[31] Jonathan Engel, Michael J. Ramsey-Musolf, and U. van Kolck, *Electric dipole moments of nucleons, nuclei, and atoms: The Standard Model and beyond*, Progress in Particle and Nuclear Physics **71**, Fundamental Symmetries in the Era of the LHC, 21–74 (2013) doi: 10.1016/j.ppnp.2013.03.003.

[32] B. C. Regan, Eugene D. Commins, Christian J. Schmidt, and David DeMille, *New Limit on the Electron Electric Dipole Moment*, Phys. Rev. Lett. **88**, 071805 (2002) doi: 10.1103/PhysRevLett.88.071805.

[33] M. R. Tarbutt, B. E. Sauer, J. J. Hudson, and E. A. Hinds, *Design for a fountain of YbF molecules to measure the electron's electric dipole moment*, New J. Phys. **15**, 053034 (2013) doi: 10.1088/1367-2630/15/5/053034.

[34] H. L. Bethlem, M. Kajita, B. Sartakov, G. Meijer, and W. Ubachs, *Prospects for precision measurements on ammonia molecules in a fountain*, The European Physical Journal - Special Topics **163**, 55–69 (2008) doi: 10.1140/epjst/e2008-00809-5.

[35] Peter W. Graham and Surjeet Rajendran, *Axion dark matter detection with cold molecules*, Phys. Rev. D **84**, 055013 (2011) doi: 10.1103/PhysRevD.84.055013.

[36] Sheldon L. Glashow, *Partial-symmetries of weak interactions*, Nuclear Physics **22**, 579–588 (1961) doi: 10.1016/0029-5582(61)90469-2.

[37] Abdus Salam, *Gauge unification of fundamental forces*, Rev. Mod. Phys. **52**, 525–538 (1980) doi: 10.1103/RevModPhys.52.525.

[38] Steven Weinberg, *A Model of Leptons*, Phys. Rev. Lett. **19**, 1264–1266 (1967) doi: 10.1103/PhysRevLett.19.1264.

[39] M. A. Bouchiat and C. C. Bouchiat, *Weak neutral currents in atomic physics*, Phys. Lett. B **48**, 111–114 (1974) doi: 10.1016/0370-2693(74)90656-X.

[40] V. V. Flambaum and I. B. Khriplovich, *P-odd nuclear forces - a source of parity violation in atoms*, JETP Lett. **52**, Original Zh. Eksp. Teor. Fiz. 79 (1980) 1656, 835 (1980).

[41] J. S. M. Ginges and V. V. Flambaum, *Violations of fundamental symmetries in atoms and tests of unification theories of elementary particles*, Phys. Rep. **397**, 63–154 (2004) doi: 10.1016/j.physrep.2004.03.005.

[42] C. S. Wood, S. C. Bennett, D. Cho, B. P. Masterson, J. L. Roberts, C. E. Tanner, and C. E. Wieman, *Measurement of Parity Nonconservation and an Anapole Moment in Cesium*, Science **275**, 1759–1763 (1997) doi: 10.1126/science.275.5307.1759.

[43] W. C. Haxton and C. E. Wieman, *Atomic parity nonconservation and nuclear anapole moments*, Annu. Rev. Nucl. Part. Sci. **51**, 261–293 (2001) doi: 10.1146/annurev.nucl.51.101701.132458.

[44] A. Borschevsky, M. Iliaš, V. A. Dzuba, V. V. Flambaum, and P. Schwerdtfeger, *Relativistic study of nuclear-anapole-moment effects in diatomic molecules*, Phys. Rev. A **88**, 022125 (2013) doi: 10.1103/PhysRevA.88.022125.

[45] Bertrand Desplanques, John F. Donoghue, and Barry R. Holstein, *Unified treatment of the parity violating nuclear force*, Annals of Physics **124**, 449–495 (1980) doi: 10.1016/0003-4916(80)90217-1.

[46] M. G. Kozlov, L. N. Labzowsky, and A. O. Mitrushchenkov, *Parity nonconservation in diatomic molecules in a strong constant magnetic field*, Sov. Phys. JETP **73**, 415–421 (1991).

[47] T. A. Isaev and R. Berger, *Electron correlation and nuclear charge dependence of parity-violating properties in open-shell diatomic molecules*, Phys. Rev. A **86**, 062515 (2012) doi: 10.1103/PhysRevA.86.062515.

[48] Malaya K. Nayak and B. P. Das, *Relativistic configuration-interaction study of the nuclear-spin-dependent parity-nonconserving electron-nucleus interaction constant W_A in BaF*, Phys. Rev. A **79**, 060502 (2009) doi: 10.1103/PhysRevA.79.060502.

[49] M. G. Kozlov, A. V. Titov, N. S. Mosyagin, and P. V. Souchko, *Enhancement of the electric dipole moment of the electron in the BaF molecule*, Phys. Rev. A **56**, R3326(R)–R3329(R) (1997) doi: 10.1103/PhysRevA.56.R3326.

[50] A. V. Titov, N. S. Mosyagin, and V. F. Ezhov, *P,T-Odd Spin-Rotational Hamiltonian for YbF Molecule*, Phys. Rev. Lett. **77**, 5346–5349 (1996) doi: 10.1103/PhysRevLett.77.5346.

[51] N. S. Mosyagin, M. G. Kozlov, and A. V. Titov, *Electric dipole moment of the electron in the YbF molecule*, J. Phys. B: At., Mol. Opt. Phys. **31**, L763 (1998) doi: 10.1088/0953-4075/31/19/002.

[52] Yu. Yu. Dmitriev, Yu. G. Khait, M. G. Kozlov, L. N. Labzovsky, A. O. Mitrushenkov, A. V. Shtoff, and A. V. Titov, *Calculation of the spin-rotational Hamiltonian including P- and P, T-odd weak interaction terms for HgF and PbF molecules*, Phys. Lett. A **167**, 280–286 (1992) doi: 10.1016/0375-9601(92)90206-2.

[53] M. G. Kozlov, V. I. Fomichev, Y. Y. Dmitriev, L. N. Labzovsky, and A. V. Titov, *Calculation of the P- and T-odd spin-rotational Hamiltonian of the PbF molecule*, J. Phys. B: At., Mol. Opt. Phys. **20**, 4939 (1987) doi: 10.1088/0022-3700/20/19/007.

[54] K. I. Baklanov, A. N. Petrov, A. V. Titov, and M. G. Kozlov, *Progress toward the electron electric-dipole-moment search: Theoretical study of the PbF molecule*, Phys. Rev. A **82**, 060501(R) (2010) doi: 10.1103/PhysRevA.82.060501.

[55] S. B. Cahn, J. Ammon, E. Kirilov, Y. V. Gurevich, D. Murphree, R. Paolino, D. A. Rahmlow, M. G. Kozlov, and D. DeMille, *Zeeman-Tuned Rotational Level-Crossing Spectroscopy in a Diatomic Free Radical*, Phys. Rev. Lett. **112**, 163002 (2014) doi: 10.1103/PhysRevLett.112.163002.

[56] S. G. Porsev, K. Beloy, and A. Derevianko, *Precision Determination of Electroweak Coupling from Atomic Parity Violation and Implications for Particle Physics*, Phys. Rev. Lett. **102**, 181601 (2009) doi: 10.1103/PhysRevLett.102.181601.

[57] V. A. Dzuba, J. C. Berengut, V. V. Flambaum, and B. Roberts, *Revisiting Parity Nonconservation in Cesium*, Phys. Rev. Lett. **109**, 203003 (2012) doi: 10.1103/PhysRevLett.109.203003.

[58] Chiu Man Ho and Robert J. Scherrer, *Anapole dark matter*, Phys. Lett. B **722**, 341–346 (2013) doi: 10.1016/j.physletb.2013.04.039.

[59] Hooman Davoudiasl, Hye-Sung Lee, and William J. Marciano, *Muon Anomaly and Dark Parity Violation*, Phys. Rev. Lett. **109**, 031802 (2012) doi: 10.1103/PhysRevLett.109.031802.

[60] Hooman Davoudiasl, Hye-Sung Lee, and William J. Marciano, *"Dark" Z implications for parity violation, rare meson decays, and Higgs physics*, Phys. Rev. D **85**, 115019 (2012) doi: 10.1103/PhysRevD.85.115019.

[61] Y. V. Stadnik and V. V. Flambaum, *Nuclear spin-dependent interactions: searches for WIMP, axion and topological defect dark matter, and tests of fundamental symmetries*, Eur. Phys. J. C **75**, 110 (2015) doi: 10.1140/epjc/s10052-015-3326-8.

[62] B. M. Roberts, Y. V. Stadnik, V. A. Dzuba, V. V. Flambaum, N. Leefer, and D. Budker, *Limiting P-Odd Interactions of Cosmic Fields with Electrons, Protons, and Neutrons*, Phys. Rev. Lett. **113**, 081601 (2014) doi: 10.1103/PhysRevLett.113.081601.

[63] Y. V. Stadnik and V. V. Flambaum, *Axion-induced effects in atoms, molecules, and nuclei: Parity nonconservation, anapole moments, electric dipole moments, and spin-gravity and spin-axion momentum couplings*, Phys. Rev. D **89**, 043522 (2014) doi: 10.1103/PhysRevD.89.043522.

[64] Seong Keun Kim, Taekjip Ha, and Jean-Pierre Schermann, *Editorial of the PCCP themed issue*, Phys. Chem. Chem. Phys. **13**, 804–805 (2011) doi: 10.1039/C0CP90114H.

[65] William A. Bonner, *The origin and amplification of biomolecular chirality*, Orig. Life Evol. Biosph. **21**, 59–111 (1991) doi: 10.1007/BF01809580.

[66] Martin Quack, *How Important is Parity Violation for Molecular and Biomolecular Chirality?*, Angewandte Chemie International Edition **41**, 4618–4630 (2002) doi: 10.1002/anie.200290005.

[67] William A. Bonner, *Parity violation and the evolution of biomolecular homochirality*, Chirality **12**, 114–126 (2000) doi: 10.1002/(SICI)1520-636X(2000)12:3<114::AID-CHIR3>3.0.CO;2-N.

[68] Martin Quack, Jürgen Stohner, and Martin Willeke, *High-Resolution Spectroscopic Studies and Theory of Parity Violation in Chiral Molecules*, Annu. Rev. Phys. Chem. **59**, 741–769 (2008) doi: 10.1146/annurev.physchem.58.032806.104511.

[69] Benoît Darquié, Clara Stoeffler, Alexander Shelkovnikov, Christophe Daussy, Anne Amy-Klein, Christian Chardonnet, Samia Zrig, Laure Guy, Jeanne Crassous, Pascale Soulard, Pierre Asselin, Thérèse R. Huet, Peter Schwerdtfeger, Radovan Bast, and Trond Saue, *Progress toward the first observation of parity violation in chiral molecules by high-resolution laser spectroscopy*, Chirality **22**, 870–884 (2010) doi: 10.1002/chir.20911.

[70] Clara Stoeffler, Benoît Darquié, Alexander Shelkovnikov, Christophe Daussy, Anne Amy-Klein, Christian Chardonnet, Laure Guy, Jeanne Crassous, Thérèse R. Huet, Pascale Soulard, and Pierre Asselin, *High resolution spectroscopy of methyltrioxorhenium: towards the observation of parity violation in chiral molecules*, Phys. Chem. Chem. Phys. **13**, 854–863 (2011) doi: 10.1039/C0CP01806F.

[71] Hendrick L. Bethlem and Wim Ubachs, *Testing the time-invariance of fundamental constants using microwave spectroscopy on cold diatomic radicals*, Faraday Discuss. **142**, 25–36 (2009) doi: 10.1039/B819099B.

[72] Marina Quintero-Pérez, Thomas E. Wall, Steven Hoekstra, and Hendrick L. Bethlem, *Preparation of an ultra-cold sample of ammonia molecules for precision measurements*, J. Mol. Spectrosc. **300**, Spectroscopic Tests of Fundamental Physics, 112–115 (2014) doi: 10.1016/j.jms.2014.03.018.

[73] Marina Quintero-Pérez, Paul Jansen, Thomas E. Wall, Joost E. van den Berg, Steven Hoekstra, and Hendrick L. Bethlem, *Static Trapping of Polar Molecules in a Traveling Wave Decelerator*, Phys. Rev. Lett. **110**, 133003 (2013) doi: 10.1103/PhysRevLett.110.133003.

[74] Paul Jansen, Marina Quintero-Pérez, Thomas E. Wall, Joost E. van den Berg, Steven Hoekstra, and Hendrick L. Bethlem, *Deceleration and trapping of ammonia molecules in a traveling-wave decelerator*, Phys. Rev. A **88**, 043424 (2013) doi: 10.1103/PhysRevA.88.043424.

[75] Mikhail Lemeshko, Roman V. Krems, John M. Doyle, and Sabre Kais, *Manipulation of molecules with electromagnetic fields*, Mol. Phys. **111**, 1648–1682 (2013) doi: 10 . 1080 / 00268976.2013.813595.

[76] Goulven Quéméner and Paul S. Julienne, *Ultracold Molecules under Control!*, Chem. Rev. **112**, 4949–5011 (2012) doi: 10.1021/cr300092g.

[77] Jolijn Onvlee, Sjoerd N. Vogels, Alexander von Zastrow, David H. Parker, and Sebastiaan Y. T. van de Meerakker, *Molecular collisions coming into focus*, Phys. Chem. Chem. Phys. **16**, 15768–15779 (2014) doi: 10.1039/C4CP01519C.

[78] C. Trefzger, C. Menotti, B. Capogrosso-Sansone, and M. Lewenstein, *Ultracold dipolar gases in optical lattices*, J. Phys. B: At., Mol. Opt. Phys. **44**, 193001 (2011) doi: 10.1088/0953-4075/44/19/193001.

[79] K.-K. Ni, S. Ospelkaus, M. H. G. de Miranda, A. Pe'er, B. Neyenhuis, J. J. Zirbel, S. Kotochigova, P. S. Julienne, D. S. Jin, and J. Ye, *A High Phase-Space-Density Gas of Polar Molecules*, Science **322**, 231–235 (2008) doi: 10.1126/science.1163861.

[80] S. Ospelkaus, K.-K. Ni, M. H. G. de Miranda, B. Neyenhuis, D. Wang, S. Kotochigova, P. S. Julienne, D. S. Jin, and J. Ye, *Ultracold polar molecules near quantum degeneracy*, Faraday Discuss. **142**, 351–359 (2009) doi: 10.1039/B821298H.

[81] N. E. Bulleid, S. M. Skoff, R. J. Hendricks, B. E. Sauer, E. A. Hinds, and M. R. Tarbutt, *Characterization of a cryogenic beam source for atoms and molecules*, Phys. Chem. Chem. Phys. **15**, 12299–12307 (2013) doi: 10.1039/C3CP51553B.

[82] Hsin-I Lu, Julia Rasmussen, Matthew J. Wright, Dave Patterson, and John M. Doyle, *A cold and slow molecular beam*, Phys. Chem. Chem. Phys. **13**, 18986–18990 (2011) doi: 10.1039/C1CP21206K.

[83] Nicholas R. Hutzler, Maxwell F. Parsons, Yulia V. Gurevich, Paul W. Hess, Elizabeth Petrik, Ben Spaun, Amar C. Vutha, David DeMille, Gerald Gabrielse, and John M. Doyle, *A cryogenic beam of refractory, chemically reactive molecules with expansion cooling*, Phys. Chem. Chem. Phys. **13**, 18976–18985 (2011) doi: 10.1039/C1CP20901A.

[84] Stephen D. Hogan, Michael Motsch, and Frédéric Merkt, *Deceleration of supersonic beams using inhomogeneous electric and magnetic fields*, Phys. Chem. Chem. Phys. **13**, 18705–18723 (2011) doi: 10.1039/C1CP21733J.

[85] K. Luria, W. Christen, and U. Even, *Generation and Propagation of Intense Supersonic Beams*, J. Phys. Chem. A **115**, 7362–7367 (2011) doi: 10.1021/jp201342u.

[86] M. R. Tarbutt, J. J. Hudson, B. E. Sauer, E. A. Hinds, V. A. Ryzhov, V. L. Ryabov, and V. F. Ezhov, *A jet beam source of cold YbF radicals*, J. Phys. B: At., Mol. Opt. Phys. **35**, 5013 (2002) doi: 10.1088/0953-4075/35/24/306.

[87] A. Trimeche, M. N. Bera, J.-P. Cromières, J. Robert, and N. Vanhaecke, *Trapping of a supersonic beam in a traveling magnetic wave*, Eur. Phys. J. D **65**, 263–271 (2011) doi: 10.1140/epjd/e2011-20096-1.

[88] Giovanni Sanna and Giuseppe Tomassetti, *Introduction to Molecular Beams Gas Dynamics.* (Imperial College Press, 2005).

[89] Manish Gupta and Dudley Herschbach, *A Mechanical Means to Produce Intense Beams of Slow Molecules*, J. Phys. Chem. A **103**, 10670–10673 (1999) doi: 10.1021/jp993560x.

[90] Manish Gupta and Dudley Herschbach, *Slowing and Speeding Molecular Beams by Means of a Rapidly Rotating Source*, J. Phys. Chem. A **105**, 1626–1637 (2001) doi: 10.1021/jp002640u.

[91] M. Strebel, F. Stienkemeier, and M. Mudrich, *Improved setup for producing slow beams of cold molecules using a rotating nozzle*, Phys. Rev. A **81**, 033409 (2010) doi: 10.1103/PhysRevA.81.033409.

[92] Hendrick L. Bethlem, Giel Berden, and Gerard Meijer, *Decelerating Neutral Dipolar Molecules*, Phys. Rev. Lett. **83**, 1558–1561 (1999) doi: 10.1103/PhysRevLett.83.1558.

[93] Samuel A. Meek, Horst Conrad, and Gerard Meijer, *A Stark decelerator on a chip*, New J. Phys. **11**, 055024 (2009) doi: 10.1088/1367-2630/11/5/055024.

[94] Ludwig Scharfenberg, Henrik Haak, Gerard Meijer, and Sebastiaan Y. T. van de Meerakker, *Operation of a Stark decelerator with optimum acceptance*, Phys. Rev. A **79**, 023410 (2009) doi: 10.1103/PhysRevA.79.023410.

[95] Hendrick L. Bethlem, Floris M. H. Crompvoets, Rienk T. Jongma, Sebastiaan Y. T. van de Meerakker, and Gerard Meijer, *Deceleration and trapping of ammonia using time-varying electric fields*, Phys. Rev. A **65**, 053416 (2002) doi: 10.1103/PhysRevA.65.053416.

[96] Sebastiaan Y. T. van de Meerakker, Paul H. M. Smeets, Nicolas Vanhaecke, Rienk T. Jongma, and Gerard Meijer, *Deceleration and Electrostatic Trapping of OH Radicals*, Phys. Rev. Lett. **94**, 023004 (2005) doi: 10.1103/PhysRevLett.94.023004.

[97] Steven Hoekstra, Markus Metsälä, Peter C. Zieger, Ludwig Scharfenberg, Joop J. Gilijamse, Gerard Meijer, and Sebastiaan Y. T. van de Meerakker, *Electrostatic trapping of metastable NH molecules*, Phys. Rev. A **76**, 063408 (2007) doi: 10.1103/PhysRevA.76.063408.

[98] Steven Hoekstra, Joop J. Gilijamse, Boris Sartakov, Nicolas Vanhaecke, Ludwig Scharfenberg, Sebastiaan Y. T. van de Meerakker, and Gerard Meijer, *Optical Pumping of Trapped Neutral Molecules by Blackbody Radiation*, Phys. Rev. Lett. **98**, 133001 (2007) doi: 10.1103/PhysRevLett.98.133001.

[99] Brian C. Sawyer, Benjamin L. Lev, Eric R. Hudson, Benjamin K. Stuhl, Manuel Lara, John L. Bohn, and Jun Ye, *Magnetoelectrostatic Trapping of Ground State OH Molecules*, Phys. Rev. Lett. **98**, 253002 (2007) doi: 10.1103/PhysRevLett.98.253002.

[100] Joop J. Gilijamse, Steven Hoekstra, Samuel A. Meek, Markus Metsälä, Sebastiaan Y. T. van de Meerakker, Gerard Meijer, and Gerrit C. Groenenboom, *The radiative lifetime of metastable CO ($a\,^3\Pi, v = 0$)*, J. Chem. Phys **127**, 221102 (2007) doi: 10.1063/1.2813888.

[101] Benjamin K. Stuhl, Brian C. Sawyer, Dajun Wang, and Jun Ye, *Magneto-optical Trap for Polar Molecules*, Phys. Rev. Lett. **101**, 243002 (2008) doi: 10.1103/PhysRevLett.101.243002.

[102] M. R. Tarbutt, H. L. Bethlem, J. J. Hudson, V. L. Ryabov, V. A. Ryzhov, B. E. Sauer, G. Meijer, and E. A. Hinds, *Slowing Heavy, Ground-State Molecules using an Alternating Gradient Decelerator*, Phys. Rev. Lett. **92**, 173002 (2004) doi: 10.1103/PhysRevLett.92.173002.

[103] Hendrick L. Bethlem, M. R. Tarbutt, Jochen Küpper, David Carty, Kirstin Wohlfart, E. A. Hinds, and Gerard Meijer, *Alternating gradient focusing and deceleration of polar molecules*, J. Phys. B: At., Mol. Opt. Phys. **39**, R263 (2006) doi: 10.1088/0953-4075/39/16/R01.

[104] Kirstin Wohlfart, Fabian Grätz, Frank Filsinger, Henrik Haak, Gerard Meijer, and Jochen Küpper, *Alternating-gradient focusing and deceleration of large molecules*, Phys. Rev. A **77**, 031404 (2008) doi: 10.1103/PhysRevA.77.031404.

[105] S. Chervenkov, X. Wu, J. Bayerl, A. Rohlfes, T. Gantner, M. Zeppenfeld, and G. Rempe, *Continuous Centrifuge Decelerator for Polar Molecules*, Phys. Rev. Lett. **112**, 013001 (2014) doi: 10.1103/PhysRevLett.112.013001.

[106] M. D. Di Rosa, *Laser-cooling molecules*, Eur. Phys. J. D **31**, 395–402 (2004) doi: 10.1140/epjd/e2004-00167-2.

[107] E. S. Shuman, J. F. Barry, and D. DeMille, *Laser cooling of a diatomic molecule*, Nature **467**, 820–823 (2010) doi: 10.1038/nature09443.

[108] V. Zhelyazkova, A. Cournol, T. E. Wall, A. Matsushima, J. J. Hudson, E. A. Hinds, M. R. Tarbutt, and B. E. Sauer, *Laser cooling and slowing of CaF molecules*, Phys. Rev. A **89**, 053416 (2014) doi: 10.1103/PhysRevA.89.053416.

[109] Matthew T. Hummon, Mark Yeo, Benjamin K. Stuhl, Alejandra L. Collopy, Yong Xia, and Jun Ye, *2D Magneto-Optical Trapping of Diatomic Molecules*, Phys. Rev. Lett. **110**, 143001 (2013) doi: 10.1103/PhysRevLett.110.143001.

[110] I. J. Smallman, F. Wang, T. C. Steimle, M. R. Tarbutt, and E. A. Hinds, *Radiative branching ratios for excited states of ^{174}YbF: Application to laser cooling*, J. Mol. Spectrosc. **300**, Spectroscopic Tests of Fundamental Physics, 3–6 (2014) doi: 10.1016/j.jms.2014.02.006.

[111] Corine Meinema, PhD thesis (University of Groningen), in preparation.

[112] D. DeMille, J. F. Barry, E. R. Edwards, E. B. Norrgard, and M. H. Steinecker, *On the transverse confinement of radiatively slowed molecular beams*, Mol. Phys. **111**, 1805–1813 (2013) doi: 10.1080/00268976.2013.793833.

[113] Gerhard Herzberg, *Molecular Spectra and Molecular Structure*, 2nd ed., Vol. 1 (Van Nostrand, 1950), 680 pp., Reprinted 2008, Reitell.

[114] John M. Brown and Alan Carrington, *Rotational Spectroscopy of Diatomic Molecules* (Cambridge University Press, 2003).

[115] Richard L. Liboff, *Introductory Quantum Mechanics*, 4th ed. (Addison Wesley, 2003).

[116] A. R. Edmonds, *Angular Momentum in Quantum Mechanics*, Revised Printing Second Edition 1968 (Princeton University Press, 1960).

[117] Wolfram Research, Inc., *Mathematica version 9.0*, (2012)

[118] K. P. Huber and G. Herzberg, "Constants of Diatomic Molecules", (data prepared by J. W. Gallagher and R. D. Johnson III), in *NIST Chemistry WebBook*, edited by P. J. Linstrom and W. G. Mallard, NIST Standard Reference Database Number 69 (National Institute of Standards and Technology, 2011).

[119] C. M. Western, *PGOPHER, a Program for Simulating Rotational Structure*, http://pgopher.chm.bris.ac.uk.

[120] W. J. Childs, L. S. Goodman, U. Nielsen, and V. Pfeufer, *Electric-dipole moment of CaF ($X\,^2\Sigma^+$) by molecular beam, laser-rf, double-resonance study of Stark splittings*, J. Chem. Phys **80**, 2283–2287 (1984) doi: 10.1063/1.447005.

[121] W. E. Ernst, J. Kändler, S. Kindt, and T. Törring, *Electric dipole moment of SrF $X\,^2\Sigma^+$ from high-precision stark effect measurements*, Chem. Phys. Lett. **113**, 351–354 (1985) doi: 10.1016/0009-2614(85)80379-1.

[122] P. Colarusso, B. Guo, K.-Q. Zhang, and P. F. Bernath, *High-Resolution Infrared Emission Spectrum of Strontium Monofluoride*, J. Mol. Spectrosc. **175**, 158–171 (1996) doi: 10.1006/jmsp.1996.0019.

[123] W. E. Ernst, J. Kändler, and T. Törring, *Hyperfine structure and electric dipole moment of BaF $X\,^2\Sigma^+$*, J. Chem. Phys **84**, 4769–4773 (1986) doi: 10.1063/1.449961.

[124] Ch. Ryzlewicz, H.-U. Schütze-Pahlmann, J. Hoeft, and T. Törring, *Rotational spectrum and hyperfine structure of the $^2\Sigma$ radicals BaF and BaCl*, Chem. Phys. **71**, 389–399 (1982) doi: 10.1016/0301-0104(82)85045-3.

[125] B. E. Sauer, Jun Wang, and E. A. Hinds, *Laser-rf double resonance spectroscopy of ^{174}YbF in the $X\,^2\Sigma^+$ state: Spin-rotation, hyperfine interactions, and the electric dipole moment*, J. Chem. Phys **105**, 7412–7420 (1996) doi: 10.1063/1.472569.

[126] Richard J. Mawhorter, Benjamin S. Murphy, Alexander L. Baum, Trevor J. Sears, T. Yang, P. M Rupasinghe, C. P. McRaven, N. E. Shafer-Ray, Lukas D. Alphei, and Jens-Uwe Grabow, *Characterization of the ground X_1 state of $^{204}Pb^{19}F$, $^{206}Pb^{19}F$, $^{207}Pb^{19}F$, and $^{208}Pb^{19}F$*, Phys. Rev. A **84**, 022508 (2011) doi: 10.1103/PhysRevA.84.022508.

[127] J. E. van den Berg, S. H. Turkesteen, E. B. Prinsen, and S. Hoekstra, *Deceleration and trapping of heavy diatomic molecules using a ring-decelerator*, Eur. Phys. J. D **66**, 235 (2012) doi: 10.1140/epjd/e2012-30017-5.

[128] Hendrick L. Bethlem, André J. A. van Roij, Rienk T. Jongma, and Gerard Meijer, *Alternate Gradient Focusing and Deceleration of a Molecular Beam*, Phys. Rev. Lett. **88**, 133003 (2002) doi: 10.1103/PhysRevLett.88.133003.

[129] Kirstin Wohlfart, Frank Filsinger, Fabian Grätz, Jochen Küpper, and Gerard Meijer, *Stark deceleration of OH radicals in low-field-seeking and high-field-seeking quantum states*, Phys. Rev. A **78**, 033421 (2008) doi: 10.1103/PhysRevA.78.033421.

[130] Sebastiaan Y. T. van de Meerakker, Nicolas Vanhaecke, Hendrick L. Bethlem, and Gerard Meijer, *Higher-order resonances in a Stark decelerator*, Phys. Rev. A **71**, 053409 (2005) doi: 10.1103/PhysRevA.71.053409.

[131] Sebastiaan Y. T. van de Meerakker, Nicolas Vanhaecke, Hendrick L. Bethlem, and Gerard Meijer, *Transverse stability in a Stark decelerator*, Phys. Rev. A **73**, 023401 (2006) doi: 10.1103/PhysRevA.73.023401.

[132] J. J. Gilijamse, S. Hoekstra, N. Vanhaecke, S. Y. T. van de Meerakker, and G. Meijer, *Loading Stark-decelerated molecules into electrostatic quadrupole traps*, Eur. Phys. J. D **57**, 33–41 (2010) doi: 10.1140/epjd/e2010-00008-9.

[133] The MathWorks, Inc., *MATLAB*, Natick, Massachusetts, United States.

[134] Eric Prinsen, *Building A Stark Decelerator*, Master's thesis (University of Groningen, 2011).

[135] W. J. Childs, L. S. Goodman, and I. Renhorn, *Radio-frequency optical double-resonance spectrum of SrF: The $X\,^2\Sigma^+$ state*, J. Mol. Spectrosc. **87**, 522–533 (1981) doi: 10.1016/0022-2852(81)90422-7.

[136] Anh T. Le, Hailing Wang, and Timothy C. Steimle, *Hyperfine structure and Zeeman tuning of the $A\,^2\Pi - X\,^2\Sigma^+(0,0)$ band system of the odd isotopologue of strontium monofluoride ^{87}SrF*, Phys. Rev. A **80**, 062513 (2009) doi: 10.1103/PhysRevA.80.062513.

[137] Timothy C. Steimle, Peter J. Domaille, and David O. Harris, *Rotational analysis of the $B\,^2\Sigma^+ - X\,^2\Sigma^+$ system of SrF using a cw tunable dye laser*, J. Mol. Spectrosc. **68**, 134–145 (1977) doi: 10.1016/0022-2852(77)90429-5.

[138] Piotr S. Żuchowski and Jeremy M. Hutson, *Prospects for producing ultracold NH_3 molecules by sympathetic cooling: A survey of interaction potentials*, Phys. Rev. A **78**, 022701 (2008) doi: 10.1103/PhysRevA.78.022701.

[139] Pavel Soldán, Piotr S. Żuchowski, and Jeremy M. Hutson, *Prospects for sympathetic cooling of polar molecules: NH with alkali-metal and alkaline-earth atoms - a new hope*, Faraday Discuss. **142**, 191–201 (2009) doi: 10.1039/B822769C.

[140] S. K. Tokunaga, W. Skomorowski, P. S. Żuchowski, R. Moszynski, J. M. Hutson, E. A. Hinds, and M. R. Tarbutt, *Prospects for sympathetic cooling of molecules in electrostatic, ac and microwave traps*, Eur. Phys. J. D **65**, 141–149 (2011) doi: 10.1140/epjd/e2011-10719-x.

[141] E. S. Shuman, J. F. Barry, D. R. Glenn, and D. DeMille, *Radiative Force from Optical Cycling on a Diatomic Molecule*, Phys. Rev. Lett. **103**, 223001 (2009) doi: 10.1103/PhysRevLett.103.223001.

[142] N. Vanhaecke and O. Dulieu, *Precision measurements with polar molecules: the role of the black body radiation*, Mol. Phys. **105**, 1723–1731 (2007) doi: 10.1080/00268970701466261.

[143] J. van Veldhoven, J. Küpper, H. L. Bethlem, B. Sartakov, A. J. A. van Roij, and G. Meijer, *Decelerated molecular beams for high-resolution spectroscopy*, Eur. Phys. J. D **31**, 337–349 (2004) doi: 10.1140/epjd/e2004-00160-9.

[144] Paul Jansen, David W. Chandler, and Kevin E. Strecker, *A compact molecular beam machine*, Rev. Sci. Instrum. **80**, 083105 (2009) doi: 10.1063/1.3206367.

[145] Ming-Feng Tu, Jia-Jung Ho, Chih-Chiang Hsieh, and Ying-Cheng Chen, *Intense SrF radical beam for molecular cooling experiments*, Rev. Sci. Instrum. **80**, 113111 (2009) doi: 10.1063/1.3262631.

[146] COMSOL Inc., *COMSOL Multiphysics*.

[147] Janko Nauta, *Aligning and detecting a SrF molecule beam*, Bachelor's thesis (University of Groningen, Oct. 2012).

[148] N. E. Bulleid, R. J. Hendricks, E. A. Hinds, Samuel A. Meek, Gerard Meijer, Andreas Osterwalder, and M. R. Tarbutt, *Traveling-wave deceleration of heavy polar molecules in low-field-seeking states*, Phys. Rev. A **86**, 021404(R) (2012) doi: 10.1103/PhysRevA.86.021404.

[149] J. Kändler, T. Martell, and W.E. Ernst, *Electric dipole moments and hyperfine structure of SrF $A^2\Pi$ and $B^2\Sigma^+$*, Chem. Phys. Lett. **155**, 470–474 (1989) doi: 10.1016/0009-2614(89)87188-X.

[150] N. J. Fitch, D.A. Esteves, M.I. Fabrikant, T. C. Briles, Y. Shyur, L. P. Parazzoli, and H. J. Lewandowski, *State purity of decelerated molecular beams*, J. Mol. Spectrosc. **278**, 1–6 (2012) doi: 10.1016/j.jms.2012.07.005.

[151] Sebastian Trippel, Terence G. Mullins, Nele L. M. Müller, Jens S. Kienitz, Karol Długołęcki, and Jochen Küpper, *Strongly aligned and oriented molecular samples at a kHz repetition rate*, Mol. Phys. **111**, 1738–1743 (2013) doi: 10.1080/00268976.2013.780334.

[152] Tom Nijbroek, *Sisyphus deceleration of SrF explored*, Master's thesis (University of Groningen, July 2013).

[153] J. E. van den Berg, S. C. Mathavan, C. Meinema, J. Nauta, T. H. Nijbroek, K. Jungmann, H. L. Bethlem, and S. Hoekstra, *Traveling-wave deceleration of SrF molecules*, J. Mol. Spectrosc. **300**, Spectroscopic Tests of Fundamental Physics, 22–25 (2014) doi: 10.1016/j.jms.2014.02.004.

[154] Moritz Kirste, Boris G. Sartakov, Melanie Schnell, and Gerard Meijer, *Nonadiabatic transitions in electrostatically trapped ammonia molecules*, Phys. Rev. A **79**, 051401(R) (2009) doi: 10.1103/PhysRevA.79.051401.

[155] T. E. Wall, S. K. Tokunaga, E. A. Hinds, and M. R. Tarbutt, *Nonadiabatic transitions in a Stark decelerator*, Phys. Rev. A **81**, 033414 (2010) doi: 10.1103/PhysRevA.81.033414.

[156] D. J. McCarron, E. B. Norrgard, M. H. Steinecker, and D. DeMille, *Improved magneto-optical trapping of a diatomic molecule*, New J. Phys. **17**, 035014 (2015) doi: 10.1088/1367-2630/17/3/035014.